ABSTRACT

Title of dissertation: CMOS IMAGE SENSORS
FOR LAB-ON-A-CHIP
MICROSYSTEM DESIGN

David Sander, Doctor of Philosophy, 2011

Dissertation Advisor: Dr. Pamela Abshire
Electrical and Computer Engineering Department

The work described herein serves as a foundation for the development of CMOS imaging in lab-on-a-chip microsystems. Lab-on-a-chip (LOC) systems attempt to emulate the functionality of a cell biology lab by incorporating multiple sensing modalidites into a single microscale system. LOC are applicable to drug development, implantable sensors, cell-based bio-chemical detectors and radiation detectors. The common theme across these systems is achieving performance under severe resource constraints including noise, bandwidth, power and size. The contributions of this work are in the areas of two core lab-on-a-chip imaging functions: object detection and optical measurements. Additionally this work describes the development of a CMOS X-ray detector.

This work examines object detection in the context of contact imaging. In the contact imaging configuration the sample of interest is placed in direct contact with the image sensor surface avoiding the use of intermediate optics. Simulations and experiments demonstrate contact imaging as a viable imaging configuration for microfluidic systems.

Address-event-representation asynchronous arrays are a form of data-driven imaging system that have favorable image detection and communication properties for sparse scenes such as the detection of micro-particles. An integrate-and-fire array with active reset was designed to minimize the front-end reset noise associated with integration-based sensors.

Differential sensors inherently increase the fundamental noise floor of the device but provide excellent environmental noise suppression. For portable sensors, environmental noise suppression becomes the dominant source of noise in the system. A differential sensor was designed to mitigate environmental noise and integrated into a hand-held fluorescence detection system. Several biologically relevant experiments were performed detecting the biotoxicity of Poly(amidoamine) dendrimers, the metabolic cycle of yeast, and a live-dead assay on bovine aortic smooth muscle cells.

Bioluminescence detection requires significant noise suppression. A low-noise bioluminescence detector array was designed, tested and fabricated. The sensor array uses a floating gate mismatch compensation technique to minimize mismatch in the sensor array and hence maximize the signal to noise ratio. The effectiveness of this detector was demonstrated using a genetically engineered CANARY cell exposed to a stimulant.

X-ray detectors or other radiation detection play an important function in medical imaging or nuclear material detection. A CMOS image sensor was designed and tested for use as an inexpensive scalable X-ray imaging system.

Finally, integration based sensors were analyzed in the context of an electronic communication channel using the device information rate and channel capacity as a

metric. The results indicate that the integration time of the sensor can be controlled to maximize the capacity of the sensor. Alternatively for integrate-and-fire sensors, the event threshold can be set to optimize the system.

Lab-on-a-chip bioanalysis systems are becoming more influential and provide a basis for massively distributed environmental sensors, implantable sensors, biochemical and nuclear agent detectors, among others. This work provides both a theoretical framework as well as experimentally verifies such techniques for the applications of micro-particle detection and optical measurements.

The original contributions of this thesis include:

- Simulations and experimental validation of contact imaging;

- An architecture for reset noise reduction in integrate and fire address event representation arrays;

- Integrated fluorescence detection;

- An array of adaptive low dark current pixel sensors for bioluminescence detection;

- Analysis and algorithms for information rate optimization for integration based sensors;

CMOS IMAGE SENSORS
FOR LAB-ON-A-CHIP MICROSYSTEM DESIGN

by

David Sander

Dissertation submitted to the Faculty of the Graduate School of the
University of Maryland, College Park in partial fulfillment
of the requirements for the degree of
Doctor of Philosophy
2010

Advisory Committee:
Professor Pamela Abshire, Chair/Advisor
Professor Timothy Horiuchi
Professor Christopher Davis
Professor Martin Peckerar
Professor Keith Harold

Dedicated
To my wife, parents, grandparents, and brothers.

Acknowledgments

Firstly, I would like to thank all of my family and friends who have supported me through this journey. It is their dedication and patience that made this possible. I would like to thank my advisor Dr. Pamela Abshire whom I met while I was an undergraduate student participating in the National Science Foundation sponsored Maryland Engineering Research Internship Teams (MERIT) program at the university of Maryland. It was that experience which led me to doctoral research at the University of Maryland.

I would like to thank my colleagues in the Integrated Biomorphic Information Systems Laboratory. Honghao Ji was my mentor during my first year and whom I worked with on my first CMOS image sensor design. Marc Dandin and Nicole Nelson for their discussion, design work and testing related to integrated fluorescence sensing. Nicole Nelson also provided discussion related to CMOS image sensor information rate optimization. Somashekar Bangalore provided discussion on a wide range of circuit designs. Timir Datta, Yanyi (Eric) Wong, and Peng Xu provided significant discussion related to modeling, designing and testing fabrication mismatch correction using floating gate designs. I would also like to thank Anshu Sarje and Babak Nouri for their discussion on asynchronous designs and Eric Chen for his computer support and technical contributions to several projects outside the scope of this thesis.

I would like to thank two colleagues in the Laboratory for Microtechnologies, Dr. Jeff Burke and Dr. Menake Piyasena for their microfluidic design and cell preparation work related to the bioluminescence detection portion of this thesis.

Contents

List of Tables

List of Figures

List of Abbreviations

κ	subthreshold slope factor
F	Faraday's constant
R	Gas constant
T	Absolute temperature
V_T	Thermal voltage
A/D	Analog to Digital
AC	Alternating Current
CMOS	Complementary Metal-Oxide-Semiconductor
DAQ	Data Acquisition
DC	Direct Current
DIP	Dual In-line Package
DSP	Digital Signal Processing
DUT	Device Under Test
FG	Floating Gate
FPN	Fixed Pattern Noise
GND	electrical GrouND
GPIB	General Purpose Interface Bus
IC	Integrated Circuit
LED	Light Emitting Diode
MOSFET	Metal-Oxide-Semiconductor Field Effect Transistor
NFET	n-type Field Effect Transistor
PCB	Printed Circuit Board
PFET	p-type Filed Effect Transistor
PSD	Power Spectral Density
RMS	Root Mean Square
RNG	Random Number Generator
SNR	Signal to Noise Ratio
UV	Ultra-Violet
VLSI	Very Large Scale Integration

Chapter 1

Introduction

The work described herein serves as a foundation for the development of CMOS imaging in lab-on-a-chip microsystems. Lab-on-a-chip (LOC) systems attempt to emulate the functionality of a cell biology lab by incorporating multiple sensing modalities into a single micro-scale system. LOC are applicable to drug development, implantable sensors, cell-based bio-chemical detectors and radiation detectors. The common theme across these systems are achieving performance under severe resource constraints including noise, bandwidth, power and size.

This work describes the development of two core lab-on-a-chip imaging functions: object detection and optical measurements. Additionally, it includes the development of a CMOS sensor for radiation detection. Object detection encompasses the detection and localization of micro-scale particles. The key requirements of such object detection systems are temporal resolution and spatial resolution. While maintaining a high signal-to-noise ratio is important for any sensing task, other considerations become important, including power consumption, throughput, frame-rate and

other metrics. Optical measurements detect specific optical properties of a sample. In these optical measurement systems, the noise floor and dynamic range of the system are of paramount importance. The focus of this work is object detection for micro-particle localization and control and optical measurements for fluorescence and bioluminescence detection.

Object detection and localization is an important component of lab-on-a-chip systems. LOCs generally have multiple sensing modalities distributed spatially across the device leading to specific spatial and temporal resolution requirements. For conventional imaging systems, the size, weight and cost are determined by the spatial resolution requirements and are not always practical for micro-scale applications, which require low-cost highly portable solutions. An alternative imaging approach is to directly couple the sample of interest to the image sensor surface without intervening optics is referred to as contact imaging and is discussed in Chapter 2. In the contact imaging configuration, an image is acquired by observing the light occluded by the sample or, for luminescent samples, by observing the light emitted by the sample. The benefits and limitations of the contact-imaging configuration have been examined with respect to micro-particle and biological cell detection, and the results indicate that the scope of contact imaging matches well with microfluidic systems, a common element in LOC design, and also increases the collection efficiency of the detector array through geometric advantage.

At the micro-scale it becomes important to be able to move a cell or groups of cells to a specific location for further analysis while disregarding unimportant material, which can include other cells or debris. Dielectrophoresis and electro-osmotic

2

flow offer two mechanisms for moving cells or other micro-size particles in fluid. Optical information such as fluorescence or bioluminescence can be incorporated into these mechanisms to provide visual feedback based particle manipulation. The design of an asynchronous image sensor array for cell steering is discussed in Chapter 3. Although asynchronous arrays have lower spatial resolution than conventional active pixel arrays, they can have advantages in terms of bandwidth utilization and efficient detection of objects of interest. Both attributes are important considerations for micro-scale imaging.

Optical measurements are another important component of LOCs. Two of the most common optical measurements are fluorescent measurements and bioluminescence measurements, and both require highly sensitive detectors.

Fluorescence imaging is one of the most widely used assay methods in cellular biology, the popularity of which is due to the specificity that can be achieved in detecting biochemical attributes. Thousands of natural and man-made fluorophores exist to detect and quantify a wide variety of analytes. Examples of these include the natural autofluorescence of NADH, which is a byproduct of cellular respiration, as well as the artificial fluorescence of FURA-2, a calcium indicator. Fluorescent markers are also a critical part of DNA analysis and biological agent detection, and can be used to discriminate different types of cells. Bioluminescence is a process by which a biochemical reaction produces light and occurs naturally or through genetically modified cells. The primary difference between bioluminescence and fluorescence is that bioluminescence does not require any additional media or excitation source, but as a result the magnitude of light produced by bioluminescence is far below

fluorescence. Several CMOS image sensors have been designed to reduce the effects of correlated noise, reset noise and thermally generated current in the detector thus decreasing the overall noise floor of these systems. These detectors have demonstrated the detection of both fluorescence and bioluminescence.

Under the severe resource constraints of lab-on-a-chip microsystems, the information-power trade-offs become increasingly important. Image sensors can be considered communication channels converting light to electrons. The information capacity of charge-based detectors have been examined and optimized with respect to the integration time of the detector. The combination of the methods described above can provide optical measurements at a spatial and temporal resolution beyond other systems.

Chapter 2 discusses the theory, simulation and experimental results for contact imaging. Chapter 3 discusses the application of an address-event representation-based image sensor array that minimizes the effects of reset noise. Chapter 4 discusses the design, analysis and experimental results of a differential image sensor. Chapter 5 discusses a hand-held fluorometer utilizing a differential image sensor. Chapter 6 discusses an adaptive array of low-dark current capacitive trans-impedance based image sensors. Chapter 7 discusses a high-density low-dark current pixel and experimental results using the pixel as an X-ray detector. Chapter 8 discusses the optimization of CMOS integration based sensors in the context using the device information rate as a metric. Chapter 9 summarizes the overarching goals, results, and implications and describes opportunities for future work.

1.1 Applications

The sensors developed in this work focus on applications related to detecting electron-hole pair generation due to incident electromagnetic energy. These applications include: contact imaging, detection of micro-scale objects, detection of fluorescence, bioluminescence and X-rays. The diverse nature of these applications enable a wide range of devices from implantable devices to ubiquitous environmental sensors to nuclear material detectors. From a system perspective, each of these systems requires trade-offs between high signal-to-noise ratio, high spatial resolution and built in application specific signal processing.

1.1.1 Contact Imaging

Microsystem image sensors require aggressive system scale-down in all aspects. While conventional imaging systems can achieve micrometer-to-sub-micrometer resolution, these systems generally use magnifying optics. Optics introduce additional weight, size, complexity and cost to the system and therefore may be undesirable in many implantable situations. For some applications, such as identification of anatomical structures, the spatial resolution afforded without additional optics may be sufficient. A method of imaging without intervening optics is known as contact imaging.

To avoid the need for intermediate optics while still achieving micro-scale resolution, the sample of interest can be placed directly on the sensor surface. The image can then be acquired by projecting light through the sample onto the sensor, or light emitted by the sample can be collected by the sensor. While these contact

imaging systems do not have the spatial resolution of conventional optics based imaging systems, contact imaging presents an opportunity for imaging applications that conventional optical based systems cannot offer such as portable and implantable biosensors. This method of imaging has been demonstrated to maintain high image contrast up to and beyond 100 μm, the scale of most microfluidic systems.

1.1.2 Particle Control

When performing analyses at the micro-scale it is advantageous to multiplex sensing modalities to gain a richer description of the sample of interest. In the context of biological cells and other micro-particles this may include electrical, impedance, capacitance and optical measurements. Therefore, it is important to develop methods in which biological cells and other micro-particles can be controlled in micro-scale environments. Several micro-scale control systems exist including optical tweezers, dielectrophoresis and electro-osmotic flow. While each of these methods can be used for manipulating particles in a open-loop configuration, the precision and complexity of movement can be greatly improved through the use of optical feedback. Optical feedback for electro-osmotic flow has been demonstrated using CCDs and other frame-based methods, however, these conventional systems are often inefficient in terms of bandwidth requirements, information trade-offs and downstream computational complexity. Asynchronous image sensor arrays can provide an efficient imaging alternative to conventional frame-based approaches for the application of micro-particle sensing steering and control.

1.1.3 Fluorescence

Fluorescence sensing is ubiquitous in life science applications because it provides extremely sensitive and highly selective measurements for many analytes. Standard spectrofluorometers require an excitation source, a detector and a method of separating the excitation and emission light such as optical filters, gratings and mirrors [11]. Whereas much bench-top fluorescence experimentation is carried out using large and costly equipment, lab-on-a-chip (LOC) systems seek to scale-down the required experimental equipment with the goal of creating systems that are portable. This implies that significant integration of the components is required to perform fluorescence measurements at the micro-scale.

Standard laboratory fluorescence detectors use charge-coupled devices (CCDs) or photomultiplier tubes (PMTs) to detect the weak light emitted by a fluorescent species. PMTs are expensive and bulky, require high voltages and power, and thus are not readily utilized for hand-held applications. Although CCDs offer high image quality, fill factor and dynamic range, they also require more power than CMOS detectors and are more difficult to integrate with other sensing, analog-to-digital conversion, and signal processing circuitry [12]. While it is true that a hand-held fluorometer can be manufactured using discrete components such as CCDs and optical filters, these are not easily integrated with other sensing modalities such as bio-amplifiers or capacitive sensors [13, 14]. Implementing the sensor in CMOS offers the opportunity for dense multi-sensor integration where fluorescence can be used, for example, in sorting viable cells, which are then further investigated using other techniques. CMOS im-

plementations additionally provide the option to incorporate signal processing on the same chip, which can reduce the overall system power consumption and minimizes the hardware necessary for system integration.

1.1.4 Bioluminescence

Bioluminescence represents an important class of optical information and can provide fast, selective responses to stimuli compared to other bio-detection systems. Bioluminescence can be found naturally in biology or more recently in genetically modified cells. One such example of a genetically modified bioluminescence cell is the CANARY cell developed by MIT. CANARY cells are genetically modified B cells with an additional gene to express a fluorescent protein. This technique takes advantage of the selectivity, specificity and biological memory of the B cell. When an antigen binds to the antibodies of the B cell, calcium pathways are opened in the same way a B cell would respond to a normal pathogen, but this calcium influx now triggers a bioluminescent signal.

In bench-top systems, these CANARY cells have been shown to detect particles within 10 minutes successfully. One such bench-top system, BioFlash, has been developed by Innovative Biosensors, Inc. This system has been shown to detect up to 21 different biological agents within minutes. While these systems work well, they are bench-top systems relying on relatively large mechanical multiplexing, sample preparation, and photo-multiplier tubes (PMT) as detection elements. Although bench-top devices are sufficient for many applications, including detection and monitoring of bi-

ological agents in government building, it is desirable to scale the cost and form factor of these sensors to a hand-held size for ubiquitous deployment.

1.1.5 Radiation Detection

Radiation detection has many applications from medical imaging to the detection of nuclear materials and national defense. While specialized detection materials provide high-quality radiation measurements, CMOS sensor present a cost-effective alternative. The physical radiation detection process is nearly identical to that of a standard visible wavelength detector. A high-energy particle creates electron-hole pairs in a detector junction and the integrated radiation-induced current is integrated and read off-chip. Since radiation cannot be focused like visible wavelength images trade-offs between pixel density and noise floor are of primary concern. CMOS image sensors present a viable option for radiation detection with favorable trade-off characteristics.

1.1.6 Optimization

Scientific imaging sensors attempt to minimize noise, and hence maximize the signal to noise ratio (SNR) to produce optimal image quality. While maximizing the SNR works well in a static scene, for time-dependent scenes such as fluorescence measurements measuring cell metabolism, the experimental strategy shifts to "How much information can we retrieve during an experiment?" The answer to this question is related to the fundamental and quantitative bound known as the information capac-

ity of the system. In general, this depends on several factors, including the power of the light emitted by the fluorescent probe as well as the reset noise, shot noise, and integration time of the sensor.

For constant illumination (implying an unchanging scene), increasing integration time implies higher SNR, and thus the amount of information during an experiment is maximized for increased integration times. Previously reported sensor arrays that maximize dynamic range through integration time control have been proposed[15, 16]. However, for time-varying illumination (such as a moving image or during photo-bleaching of a fluorophore), increased integration time obscures information about the changes while a decreased integration time results in a poor SNR. There is therefore an inherent trade-off between the fidelity of an image and the bandwidth.

1.2   Imaging Performance Metrics

A number of sources of uncertainty, collectively referred to as noise, are present regardless of the explicit sensor system design and determines how easily the incoming signal can be detected. In imaging systems, fundamental noise sources arise from photon shot-noise, dark current, reset noise and readout noise, while environmental noise includes power supply noise and electro-magnetically coupled radiation. Photon shot-noise arises due to the uncertainty of photon arrival times and photon-electron generation in the silicon detector is proportional to the illumination power. Additional shot-noise exists due to the electron-hole pairs thermally generated within the

detector. This noise is proportional to the thermally generated current and can significantly affect performance. Other sources of noise at low light levels include reset noise, which results from thermally generated fluctuations in the voltage at the integration node prior to integration, and readout noise, which arises from thermal and shot noise along the readout path. Additional noise sources exist, including coupled electro-magnetic fields and power supply fluctuations. In this work the number of photons required to obtain an SNR of one is used as a metric to compare different detectors.

1.2.1   Photon Shot Noise

Photon shot noise results from uncertainty in the photon arrival times as well as the photon-carrier conversion process and follows Poisson statistics. Therefore, the variance of the photon-generated current I_{ph} is proportional to the mean of the photon-generated arrival rate λ_{ph}, where g_e is the sensor gain and q is the electronic charge is the incident photon-generated current.

$$Var[I_{ph}] = g_e^2 q^2 E[\lambda_{ph}] \tag{1.1}$$

1.2.2   Readout Noise

Readout noise arises from both thermally generated noise and shot noise along the readout path as described by the first and second terms in equation 1.2. This noise depends on several factors including transistor sizing, biasing conditions, region

of operation, and process parameters. The process parameters must be extracted experimentally for noise analysis because process-dependent interface traps may account for a significant portion of the readout noise and are not given as a standard parameter in test data supplied by the chip foundry. The noise current in each transistor is described by Equation 1.2,

$$S_{I_d} = 4\gamma kTg_m + \frac{K_f I_d}{C_{ox}WLf} \tag{1.2}$$

where k is Boltzmann's constant, T is the temperature, g_m is the conductance of the transistor, $\gamma = 2/3$ or $1/3$ depending on the region of operation, K_f is a process dependent parameter, I_d is the drain current of the transistor, and C_{ox}, W and L are the oxide capacitance per unit area, and the geometric parameters of the device.

1.2.3 Reset Noise

Reset noise results from uncertainty in the number of charges, and hence voltage, at the integration node upon reset. Thermally generated carriers cause a fluctuation of carriers on and off the capacitive node around the desired reset value. This phenomenon has been extensively described for image sensors [17–19]. Additional noise comes from the uncertainty in the number of injected charges by closing the reset switch, but for high speed systems this noise is generally negligible [20].

Several reset methodologies have been developed for integration mode active pixel sensors including hard reset, soft reset and active reset. Representative schematics for each of these methodologies are shown in Figure 1.1.
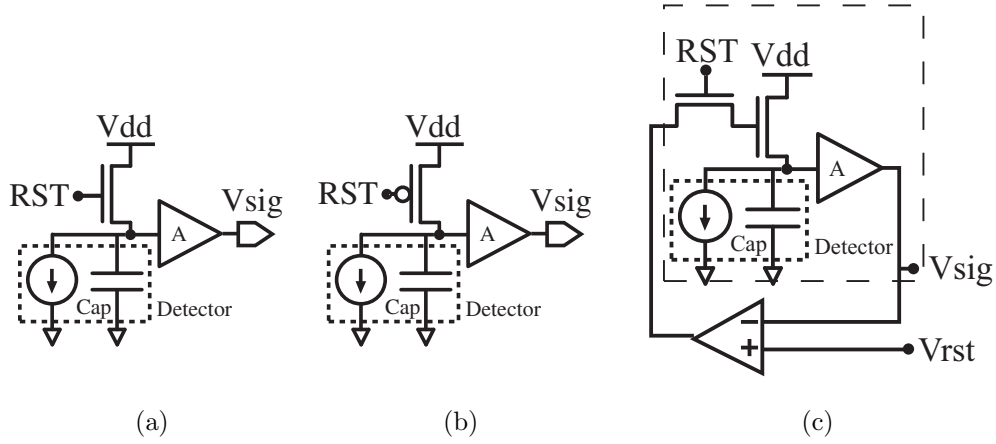
Figure 1.1: Reset techniques for active pixel sensors. a. Soft reset pixel schematic, b. Hard reset pixel schematic, c. Active reset schematic.

The first approach for resetting a pixel is hard reset. With hard reset, the reset transistor is over-driven such that it operates like a digital switch. Hard reset produces reset noise of kT/C but provides the largest signal dynamic range possible. The second method of reset is soft reset. In soft reset the gate of the reset transistor is driven high, and the source is connected to the integration node. As the voltage at the integration node rises, the reset transistor turns itself off. Due to this non-equilibrium condition, the reset noise results in at most kT/2C. Although this method has a lower reset noise than hard reset, it suffers from a lower dynamic range because the integration node will rise to at most a threshold below VDD, as well as image lag. Image lag results because the final integration node voltage depends on the integration node voltage prior to reset.

A method to mitigate the image lag was developed by Pain [21]. This method performs a hard reset to a specified voltage such that the previous integrated value is erased, following which soft reset is performed. This can be achieved using a standard

13

three transistor pixel as shown in Figure 1.1(a).

In 2000, Fowler *et al.* developed the active-reset technique [22]. The active-reset technique reduces reset noise by incorporating an explicit feedback amplifier into the reset path to ensure that the pixel settles to a specific reset value, thereby also reducing fixed pattern noise. Figure 1.1(c) shows the general configuration for a pixel using active reset. The positive terminal of the amplifier is connected to the specified reset value. The output of the amplifier is connected to the gate of the reset transistor through an enable switch. Any variation at the reset node due to thermal noise occurs along the readout path into the negative terminal of the amplifier. For an amplifier with sufficiently high bandwidth, the amplifier is capable of compensating for the reset noise. The key to minimizing the noise is that the reset transistor provides sufficiently high impedance, thereby limiting the bandwidth of the reset noise. Although the high impedance does not limit the noise itself, it limits the bandwidth sufficiently such that the feedback amplifier can compensate. The reset noise becomes a combination of the noise along the readout line that has been prematurely compensated at the reset node as well as noise in the reset signal at the positive input terminal of the amplifier. Fowler has shown a reduction of 18X over the predicted thermal noise [22]. A number of other groups have reported similar noise reduction results using the mechanism described above [23–27]

The main drawback with this active feedback method is that the transistor is only capable of providing current in one direction. This means that unless a well controlled reset signal is employed, overshoot can occur. To prevent overshoot, typically a voltage ramp is used to reset the pixel.

Other structures have been suggested using similar principles to active-reset including using an amplifier to modulate the drain source voltage of a hard-reset transistor in a feedback loop. Although this method produces some noise suppression, it is not as successful because the reset switch in hard reset has a low resistance, and therefore the reset noise has a bandwidth larger than the amplifier [28]. Yet another method is to connect the output of a single transistor amplifier to its input via a hard reset transistor [29]. Once again, the reset noise has a wide bandwidth and, in addition, the final reset value will be illumination dependent. This illumination-dependence arises because the photodiode provides a second current path for the single transistor amplifier. However, this nonlinearity should be deterministic and small, and therefore may be compensated for off-line. Interestingly, the last two methods, although inferior in noise reduction, can be implemented in a simple manner, and therefore can be incorporated into various systems including address-event type systems.

1.2.4 Dark Current

The dark current of CMOS image sensors is mainly produced by thermally generated leakage current from the reversed-bias photodiode and parasitic junctions. Dark current introduces several artifacts in the signal collected by active pixel sensors. Figure 1.1(a) shows the schematic of a conventional three-transistor one-photodiode integration mode active pixel sensor (APS). During integration, the reverse-biased voltage across the n^+/p_{sub} photodiode decreases at a rate of $(I_{ph} + I_{dk})t_{int}/C_{ph}$ where

I_{ph} is the photocurrent, I_{dk} is the dark current, t_{int} is the integration time, and C_{ph} is the total capacitance of the integration node. Clearly, dark current reduces the dynamic range of the sensor. Additionally, temporal noise increases due to the shot noise of the dark current at a rate proportional to the magnitude of the dark current. When observing an ensemble of detector measurements, given the same noise and biasing conditions the increase in voltage variance as a function of time is:

$$Var[V(t)] = g_e^2 q^2 (\lambda_{dk}) t$$

where I_{dk} is the dark current, g is the sensor gain and t is time.

For most integration mode pixels, dark current contributes additional signal-dependent noise and device non-linearity. In standard pixels, such as the three-transistor one-photodiode pixel shown in Figure 1.1(a), I_{ph}, I_{dk} and C_{ph} change with reverse bias across the photodiode. Surface and bulk leakage currents contribute the primary sources of dark current, I_{dk}, of the reversed n^+/p_{sub} photodiode. Therefore the amount of dark current generated over an integration cycle is dependent on the photo-generated current, as this produces a time-varying reverse bias. This implies that the dark current will be spatially varying in accordance with different illumination levels across the pixel array.

Increasing the reverse bias across the photodiode has been shown to increase the dark current [2, 30]. Loukianova experimentally showed that the dark currents are directly related to reverse bias voltage as shown in Figure 1.2. While increasing reverse bias across the photodiode may have the benefit of increasing collection efficiency, the subsequent increase in dark current may negate this advantage. This problem is

16
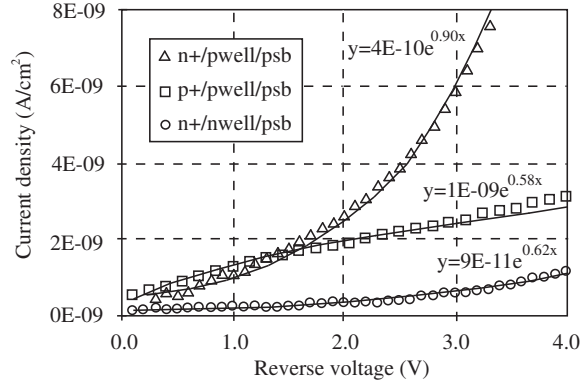
Figure 1.2: Reverse IV characteristics for n+/n-well/psb, p+/n-well/psb, and n+/p-well/psb together with fitted functions [2].

particularly troublesome for implementing image sensors in deep sub-micron CMOS technologies. Several design techniques have been proposed to minimize artifacts induced by dark current. Abdallah *et al.* developed a pixel using a shielded dummy phototransistor to obtain an estimate of the dark current and subtract this value from nearby pixels [31]. While this can eliminate a large portion of the dark current, the biasing conditions for the dummy transistor and sensor cannot be matched, and therefore the dark current cannot be completely eliminated. Additionally, introducing dummy pixels into the imager array decreases the spatial resolution. Another method implements double sampling over two integration cycles to remove dark current artifacts [32]. However, this method sacrifices speed, since two integration cycles must occur in order to get data from one pixel. Also, since the dark current is a random process, subtracting an estimate of the dark current reduces the DC offset in the signal, but actually increases the overall uncertainty in the measurement.

It has been shown that the ratio of quantum efficiency to dark current is maximized when the reverse-biased photodiode voltage is held close to zero volts [30]. This

technique has been implemented in standard APS format [33] as well as an integrate-and-fire format [34]. Several structure capable of pinning the reverse-biased junction voltage have been reported; the simplest is shown in Figure 1.3(a). A capacitive trans-impedance amplifier (CTIA) is the most well known structures for pinning the photodiode voltage near zero. The simplest CTIA amplifier uses a capacitor in the negative feedback path of an amplifier to maintain near-zero potential across the photodiode for the duration of integration. Another variation utilizes offset correction via correlated double sampling [35]. Although the photodiode is biased near zero, the reset transistor still contributes some leakage current at the integration node. As a result, a modified CTIA developed by Bolton *et al.* uses a switching network to maintain zero bias across the reset transistor during signal integration [34]. This minimizes the leakage current at the photodiode node while providing a buffered output for the integrated signal voltage. Figure 1.3(b) depicts this low-dark current CTIA pixel. An array of CTIA pixels has been designed to minimize dark current through a mismatch compensation technique described in Chapter 6.

While these structures minimize the dark and leakage currents, they have a relatively large footprint because there is an amplifier in each pixel. Pseudo-active pixels for low-dark-current applications have also been developed comprised of several pseudo-active pixels connected to one amplifier [36, 37]. This method attempts to reduce the footprint by sharing the feedback amplifier, but because several pixels are connected to the same amplifier, there is a possibility of blooming and other artifacts. The authors found that, at most four pixels can be connected to the same amplifier before these leakage effects outweigh the benefits of the feedback amplifier.
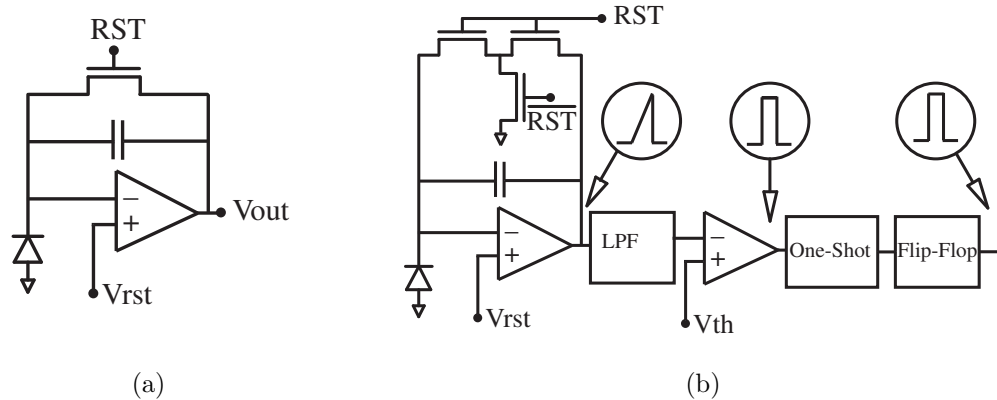
Figure 1.3: Capacitive trans-impedance amplifier (CTIA) pixel schematics. a. Conventional CTIA schematic, b. Low-dark current CTIA schematic.

Ji *et al.* developed a method for fixing the reversed bias photodiode voltage near zero volts while decoupling the integration node from the photodiode node [38]. This structure provides high front-end gain at the expense of remaining leakage currents at the integration node. Additionally, the leakage current reduction method can be implemented either in-pixel or chip-wise with little variation on the leakage properties. For the in-pixel configuration, the reverse-biased voltage is maintained through local feedback ensuring the highest dark current rejection at the expense of footprint. The chip-level configuration provides a high level of dark current rejection with minimal footprint but cannot optimize the biasing condition in each pixel.

1.2.5 Environmental Noise

Although dark current and reset noise are the primary sources of fundamental noise, in practice, power supply fluctuations and other coupled environmental noise sources may significantly affect sensor performance. For many scientific imaging ap-

plications power supply noise, ground bounce, and other environmental noise sources may be well controlled, but in portable and implantable systems this may not be true. As such, techniques such as differential structures have been utilized to increase environmental noise immunity.

Fujimori used a passive pixel sensor with alternating elements either exposed to light or covered in metal [39]. Eltoukhy *et al.* developed a pseudo-differential pixel sensor, where the integrated photo signal and a fixed bias voltage were read out along identical readout paths thereby suppressing noise [40, 41]. The use of a global bias voltage may still be susceptible to noise through the effects of ground bounce and coupling of transistors from logic traces. Ji *et al.* proposed another differential architecture by incorporating a sample-and-hold node in pixel. At the end of the integration cycle the sampled voltage and the integrated photo signal were read out along identical readout paths [38, 42, 43]. The differential structure proposed by Ji *et al.* samples the local photodiode voltage, providing the highest environmental noise rejection. While all of theses differential sensors decrease environmental noise at the expense of fundamental noise, the sensor developed by Eltoukhy *et al.* does not increase reset noise. In addition, because of its architecture the active techniques developed by Fowler *et al.* can be applied. Additionally, differential architectures require somewhat more complex double sampling structures which may reduce the advantages of differential readout. Despite these drawbacks, differential pixels make excellent candidates for portable and implantable wireless sensor systems because of their noise rejection capabilities. The design of a differential pixel sensor is described in Chapter 4, and the sensor was incorporated into a hand-held fluorescence sensor

described in Chapter 5.

1.2.6 Signal to Noise Ratio

The signal-to-noise ratio (SNR) is a metric that quantifies how much an observable signal has been corrupted by noise. For image sensors, each of the above noise sources must be taken into account when comparing system architectures. The system SNR is described by equation 1.3. Unless stated otherwise, we will evaluate systems based on an SNR of 1, which by convention represents when the signal power is equal to the noise power.

$$SNR(t) = \frac{Signal}{Noise} = \frac{g_e^2 q^2 \eta^2 \lambda_{ph}^2(t)}{\sigma_{reset}^2 + \sigma_{readout}^2 + \sigma_{environment}^2 + g^2 \lambda_d(t) + g_e^2 q^2 \eta \lambda_{ph}(t)} \quad (1.3)$$

where g_e^2 is the electron gain, q is the electronic charge, η is the quantum efficiency, λ_{ph} is the photon arrival rate, $sigma_{reset}^2$ is the reset noise, $sigma_{readout}^2$ is the readout noise, $sigma_{environment}^2$ is the environmental noise.

1.2.7 Noise Effective Power

The noise effective power (NEP) is the incident power necessary to have an SNR of 1. This is an attractive metric for environments where one cannot control the incident illumination power and will be used in the context of bioluminescence detection. In the case of imaging systems, the SNR is often dependent on both the magnitude of the incident illumination as well as the length of the observation. The

resulting NEP is described in equation 1.4.

$$NEP(t) = g^2 q^2 \eta^2 \lambda_{ph}^2(t) - g^2 q^2 \eta \lambda_{ph} - g^2 q^2 \lambda_d(t) - \sigma_{reset}^2 - \sigma_{readout}^2 - \sigma_{environment}^2 = 0$$

(1.4)

Solving Equation 1.4 using the quadratic equation, the NEP is related to the incident illumination by Equation 1.5

$$NEP(t) = \frac{g^2 q^2 \eta^2 + -\sqrt{g^2 q^2 \eta^2 - 4g^2 \sigma_{reset}^2 - \sigma_{readout}^2 - \sigma_{environment}^2 - g^2 q^2 \lambda_d(t)}}{2g^2 q^2}$$

(1.5)

1.3 Imaging Systems

There are many commercially available imaging systems. The most popular imaging systems include: photo-multiplier tubes (PMTs), charge-coupled devices (CCDs), CMOS active-pixel sensors (APSs), and hybrid detectors. A brief description of each detector is provided below.

1.3.1 Photo-multiplier Tubes

Photo-multiplier Tubes (PMTs) are considered the gold standard of scientific detectors and have unrivaled noise performance. Photons are absorbed at the photo-cathode and excite electrons. These electrons enter a vacuum under a high electric
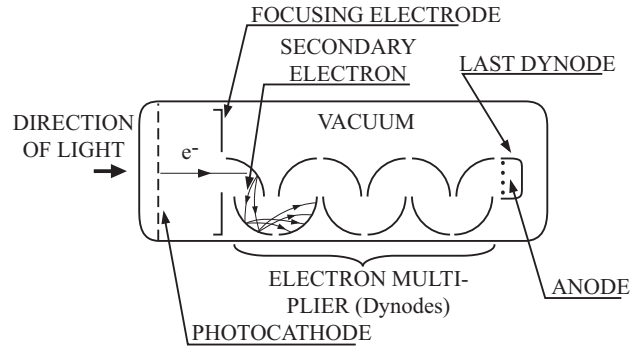
Figure 1.4: Diagram of a photomultiplier tube operation

field and are accelerated and focused onto a dynode. When they hit the dynode, they produce multiple secondary electrons which are then accelerated under a high electric field to the next dynode. At each stage the number of electrons increases due to the multiplicative secondary emission and continues until the last dynode, at which point all the electrons are collected. The primary advantage of these systems is that they have fast temporal dynamics as well as extremely low dark current and high front-end gain. The low dark current comes from the material properties of the front end photo-cathode, and the high gain comes from the multiple stages of secondary emission. While PMTs possess superior noise performance, they rely on high-quality materials, vacuums, high-electric fields, and a geometry that do not scale well to microsystems, nor to provide spatial resolution.

1.3.2 Charge-Coupled Devices

Charge-coupled devices (CCDs) have been used for many imaging applications because they have relatively low noise compared to other sensors. A bias is applied to a polysilicon covering the substrate, which forms a depletion region. Photons travel
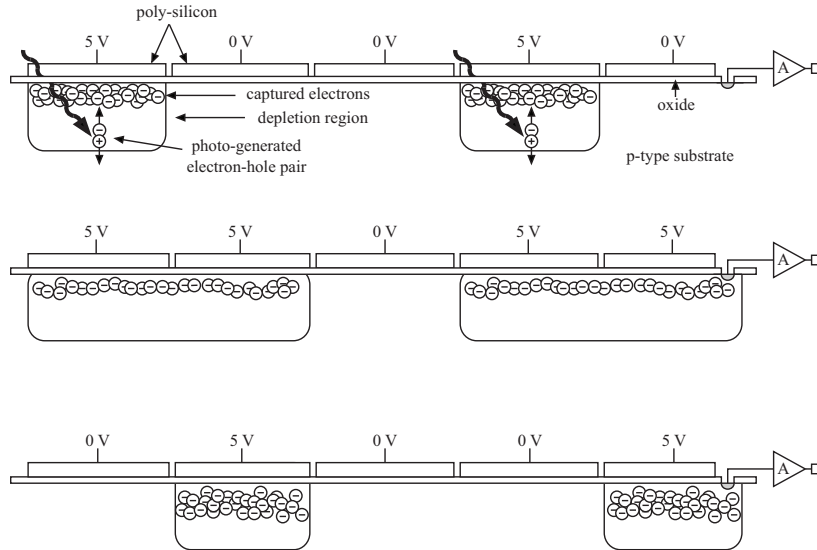
Figure 1.5: Diagram of charge-coupled device (CCD) cross-section and operation

through the polysilicon gate and form electron hole pairs. These charges remain for the duration of the integration cycle. A CCD accomplishes readout using a bucket brigade, passing the charges from one pixel to the next through sequential biasing of the polysilicon regions. Then (at the row level) charges are transferred to a high impedance node for amplification and readout at the row or column level. Although the CCD achieves nearly 100% fill factor (the percentage of active area to total pixel area) it has several drawbacks. Because CCDs use a charge transfer bucket brigade, 100% charge transfer efficiency from one pixel to another is imperative during readout since charge loss accumulates over the readout path. This can be achieved but requires slow frame rates. Additionally, because the whole chip is essentially a capacitor, a high capacitive driving system is needed to perform integration and readout, which also prohibits high frame rates. Fabrication also presents a drawback of the CCDs. CCD fabrication requires a specialized fabrication process and has not been successfully integrated with other CMOS electronics despite decades of attempts [44].

1.3.3 Active Pixel Sensors

Active pixel sensors are sensors in which both the detector and associated active readout electronics are integrated onto the same device. Common active pixel detectors include photogates, photodiodes, and phototransistors essentially any device that can perform an optoelectronic conversion in a controlled manner. The active readout electronics may be as simple as a unity-gain buffer to more sophisticated signal processing architectures. Descriptions of some of the most common active pixel detectors are described below.

Photogates

The photogate is essentially a single stage CCD. It collects charge under a polysilicon gate in the same manner as the CCD but then transfers the charge to a local high impedance buffered node for readout thereby relaxing constraints on transfer efficiency. Photogates are often used because of their high front-end gain, which is independent of the detector size. The primary drawbacks of the photogate are: the gate filters some of the light, it is difficult to achieve 100% charge transfer to the readout node and it requires driving a large capacitive load for collection and transfer. Another drawback with photogates is that they are charge-mode devices and as such require explicit timing functions. However, since the pixels perform local readout, only one charge transfer is required, and the system can achieve a much higher frame rate than the CCD [12].
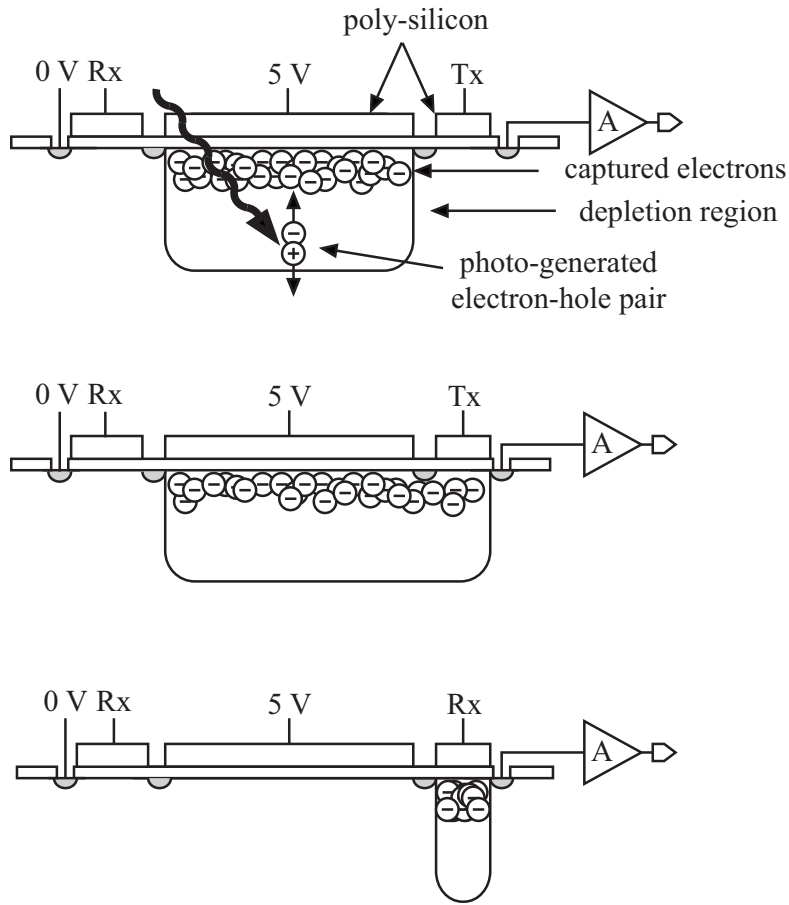
Figure 1.6: Diagram of a photogate active pixel sensor cross-section and operation
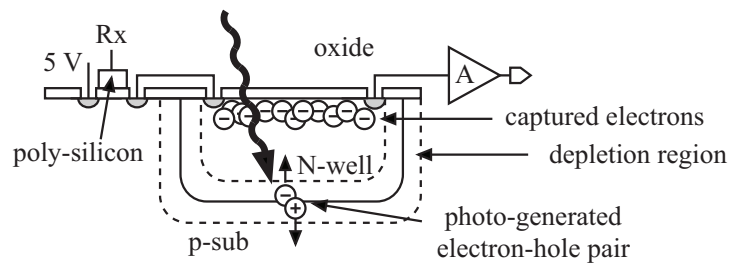
Figure 1.7: Diagram of a photodiode active pixel sensor cross-section and operation

Photodiodes

One of the simplest transduction elements is the p-n junction, commonly referred to as a photodiode. When an incident photon transfers energy to an electron-hole pair in the depletion region of the diode, an electron-hole pair is broken in the lattice enabling the mobile electron and hole to move freely in the silicon. Because of the built-in electric fields of the p-n junction, the electron and hole are separated and swept to their respective quasi neutral regions. The quasi-neutral region captures the freed carriers, which are then read out through various mechanisms which will be discussed later. In an integration mode pixel, whereby the photocurrent is accumulated onto a capacitive node, the front-end gain of the photodiode is typically scales detector area. This is traditionally one drawback to photodiode and phototransistor pixels since larger devices have smaller gain.

Single Photon Avalanche Detectors

Silicon photo-avalanche devices (SPADs) are a sub-set of the p-n junction based detectors but are considered separately here due to their operational requirements. SPADS are semiconductor-based devices in which an extremely high reverse bias voltage is applied to a p-n junction. The large reverse-bias provides several advantages. The large reverse-bias creates a large depletion region thereby increasing the quantum efficiency of the detector. In addition, the large reverse bias creates a large electric field. This large electric field imparts enough energy to a photo-generated carrier so that when it collides with the silicon lattice, secondary electrons are emitted, thereby
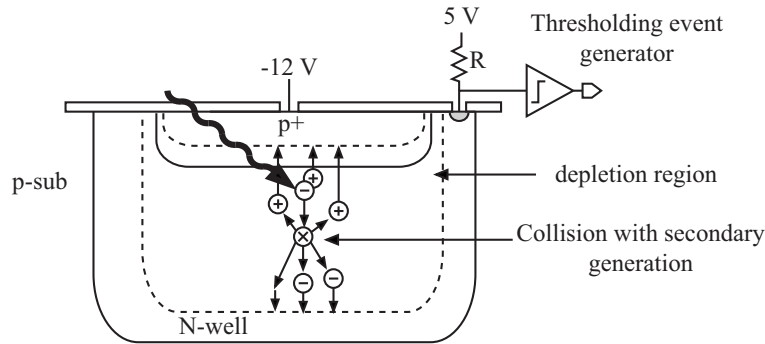
Figure 1.8: Diagram of a single-photon avalanche detector cross-section and operation

increasing the front end gain. This process is the semiconductor analog to the PMT. The large electric field also decreases the transit time of carriers within the junction allowing fast time dynamics of a signal to be observed. The primary drawback of SPADs is that they suffer from a large dark-count rate. This increase in dark count decreases the overall SNR of the system as well as dramatically increasing the bandwidth requirements of detector arrays.

Phototransistor

The phototransistor is a bipolar junction transistor (BJT) with a floating base node. Phototransistors are attractive because they incorporate the high front-end gain of a BJT, which can amplify the incident signal above the noise floor of the readout architecture. However, (except for vertical PNP in n-well bulk processes) because it requires a BiCMOS process it is not as common as the p-n junction which is present in all CMOS processes. Photons generate electron-hole pairs in the base, the base-collector junction and the base-emitter junction. For a PNP type phototransistor, electrons accumulated in the base raising the potential of the base. As the potential rises, holes from the emitter flow into the base and then into the collector and are

28

amplified by the static common emitter current gain. When operated in integration mode, the phototransistor will also have a gain that is independent of detector area.

1.3.4 Hybrid Detectors

Hybrid detectors are detectors with specialized absorption properties such as quantum-well infra-red detectors. These devices generally work in the same manner as silicon active pixel sensors and often rely on CMOS-based readout electronics. The advantage of theses systems is that they can provide application-specific absorption properties at the expense of increased complexity.

The work described herein uses a CMOS technology utilizing several active pixel designs while drawing comparisons to PMT and CCD designs and providing a theoretical framework that can be extended to CMOS readout structures for hybrid detector arrays.

Chapter 2

Contact Imaging

2.1 Introduction

Microsystem image sensors require aggressive system scale-down in all aspects. While conventional imaging systems can achieve micrometer to sub-micrometer resolution, these systems generally use magnifying optics. Optics introduce additional weight, size, complexity and cost to the system and therefore may be undesirable in many implantable situations. For some applications, such as identification of micro-sized particles, the spatial resolution afforded without additional optics may be sufficient. A method of imaging without intervening optics is known as contact imaging.

To avoid the need for intermediate optics while still achieving microscale resolution, the sample of interest can be placed directly on the sensor surface. The image can then be acquired by projecting light through the sample onto the sensor, or light emitted by the sample can be collected by the sensor. While these contact

imaging systems do not have the spatial resolution of conventional optics-based imaging systems, contact imaging presents an opportunity for imaging applications that conventional optical based systems cannot offer such as portable and implantable biosensors.

Contact imaging has been previously investigated [45–47] for various applications in structural analysis [48, 49], document imaging [50, 51], *in vitro* and *in vivo* biomedical imaging [52–66], as well as lab-on-a-chip systems [38, 41, 42, 67–75].

2.2   Theory

The primary difference between contact imaging systems and conventional imaging systems is that conventional imaging paradigms require the use of optical elements between the sample and the sensor array. An illustration of a representative conventional imaging system and contact imaging configuration is shown in Figure 2.1. In conventional imaging systems the object is illuminated by a source and optical elements such as lenses project and focus the object of interest onto the image plane of the sensory array. In contrast, contact imaging systems fall into two configurations that do not require any optical elements. In the first contact imaging configuration a light source illuminates an object closely coupled to the image sensor surface thereby blocking the light, while in the second configuration a luminous sample produces a bright spot against a dark background. In this work only the illuminated sample configuration of contact imaging will be examined.

In addition to the size, weight and cost benefits of contact imaging sensors,

(a) optical imaging system	(b) contact imaging system
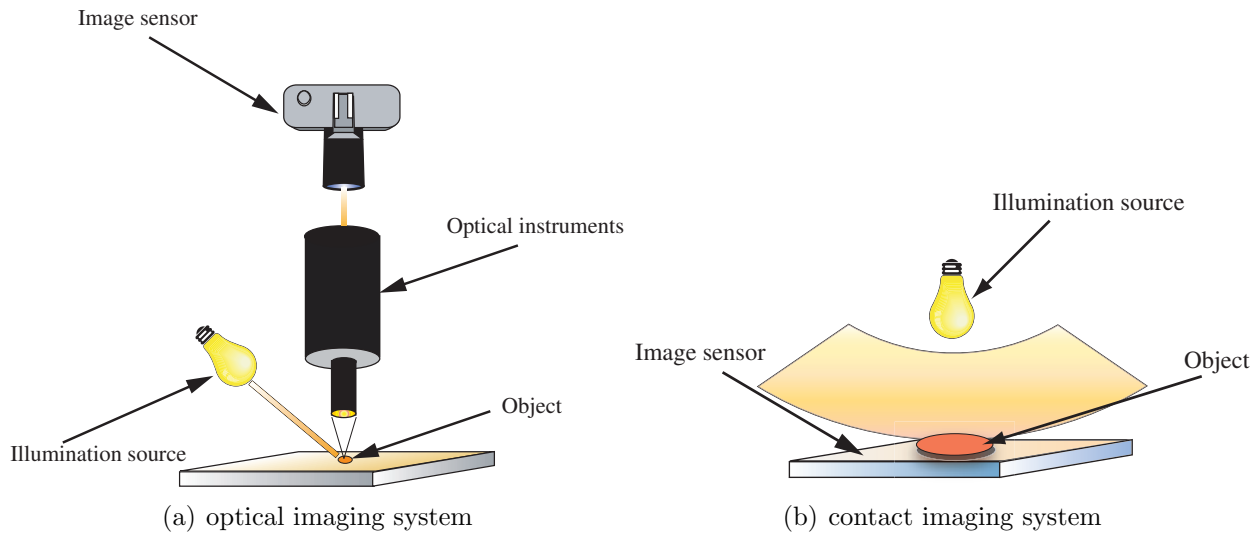
Figure 2.1: Imaging system configurations. (a) Conventional optical imaging system consists of a microscope projecting the image of an object onto a camera; (b) A contact imaging system where the object is placed directly on the sensor surface. [3]

another advantage of the contact imaging configuration is in collection efficiency. Collection efficiency describes the percentage of light emitted by a sample that is capable of being detected by the sensor. In conventional optical imaging systems, the working distance of the optics and object as well as the quality of the optical elements determine the collection efficiency.

When the sample is placed directly on the sensor surface, the collection efficiency can be nearly 50%. Salama *et al.* estimated that the optical efficiency of a contact imaging system is improved by 35 dB in comparison with a camera-based imaging system [74]. Signals such as fluorescence or bioluminescence are notoriously weak. Increase in collection efficiency can improve the detection limit of these weak signals.

The resolution of a conventional imaging system is primarily dictated by the effective pixel density in the sensor array. This increase in effective pixel density can be achieved by increasing the total number of pixels in the array and using optics to

32

project the image scene onto the array, or by decreasing pixels size to increase spatial resolution.

In contact imaging systems there are no optics; thus the spatial resolution of the projected image is solely determined by the pixel size. The active components within each pixel of a CMOS image sensor force a trade-off in spatial resolution, discussed above, and fill factor, the percent photo-active area and non-photo-active area within a pixel. Additionally, as pixel size decreases the dynamic range (DR) and signal-to-noise ratio (SNR) of the sensor decrease [76]. Therefore, there is a trade-off in spatial resolution with image quality when determining optimal pixel size.

Pixel size is but one of the factors that contribute to image resolution. In conventional imaging systems the resolution also depends on the diffraction limits imposed by the optical elements. Optical elements introduce diffraction in the system causing the image of a point source to have finite dimension. This finite dimension introduces a fundamental limit in the ability to discriminate between two spatially close point sources. In most conventional imaging systems, the optics are generally circular and are therefore well modeled by Fraunhofer diffraction at the aperture [77]. Under these constraints the minimum resolvable angle of separation between two point sources is determined by Rayleigh's criterion, and can be expressed as $\theta \approx 0.61\lambda/a$, where λ is wavelength and a is the radius of the circular aperture.

In contact imaging systems, spatial resolution is limited by near-field diffraction in addition to pixel size. The predominant factor that contributes to the near-field diffraction limit is the distance from the object to the image plane [77]. Using a molecular dye photo-transducing film to minimize the spatial quantization effects

33

of finite pixel size, Fisher *et al.* has demonstrated contact imaging with a spatial resolution of 50 nm [45, 46]. In practice CMOS image sensors will be limited by pixel size, distance between the object and the sensor surface, object optical density and object geometry.

2.3   Simulated and Experimental Results

The advantages and limitations of contact imaging have been examined through the simulation of ray tracing software and the use of CMOS image sensors [3]. Simulations used a commercially available optics simulator to examine different contact imaging configurations. Experiments were performed and compared against results collected from an image sensor from a commercially available CMOS process. These experiments examined the effects of particle size and position relative to the CMOS sensor. Both simulated and experimental results were analyzed to determine effects on contrast under each configuration. It has been demonstrated that contrast can be maintained if the particle size is larger than the pixel and remains close to the sensor surface. The results described herein indicate that contact imaging works well for detecting particles up to and beyond 100 μm, corresponding well with the dimensions of microfluidic systems.

2.3.1   Simulation

In one contact imaging configuration, light is used to project the shadow of an object onto a sensor array. In this configuration, the image quality is anticipated

to be a function of the distance between the object and the sensor surface, and the optical density of the object.

The optics simulator $LightTools^{TM}$ was used to model the effects described above. This optics simulator performs ray tracing in which simulated photons are sequentially generated randomly along the spatial extent of the source. The paths of these photons are calculated and recorded at the detector. In this way, the spatial arrival statistics are determined in the system. The geometric setup for the simulation of the contact imaging configuration is depicted in Figure 2.2. In this setup, a 2 mm × 2 mm Lambertian surface source emitting light at 550 nm is used to model the light source. A 550 nm light source was chosen because common contrast enhancement agents for biological cell detection such as neutral red stain are well characterized at this wavelength. The light source was used to illuminate an opaque 5 μm diameter circular disk where the distance between the light source and the object is denoted as D_{ls} and the distance between the disk and image plane is denoted as D_{obj}.

Symmetry in the system was exploited and only modeled one quadrant of the sensor surface to minimize simulation time while maintaining accurate results (Figure 2.2). A two-dimensional array of size 30 μm by 30 μm was used to emulate the image sensor. As mentioned above, the spatial resolution is determined by pixel size. In this simulation each pixel measures 0.85 μm by 0.85 μm.

System performance was quantified by the contrast (C). For this work, contrast is defined as $C = \frac{\left(m_{img} - m_{bkgrd}\right)^2}{\sigma^2}$, where m_{img} is the mean photon arrival count of the object image, m_{bkgrd} is the mean photon arrival count of the background excluding
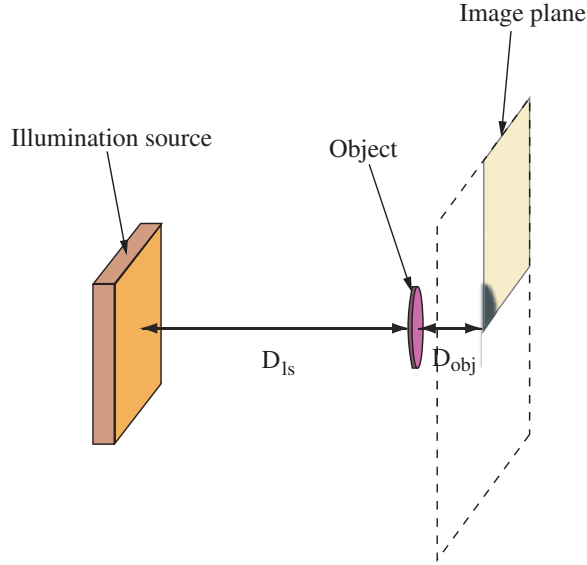
Figure 2.2: Simulated model of contact imaging system using the optics simulator $LightTools^{TM}$ (not to scale) [3].

the image of the object, and σ^2 is the background variance in photon arrivals. In this context, contrast serves the role of signal-to-noise power ratio for contact imaging systems, where a value of one indicates the minimum detectable signal. In simulation the background noise arises from the spatial uncertainty of the photon arrival process and follows Poisson statistics. As with all Poisson statistics, the variance increases linearly with the mean signal. Therefore, the noise power and SNR will increase with the number of photons captured by the detector array. This simulated noise follows the same distribution as the shot noise at the front end of physical contact image sensors. Since the SNR increases with an increase in simulated photons, the number of photons in the simulation affect the results. For the simulations herein, the same number of photons were generated under each condition to facilitate comparison of each configuration. In practice, sensor contrast is limited by the power supply rails, reset noise, readout noise, as well as the photon shot noise and is the square of the

sensor dynamic range.

An algorithm was used to determine the contrast of each simulated and experimental configuration. This algorithm incorporates prior knowledge of the system setup to aid in quantifying the contrast of each configuration. The image is considered to have three concentric regions: the object, the transition, and the background. For each simulation, the center of the object is fixed; while in the experimental configurations, the center of the object was determined by inspection. Additionally, the radius of each object is known *a priori* such that the object region is explicit. A sample set of background pixels are assumed to be close to the image boundary away from the object region. The background region is assumed to be pixels close to the edge of the frame determined by the following algorithm.

For each image the object region is darkest and becomes progressively lighter away from the object center. The center of the transition region was determined by finding the smallest radius of a two-pixel-wide annulus whose mean pixel intensity was greater than the average of the object pixels and background test pixels. Once the center of this transition region is determined, we locally sweep the annulus radius to determine the slope and intercept of the mean pixel intensity. The edge of the background region is taken to be the annulus radius in which the slope of the transition region intersects the mean sample background intensity. The contrast of each image was calculated using the mean and standard deviation of the object and background regions. Figure 2.3 shows a representative plot of the mean annulus intensity as a function of radius and illustrates the procedure used to calculate the intensities of the object and background, standard deviation of the background, and estimated radius
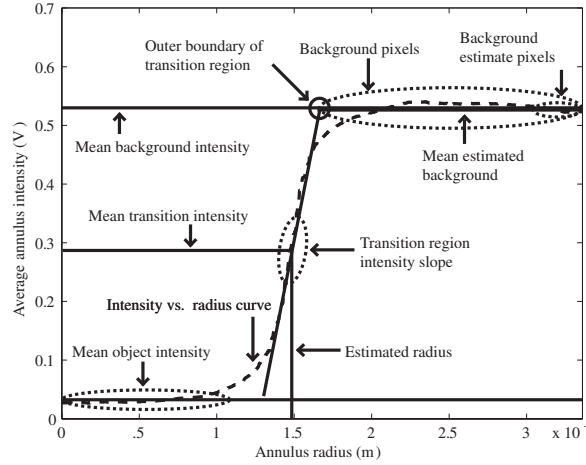
Figure 2.3: A representative plot of the mean annulus intensity as a function of radius and illustration of the procedure used to calculate the intensities of the object and background, standard deviation of the background, and estimated radius of the object [3].

of the object. The data shown in Figure 2.3 is experimental data from an image sensor array described in section 2.5.1.

Simulations were performed to analyze how the distance between the object and sensor surface, D_{obj}, affects image contrast when the light source is 100 mm away from the object. Three of the resulting 2-D histograms of photon arrivals are

| Contrast = 1846 | Contrast = 392.6 | Contrast = 12.18 |
| (a) | (b) | (c) |
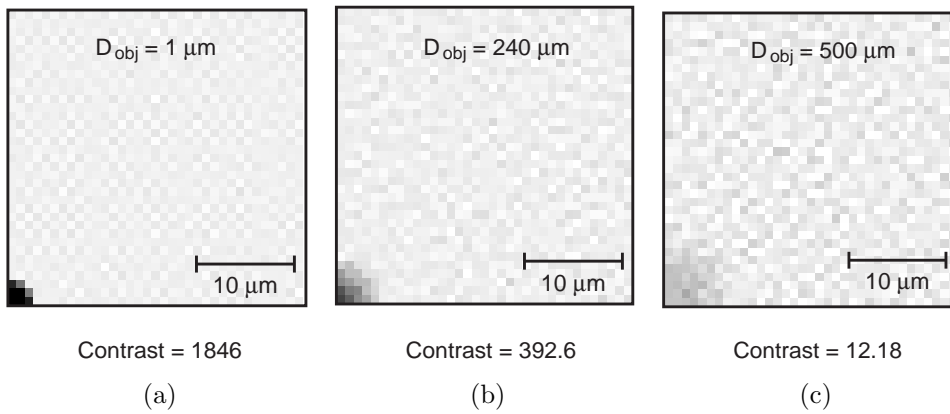
Figure 2.4: Simulated contact images of a quarter disk formed on image planes at (a) 1 μm, (b) 240 μm, and (c) 500 μm away from the disk [3].
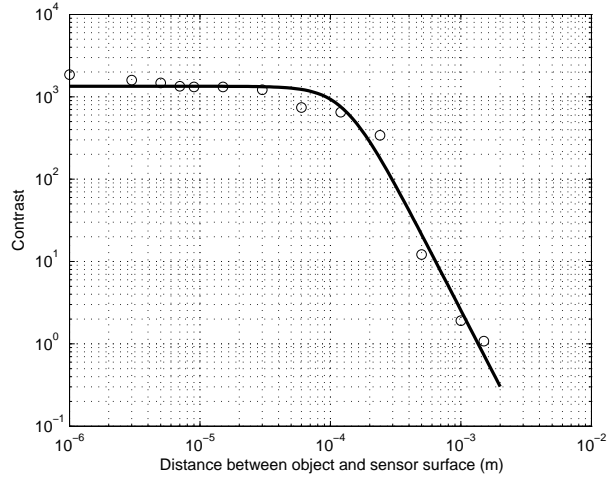
Figure 2.5: Simulated image contrast as a function of distance between the object disk and sensor surface. The Lambertian surface source is placed 100 mm away from the disk [3].

shown in Figure 2.4 with a D_{obj} of 1μm, 240μm and 500μm. It is clear that as the

disk becomes farther away from the image sensor surface, the contrast decreases. The

calculated contrast as a function of D_{obj} for each of the simulation are presented in

Figure 2.5. Simulated data points are depicted by open circles, and a best fit to

the equation $f(D_{obj}) = a/\left(1 + (D_{obj}/d)^n\right)$, is shown by the solid line, where D_{obj} is

the characteristic distance representing the distance at which the contrast starts to

dramatically decrease. Contrast is maintained up to $d = 130\mu$m from the sensor

surface to a 5 μm object which corresponds well to the dimensions of microfluidic

systems.

2.3.2 Contrast as a function of distance D_{obj} between object and sensor surface

2.4 Contrast as a function of distance D_{obj} for different optical densities

The simulations described in the previous sections modeled the object as completely opaque, absorbing any photons incident on the object. In experimental environments; however, most objects are not opaque and instead have a finite optical density. This finite optical density allows the transmission of photons through the object which is expected to decrease the apparent contrast of the scene.

A study of contrast as a function of distance between the object and the sensor was performed for three optical densities specified in absorbance per unit length: 3900/mm, 390/mm and 39/mm. These optical densities were chosen as representative optical density of biological cells. Biological cells stained with neutral red dye have an optical density of 390/mm, and the optical densities above and below are used to extrapolate the general properties of this configuration. The amount of light transmitted through the object is related to the object's optical density and thickness following Equation 2.1 where OD is the optical density, T is the thickness of the object, and Transmission is the percent of light able to pass through the object.

$$Transmission = 10^{-OD \cdot T} \tag{2.1}$$

In these simulations the dimensions of the object were the same as in the previous sections. The results are shown in Figure 2.6 and indicate that, as the optical density of the object decreases, the contrast of the object also decreases. This decrease in contrast is due to the fact that, as the optical density decreases, more light reaches the image plane. It is clear that, although the magnitude of the contrast differs, the trends of the contrast match closely with the previous simulations and experiments, with high contrast when the object is near the sensor surface and an abrupt drop off in contrast beyond a characteristic distance. According to our theoretical model, the curves of contrast as a function of distance for all three optical densities should be monotonically decreasing. Although these are simulated results, several non-ideal artifacts can be observed in the simulation sets. These non-ideal artifacts are primarily due to the simulated random process of the system, and arise when the sample size of the random process is small. Despite these non-idealities, each configuration provides a contrast greater than one, indicating that each of the objects can be observed. Theoretical modeling indicates that biological cells have sufficient contrast to be observed in the contact imaging configuration beyond 100 μm away from the sensor surface.
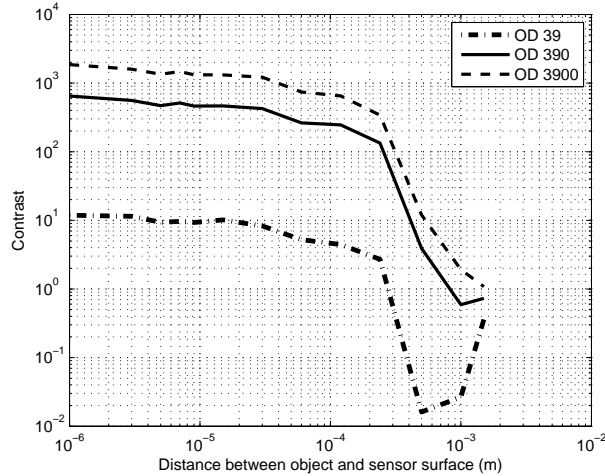
Figure 2.6: Simulated image contrast as a function of D_{obj} for different optical densities [3].

2.5 Contrast as a function of distance for different object geometries

The simulations in the previous section assumed that the shape and physical dimensions of the object were a cylindrical disk, 5μm in diameter and 1 μm thick. While these dimensions are similar to a biological cell spread along the surface of the detector, in practice a more realistic geometry is somewhere between a disc shape and a hemisphere. To assess the contrast as a function of geometry, a series of simulations were performed in which the geometry of a semi-transparent object was varied from cylindrical to hemispherical holding the optical density fixed at 390/mm.

The inset of Figure 2.7 depicts the variation in geometry, which was defined as equatorial slices of a sphere 5μm in diameter, with one face at the center of the sphere and the other face defined at a width between 1 μm (nearly cylindrical) and 2.5 μm (hemispherical) in increments of 0.5 μm. The distance from the object to

42
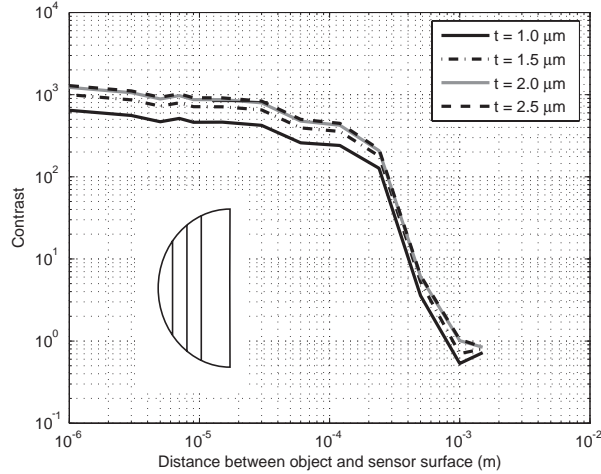
Figure 2.7: Simulated image contrast as a function of D_{obj} for different geometries [3].

the sensor surface, D_{obj} , was varied from 1μm to 2mm for each geometry. The results shown in Figure 2.7 indicate that contrast increases with object thickness. Again the highest contrast is achieved when the object is close to the sensor surface and the contrast decreases beyond 100 μm from the sensor surface. The increase in contrast due to geometry arises from an increase in thickness and hence optical absorption of the object, decreasing the number of photons reaching the image plane. These simulations match well with the prior simulations where it was apparent that the highest contrast was at the center of the object, therefore an increase in optical density at the center of the object should improve the contrast.

2.5.1 Contact Imaging Experimental Setup and Results

Two experiments were performed to corroborate the simulated results. These experiments looked at the contrast of two different sized micro-beads using a contact imager. The contact imager used for the bench-top experiments had pixel pitch of

7.4 μm a measured rms temporal noise of 2.5 mV with a maximum signal range of 1.2 V corresponding to a dynamic range of 53.6dB or a maximum contrast of 230,400. The first experiment varied the distance of a 48 μm diameter polystyrene micro-bead to the image sensor surface, while the second experiment used a 284.5 μm diameter stainless steel micro-ball as the object. An Axiotron microscope light source was used to illuminate the object. Each object was attached to a micro-pipette, and the micro-pipette was placed in a standard three-axis stage to control object-to-sensor distance. These experiments were different from the simulations in that the distance of the illumination source was 200 mm away from the sensor surface and not Lambertian, while the spectrum of the light source was broadband in wavelength.

Contrast analysis as a function of object-to-sensor distance was performed using the analysis described in Section 2.3.1. Representative examples of each captured image from each experiment are depicted in Figures 2.8 and 2.9. The upper half of each image was used in the contrast function to avoid distortion due to the micro-pipette used to control bead placement. Figure 2.10 shows the measured contrast as a function of distance. The circles represent the experimental data, while the lines represent a best fit to the equation $f(D_{obj}) = a/\left(1 + (D_{obj}/d)^n\right)$. The polystyrene bead has a characteristic distance of $d = 0.2679\ mm$, while the metal bead has a characteristic distance $d = 3.283\ mm$. These variations indicate the role of object size on contrast performance.

The experimental results show similar trends to the simulated results. The primary differences in these results are a variation in the maximum achievable contrast and contrast characteristic distance. The experimental results have a lower maximum
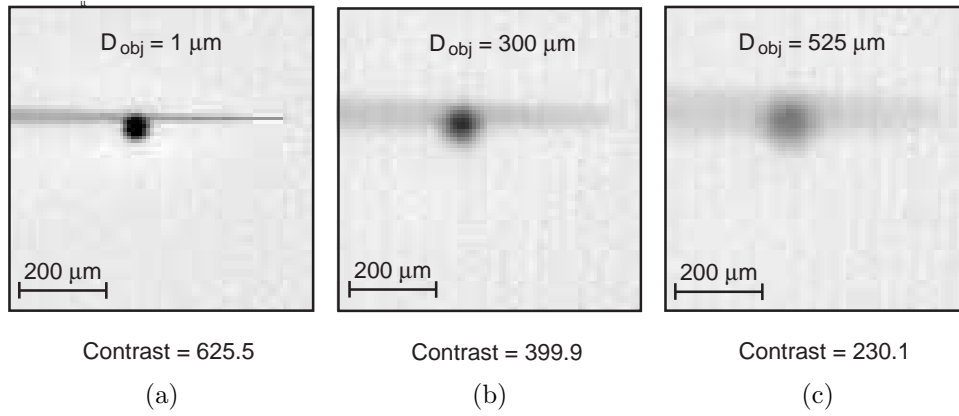
Figure 2.8: Images of a 48 μm polystyrene bead at (a) 1 μm, (b) 300 μm, and (c) 525 μm away from imager surface [3].
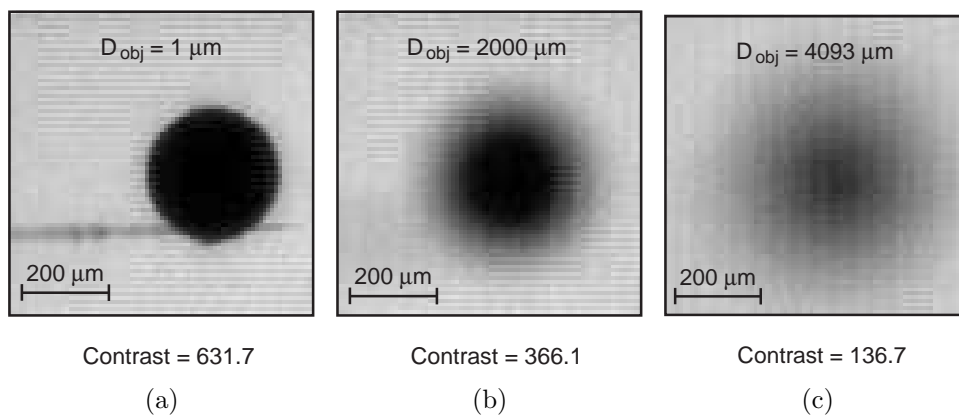
Figure 2.9: Images of a 284.5 μm metal bead at (a) 1 μm, (b) 1950 μm, and (c) 3950 μm away from imager surface [3].
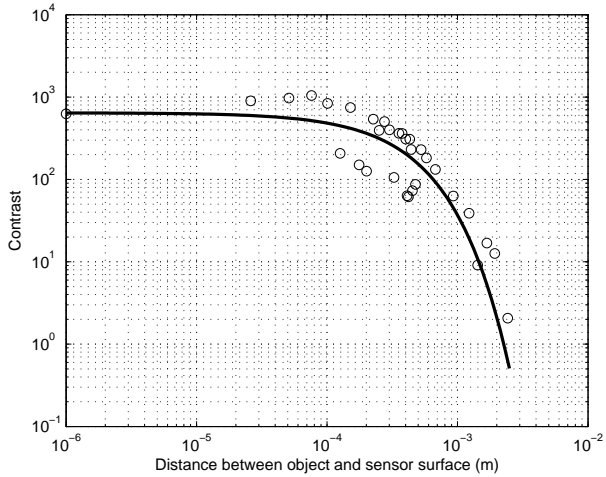
(a) Polymer microbead with diameter of 48 μm　　(b) Metal microball with diameter of 284.5 μm
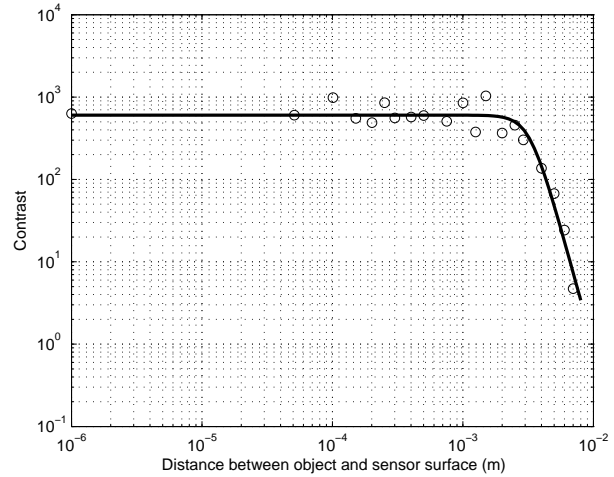
Figure 2.10: Measured image contrast as a function of distance between a small bead and the sensor surface, for (a) a polymer microbead with diameter 48 μm, and (b) a metal microball with diameter 284.5 μm [3].

contrast than the simulations despite having larger object size due to additional noise within the system. This lower contrast is a result of additional noise sources within the image sensor which degrade image quality such as reset noise, readout noise, fixed pattern noise.

2.6　Summary of Results and Critical Analysis

Contact imaging, imaging without optics, represents an attractive imaging paradigm, simplifying microscale systems by removing the optical elements between the sample and the image sensor. This simplification not only reduces the cost, weight, and size of microscale imaging systems; it also increases the collection efficiency through geometric advantage. The primary drawback of contact imaging over conventional systems is that spatial resolution is determined entirely by pixel size. Therefore,

46
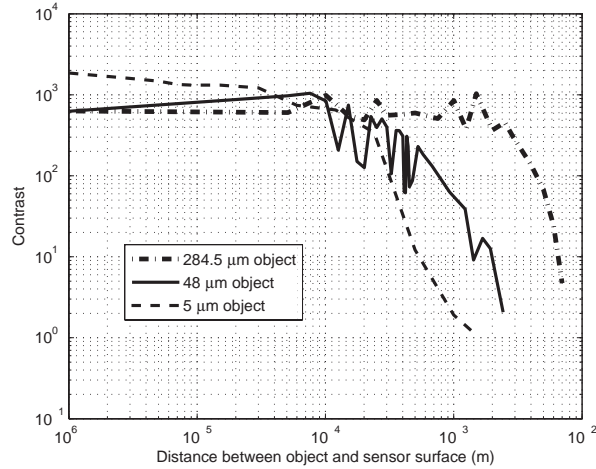
Figure 2.11: Simulated and experimental object contrast as a function of increasing D_{obj} [3].

it is necessary to determine the system limitations. The work described above was

conducted using the ray tracing simulator $LightTools^{TM}$ and experimentally verified

with a custom image sensor. The results show that contact imaging is achievable

for both synthetic particles and stained biological cells. The ray tracing simulations

not only demonstrate the trends in the relationship between geometry, size, optical

density, and distance of microparticles, but they also provide insight into contact

imaging performance as pixel size decreases with technology trends. The key results

of these studies indicate that sufficient contrast is maintained beyond 100 μm to de-

tect micron-sized particles such as cells, which coincides with the typical dimensions

of microfluidic systems.

Chapter 3

Active Reset in Address-Event Representation Imager Sensor Arrays

3.1 Introduction

In the previous chapter we examined the use of CMOS image sensors in the contact imaging configuration to detect micro-particles and biological cells. The focus of that chapter was examining the relationship between pixel size, particle size, and the distance between them. This chapter examines how asynchronous image sensor arrays can provide an efficient imaging alternative to conventional frame-based approaches for the application of micro-particle sensing steering and control.

3.1.1 Asynchronous Systems

Asynchronous systems generate most clocking signals on chip or *in pixel* and transmit signal information in the form of pulse modulation (inter-spike timing). When used in an array format, the event timing can be encoded in the coordinate address of the pixel. This signal representation is known as address-event representation (AER). The most common asynchronous imaging system is based on an integrate and fire design, whereby a signal is integrated and continuously compared to a threshold value. Once the threshold has been reached, the pixel initiates a continuous-time digital amplitude event, and the pixel is reset. The inter-event time encodes the photocurrent stimulus. An example of an array of asynchronous pixels is shown in Figure 3.1. Two pixels initiate events with time intervals t_{p1} and t_{p2} based on an integrated photocurrent. These events are encoded, transmitted off-chip and reconstructed based on their arrival times as shown in Figure 3.2. Many biological systems have similar pulse coding mechanisms and have been the focus of much research due to their efficiency, especially in the development of silicon retinas [78–83].
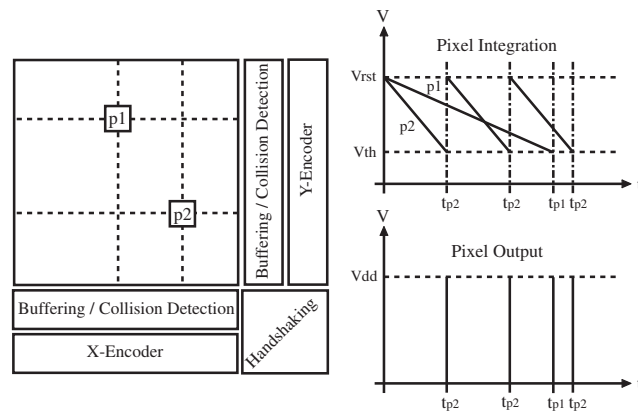
Figure 3.1: Example of address event representation (AER). a. Readout control block diagram. b. Example of initiated event in response to an integrated signal.
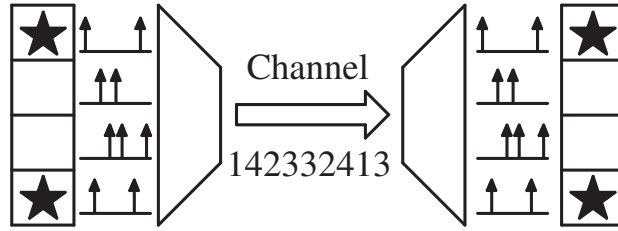
Figure 3.2: Example of an AER communication channel and reconstruction. Events occur in real time and are multiplexed across a communication channel. Reconstruction occurs based on the arrival time of each event recovering sensor information. [4]

In many experimental settings, data is sparse across the image array. In this context, sparseness implies that there are many pixels with little to no important information. Figure 3.3 depicts the results of an in-vitro experiment in which a small number of cells were placed on top of an image sensor in a contact imaging configuration. Under conventional frame-based imaging acquisition, every pixel in the array is quantized and transmitted to a computer for data analysis. Clearly, most of the pixels in the image do not correspond with the features of interest, such as cells, and are therefore not important. AER systems present an opportunity to analyze data only where interesting features exist. In severe resource-constrained environments AER can provide important power consumption and communication bandwidth advantages over traditional frame based systems.

Address event representation sensors attempt to ease data quantization and data transmission overhead by performing highly parallel pixel based filtering operations. Specific details of the image are extracted, and events are generated only when the pixel detects a particular salient detail. The address of the event is then trans-

50

(a) photograph   (b) captured image   (c) overlay
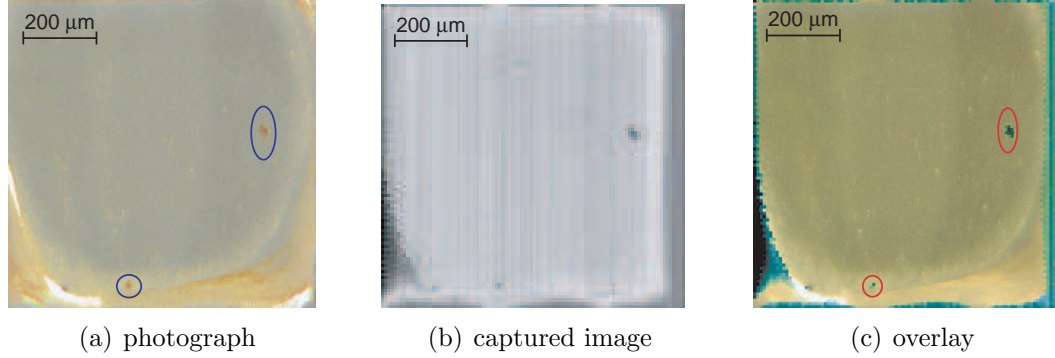
Figure 3.3: Pictures showing image sparseness of live cells coupled to a chip surface are taken using (a) a camera and (b) the contact imager. The overlapped view is shown in (c). [3]

mitted off-chip for further analysis. This asynchronous sensing method has several advantages over traditional methods. The first advantage is that a pixel only generates an event and requests access to the data bus when there is information of interest presented to the detector. This means that access to the bus is data dependent. In frame-rate imagers each pixel gets equal access time to the bus. As mentioned before, communication bandwidth is precious and the AER paradigm maintains maximum efficiency. Another advantage to this method is that the dynamic range is maximized for each pixel in the array. Traditional frame-based sensors require a fixed integration time for each pixel. If the integration time is too short, the signal may not be above the noise floor. If the integration time is too long, the pixel may saturate at the power supply rail. In either case the data is unusable. AER systems overcome this problem by initiating events only under specific conditions that precludes the aforementioned problems such as a voltage threshold crossing.

Although AER systems have advantages, they do not come without a price in terms of spatial resolution and complexity. The signal-to-noise ratio of the sensor

is dictated primarily by the timing and communication link properties of the sensor. Spatial resolution is important for contact imaging systems because such systems cannot afford high quality optical components. The spatial resolution therefore depends directly on pixel size.

Additionally, since pixels access the communication bus asynchronously, concurrent events cause collisions in data yielding unusable results. Biological systems commonly achieve asynchronous high-density massively-parallel computations. These systems are aided by high density three-dimensional interconnectivity. To compensate for a lack of high density connectivity a number of techniques have been developed. Although these methods differ they all trade physical connectivity for signaling speed. Although signaling speeds are higher than biological systems, collisions can still occur. When coincident or nearly coincident events are generated the signals will collide causing an error in the row or column address encoding. To deal with this problem, collisions can either be discarded, error corrected, or arbitrated.

The first biologically inspired technique developed by Mahowald and Mead uses a binary tree competition circuit to arbitrate between simultaneous events [84]. In this design the row and column addresses are transmitted off-chip in a serial manner. Boahen has analyzed this design in terms of its key trade-offs including: capacity, latency, temporal dispersion, and integrity [4]. Capacity is the maximum rate at which spikes can be transmitted, while latency is the time it takes to send two points. Temporal dispersion is the standard deviation in the latency, and integrity is the number of spikes that are successfully transmitted. A subsequent revision by Boahen increases the capacity and latency by using a greedy-fair arbiter which services events

in the same row or column before servicing other events, and transmits the addresses in a word-serial fashion [85–87]. In this arbiter, coincident or nearly coincident signals are queued and accessed in a nearest neighbor fashion to reduce redundant address data transmission. For example, if two pixels from the same row produce coincident events, first the row address is transmitted off chip, then the column address of the first event, and then the column address of the second event. The architecture is termed greedy-fair because if many events are in the queue, and another event enters the queue, the later event may get accessed prior to an event already in the queue. However it guarantees that the same pixel event cannot gain access to the readout bus twice until the entire arbitration tree has been cleared. This prevents a few highly active pixels from dominating the entire bandwidth of the sensor. This contrasts with prior architectures in which the row and column addresses are transmitted for every event.

Other biologically inspired systems use analog winner-takes-all (WTA) arbitration. Andreou *et al.* proposed using a two stage WTA to detect the first event, and latch the inputs until the end of the communication cycle [88]. Yet another access method is the use of priority encoders to perform arbitration in a predetermined manner, whereby each pixel is assigned priority a-priori. If a pixel of high priority enters the queue while another pixel has access to the bus, the pixel with higher priority will take control of the bus causing data errors. This can be mitigated with latching inputs during the communication cycle. A remaining drawback of this system is that when a few pixels of high priority dominate the output bus, and low priority pixels may never get served.

Culurciello *et al.* analyzed the theoretical latency, throughput and collision probability as a function of sensor array size for scanning, arbitrated, ALOHA, and priority encoding systems [89]. He concluded that ALOHA-based sensors provide superior performance for low to moderate array sizes (less than 10^5 pixels), while arbitrated systems excel with larger format arrays (greater than 10^5 pixels).

Culurciello *et al.* uses an ALOHA access method in which every pixel can directly access the readout bus without arbitration. The advantage of this method is decreased latency and therefore higher capacity and lower probability of collision. In this configuration collisions can still occur. A collision detection circuit determines whether two or more pixels access the bus at once and transmits an invalid bit if there are collisions. [90–92].

Another way to mitigate data errors resulting from collisions is to use error correction coding. Brajovic proposed using a syndrome event encoder to encode simultaneous events [93]. Essentially, redundancy is built into the encoding to determine which multiple events have occurred at the expense of larger code words. This may be useful for wireless devices where the latency introduced by longer codes may be less than that introduced by transmitting multiple events individually. Additionally, this allows error correction codes to be integrated to prevent signal corruption along the communication link.

3.2 Pixel Design

The pixel described herein incorporates an active-reset technique into an event-based readout architecture. As technology sizes decrease, the full well capacity (total number of photons captured before saturation) of image sensors also decreases due to the increased front-end gain. While the full well capacity decreases, the reset noise becomes a larger fraction of the full well capacity. It has been demonstrated that an active-reset technique can minimize the reset noise in image sensor arrays [22, 23].

The pixel schematic of the analog and digital portions of the pixel is shown in Figure 3.4, with a description of each portion to follow.
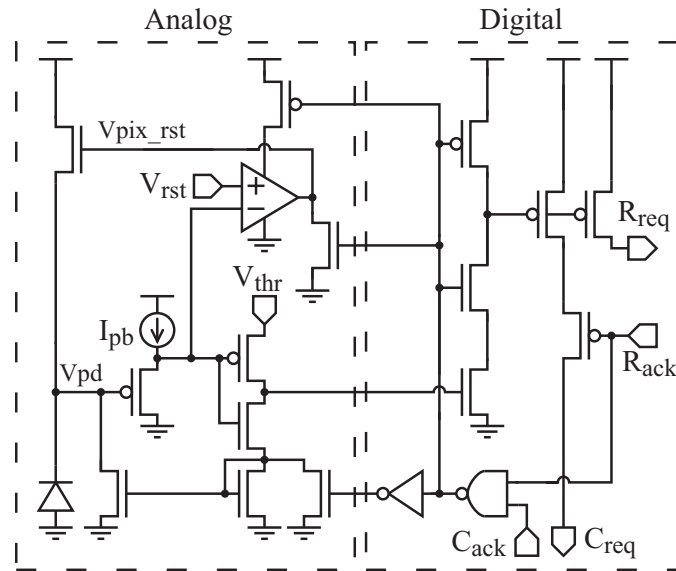
Figure 3.4: AER Active Reset Pixel

The reset noise contributes to uncertainty in the number of initial charges at the reset node. For integrate-and-fire systems the reset noise uncertainty translates directly into an uncertainty in the amount of time it takes to read a pre-defined threshold.

The variance of the integration process with reset noise is found using the law of total variance derived from the law of total expectation in Equation 3.1.

$$
\begin{aligned}
X &= \sum_{i=1}^{N} Y_i; Y_i \sim exp(\lambda) \\
VAR[X] &= E[X^2] - E[X]^2 \\
&= E\left[X^2\right] - [E[X]^2 \\
&= E\left[Var\left[X|Y\right] + E[E[X|Y]]^2 \\
&= E\left[Var\left[X|Y\right] + E[E[X|Y]^2]\right] - E[E[X|Y]]^2 \\
&= E\left[Var\left[X|Y\right]\right] + (E[E[X|Y]^2] - E[E[X|Y]]^2) \\
&= E\left[Var\left[X|Y\right]\right] + Var[E[X|Y]] \\
&= \frac{VAR[N] + E[N]}{\lambda^2}
\end{aligned}
\tag{3.1}
$$

where λ is the electron generation rate, E[N] is the total number of electrons required to generate an event, Var[N] is the reset noise which is related to the reset noise kTC, where k is Boltzmann's constant, T is the temperature in Kelvin, and C is the integration capacitance.

An AER system that uses the inter-arrival time as a measure of light intensity has several sources of noise. AER noise sources are similar to those of standard imaging system noise sources. However, their effect is viewed as a variation in the inter-arrival time rather than voltage. This variation inter-arrival time leads to an interesting situation when compared to integration-based systems.

Timing jitter occurs along the readout path, and therefore is independent of the electron arrival rate at the input. This implies that as the light intensity increases, the effects of timing jitter degrade the SNR. For a single sensor the resulting SNR is defined in Equation 3.2.

$$SNR = \frac{(V_{thr}C_{int}\frac{q\lambda_{ph}}{(q\lambda_{tot})^2})^2}{\sigma_{readout}^2 + \frac{\frac{kTC_{int}}{q^2} + \frac{V_{thr}C_{int}}{q}}{\lambda_{tot}^2}} \tag{3.2}$$

where, V_{thr} is the event threshold in volts, C_{int} is the integration capacitance, q is the electron charge, k, is Boltzmann's constant, T is the temperature in Kelvin, λ_{ph} is the electron generation rate due to photons, λ_{tot} is the total generation rate (dark current and photocurrent) rate, and $\sigma_{readout}$ is the timing jitter along the readout path. For an array of sensors the timing jitter will become a function of the number of pixels and event time.

3.3 Array Architecture

The array architecture follows that proposed by Boahen *et al.* [4] The primary difference is that rather than providing a purely digital reset signal and an analog reset value is multiplexed to the appropriate pixel using an arbitration circuit. The arbitration circuit latches the requests and then uses an arbitration tree to select one of N requests. The selected row allows each activated pixel in that row to propagate a column request signal to an identical column arbitration circuit, where a single column is selected, encoded and allows the selected pixel to be reset. Representative

reset and readout signal traces are shown in the Figure 3.5. The pixel array uses active high requests, and active low acknowledges.
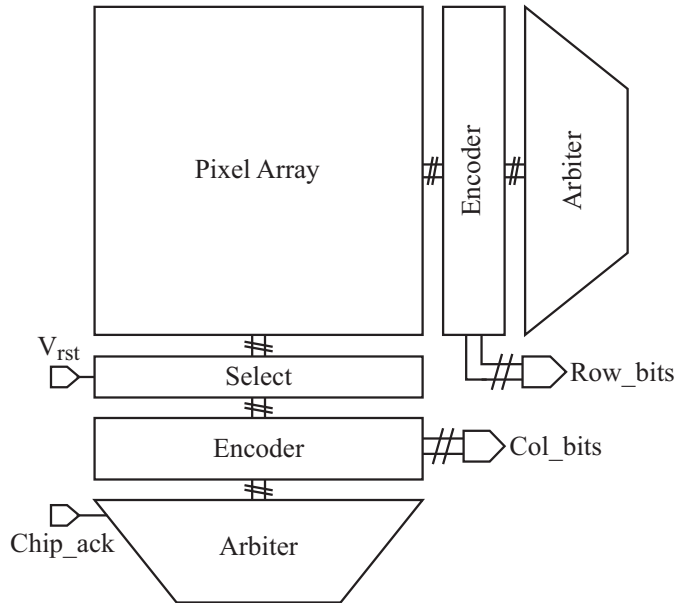
Figure 3.5: AER Active Reset Pixel Array

The timing diagram for the system is shown in Figure 3.6. The photodiode node integrates the accumulated photocurrent. Once the appropriate threshold is reached, feedback pulls the photodiode node to ground. This triggers the row request (R_{req}) pulling the row request line high. The row request signal is arbitrated and served returning an active low signal (Rack) to the pixel. This row acknowledge triggers a column request (C_{req}) that pulls the column line high. The active column lines are then arbitrated, and a column acknowledge, active low, is propagated back to the pixel array. The column acknowledge activates a transmission gate allowing an analog reset to propagate column-wise to the selected pixel.

The in-pixel amplifier drives the NMOS reset transistor in the pixel and monitors the photodiode node through a source follower buffer amplifier at the negative node

58
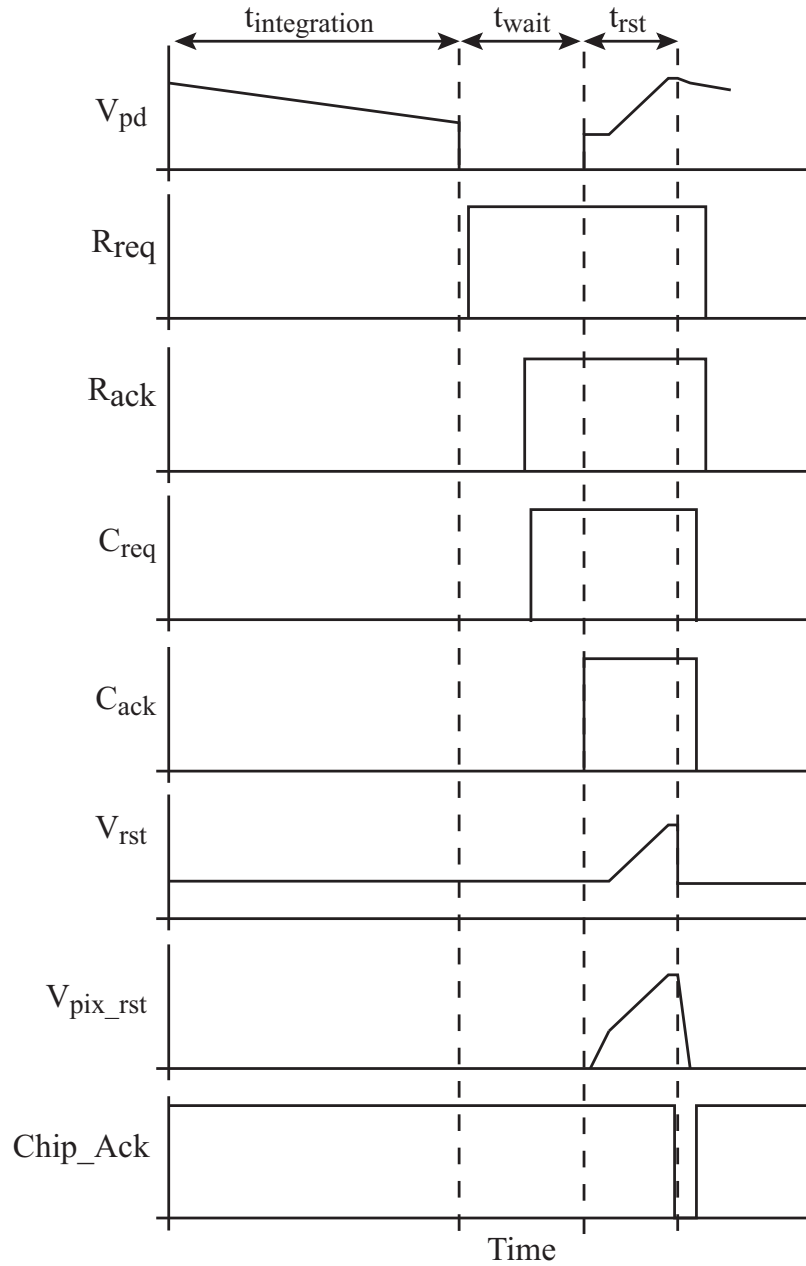
Figure 3.6: Timing diagram of active-reset AER pixel array. The photodiode voltage decreases with incident light and when it reaches a specific threshold generates a row request ,R_{req}, to the row arbiter. The row arbiter sends a row acknowledge, R_{ack}, and the pixel sends a column request, C_{req}, to the column arbiter. The column arbiter sends a column acknowledge, C_{ack}, to the pixel. The active reset signal, V_{rst}, propagates to the pixel and produces a pixel reset voltage, V_{pix_rst}, resetting the photodiode voltage to the specified reset level. A chip acknowledge signifies the entire cycle is complete.

of the pixel.

The purpose of the PMOS source follower is to buffer the photodiode node from the input amplifier capacitance and additional event generator capacitance. The effectiveness of the active reset topology is inversely proportional to the photo-diode capacitance. The smaller the capacitance, the larger the reset noise, and the better the feedback amplifier can control the noise. For smaller technologies this additional amplifier would not be necessary and would dramatically reduce the power consumption of the system.

Each pixel is 35 μm x 35 μm with a fill factor of 4%. A centroid approach is taken in the layout with four pixels, each reflected about the x- and y-axis. This layout technique allows for a more-compact layout implementation at the expense of regular pixel pitch, which can contribute to image irregularities.

3.4   Experimental Results

A 22 x 22 pixel array was fabricated in a 0.5 μm commercially available CMOS process. Figure 3.7 shows a photomicrograph of the chip. A custom Labview program was written to asynchronously interface with the imaging chip. For analysis purposes the address and time-stamp of each event were recorded.

To assess the SNR of the system, the mean inter-arrival times and standard deviation in those arrival times were determined as a function of illumination intensity. The experimental setup used to obtain these measurements is shown in Figure 3.8 A grating monochromator (Cornerstone 620, Newport Oriel Inc.) was used as a
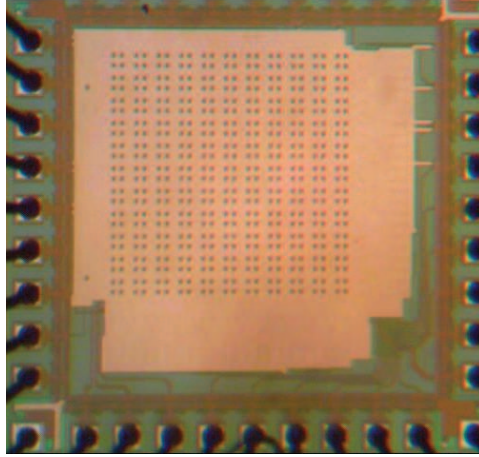
Figure 3.7: AER Chip Photograph

light source. A 20 nm slit assembly was used to obtain high optical power without sacrificing resolution at a center wavelength of 508 nm. The output light from the monochromator was directed into the integrating sphere through a fiber-optic coupler to minimize thermal coupling from the monochromator to the sensor. Illumination power was controlled by inserting neutral density filters between the output of the monochromator and the input port of the integrating sphere to obtain the specified light intensities. The chip was mounted to the output of the integrating sphere. A similar configuration is be used for all intensity based bench-top measurements throughout this work.

When the illumination intensity is low, the inter-arrival times are determined primarily by the integration of thermally generated dark current. Because this generation process follows Poisson statistics, there is interment variability in the inter-arrival times. As the illumination intensity increase, the mean inter-arrival times decrease data collisions begin to occur. Because the architecture uses an arbitration circuit, each event is queued and will eventually be read out, but the mean and standard
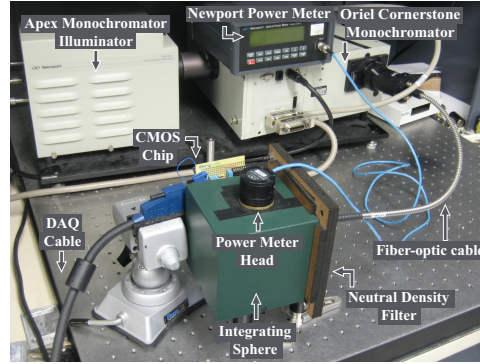
Figure 3.8: Experimental Test Setup to determine device properties as a function of spectrum and illumination intensity.

deviation of these readout times increases. Eventually, this queued readout time becomes the dominant process in the system. The results of the mean and standard deviation of the pixel inter-arrival times are shown in Figure 3.9.
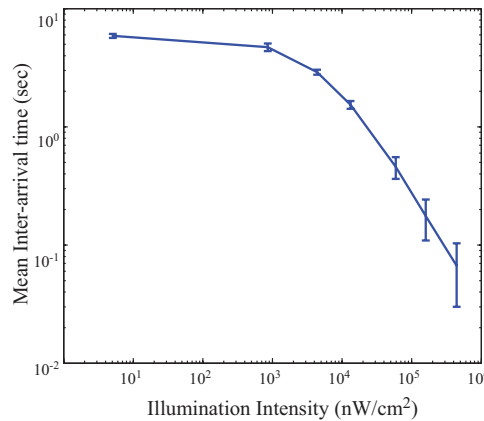
Figure 3.9: AER array mean pixel inter-arrival time as a function of incident illumination intensity.

A 508 nm wavelength beam of light was produced and filtered by a Newport Monochromator with a 10 nm slits. The light was coupled to an optical fiber and subsequently focused using a lens and mechanical iris. The beam was then moved across the image array to simulate the response from a fluorescent micro-particle. The test setup used to model a fluorescent micro-bead as a narrow beam of light is shown

in Figure 3.10. The beam of light was moved across the image plane to represent a moving fluorescent micro-particle in a microfluidic system. Timestamps for each event were recorded and the inter-arrival times were analyzed. Figure 3.11 shows four "frames", or "images" produced by the AER sensor. The intensity of these images are inversely proportional to the inter-event interval and normalized such that the maximum value is 256 to maximize the image dynamic range.
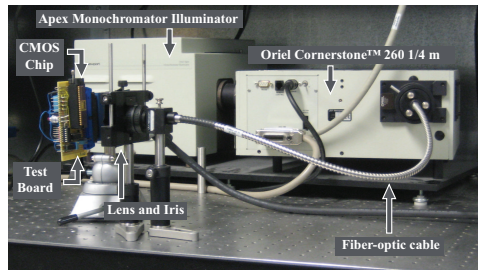
Figure 3.10: Experimental test setup used to model fluorescent microbeads as a narrow beam of light.

As previously mentioned, one of the main advantages of AER image sensors is that they are extremely bandwidth efficient when imaging sparse scenes such as a bright spot against a dark background. For example, the average inter-arrival times for pixels outside of the main spot is 4 sec, while the average inter-arrival time for pixels inside the main spot are 0.33 seconds. Therefore the total average event rate is 285 events/sec. Given that each event requires 10 bits to adequately encode the pixel address, the total average bit-rate for the scene is 2850 bits/sec.

In comparison to an 8-bit frame-based system with 484 pixels, obtaining 3 frames/sec would be an equivalent bit rate of 11,616 bits/sec. If a standard frame-based imaging system provides 1-bit resolution, the average bit-rate would be 1452 bits/sec. While this 1-bit resolution system is more efficient in terms of bandwidth,
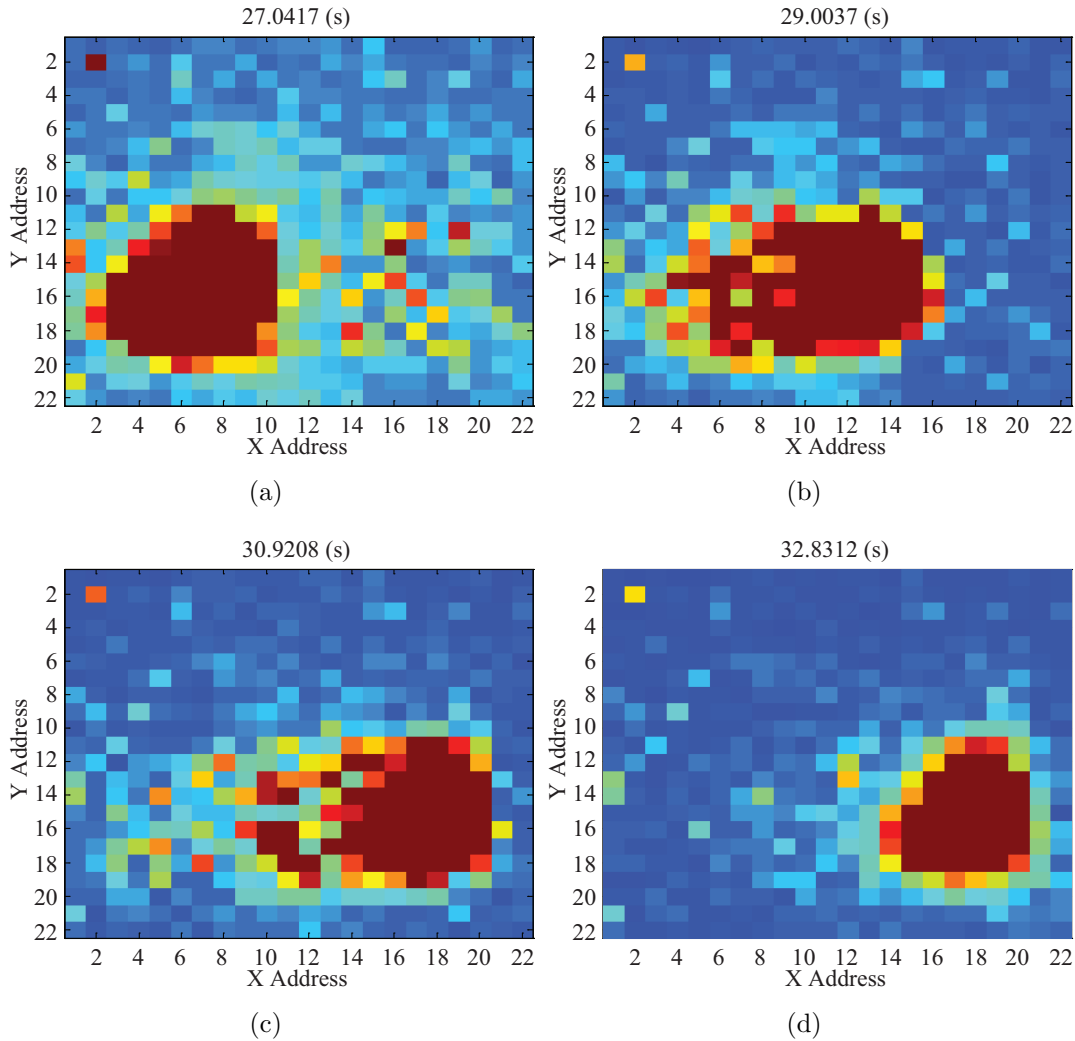
Figure 3.11: "Images" of the last time stamp of each pixel.

it requires precise thresholding.

Another advantage of AER systems is that they allow for real-time processing on a pixel-by-pixel basis. One of the most common tasks associated with particle-tracking is determining the center of mass for the image. The center of mass is defined in equation 3.4 where the summation occurs over the entire frame. Where C_x is the center of mass for the image in the x-direction, C_y is the center of mass for the image in the y-direction, X_{add} is the address of the selected pixel in the x-direction, Y_{add} is

64

the address of the selected pixel in the y-direction, $I_{X_{add},Y_{add}}$ is the intensity of the pixel with address X_{add} and Y_{add}.

$$C_x = \sum_{X_{add}} \sum_{Y_{add}} X_{add} I_{X_{add},Y_{add}} \tag{3.3}$$

$$C_y = \sum_{X_{add}} \sum_{Y_{add}} Y_{add} I_{X_{add},Y_{add}} \tag{3.4}$$

For an asynchronous sensor we can formulate a similar equation, but instead represent it as an IIR filter. IIR filters provide significant computational savings and provide a conveniently methodology for data-driven analysis.

$$C_{x\_t+dt} = e^{-\alpha dt} C_{x\_t} + X_{add} \frac{1}{dt_{X_{add}}} \tag{3.5}$$

$$C_{y\_t+dt} = e^{-\alpha dt} C_{y\_t} + Y_{add} \frac{1}{dt_{Y_{add}}} \tag{3.6}$$

3.5 Extension to First-Time to Spike Image Sensors

Typically AER sensors implement rate based encoding. While this method allows the efficient encoding of sparse scenes, it heavily weights resources to areas of highest illumination intensity. While these data-driven designs are efficient, they can present problems when utilized in control-based systems since there is no guarantee that the requisite data is generated within the necessary time interval to take action.

For the application of micro-particle steering this is particularly troublesome. The pixel firing rate is dependent upon the illumination conditions. The electro-osmotic flow moves the micro-particle in reference to the image sensor output and desired direction. If the sensor output rate is too slow, the particle may overshoot its desired position, or worse leave the observable area in the microfluidic channel. A complimentary strategy is the use of a first-time to spike image sensor originally designed by Xiaochuan et al [94]. Recently neuroscientists have observed that human reactions to images occur within 2 ms. This time-frame is too short for the brain to process every spike from every retinal cell. Consequentially these neuroscientists have formulated a theory that the brain responds not to all the spikes in a spike train, but the first arrival of a spike train. Harris et all has used these principles to design a first-time to spike image sensor array. This sensor uses an asynchronous readout structure with in-pixel comparator similar to standard AER sensors, however, the pixel array is reset periodically by only a global reset signal whereas most AER sensors have event generated reset mechanisms. The advantage of this design is that the firing rate is still sparse, whereby the global reset can be used to reset low-intensity pixels before they fire, and high-intensity pixels do not necessarily use the majority of the system resources. Furthermore, Xiaochuan *et. al* have incorporated a dynamic threshold into their design. By providing a ramp threshold, they can augment the dynamic range of the system to ensure that any incident illumination intensity will cause a response within the given required frame rate. Illumination intensities, are then estimated based on the time of the threshold crossing, and the voltage threshold at the time of the threshold crossing. Using a first-time-to spike imager, it is possible to ensure a

specified frame-rate for the control algorithm while maintaining the sparseness of an AER system. In future work the active-reset technique demonstrated in this chapter will be implemented in a first-time to spike architecture. A first time-to-spike image sensor with a dynamic threshold will benefit from reduced reset noise and hence reduced timing jitter for low-light-level scenes. Since the voltage threshold V_{th} goes to zero for low-light level scenes the timing jitter tends towards only a function of the readout path jitter and the reset noise as a function of voltage ramp speed.

3.6   Summary of Results and Critical Analysis

Unfortunately not all aspects of the system worked as designed. The primary disappointment was the failure to suppress reset noise using the active reset circuit. Many AER systems are designed for extracting a particular salient features from an image rather than noise performance considerations; however, all integration based sensors suffer from fundamental noise sources including reset noise. Reset noise arises from the uncertainty in the number of charges on a sample-and-hold node due to thermal fluctuations and becomes more pronounced as the integration capacitance decreases. Looking toward semiconductor technologies with smaller and smaller feature sizes and therefore smaller and smaller capacitances, reset noise is expected to become a significant problem for AER systems in future technologies.

While similar frame-based reset noise circuits have been demonstrated, this is the first work to attempt an active reset in an asynchronous readout-based sensor. Unfortunately noise suppression was not achieved for one of several reasons: 1. En-

vironmental noise interference - Reset noise is on the order of 500 μV. While this noise is significant, environmental noise such as power supply fluctuations or other electromagnetic interference can be on the order of 1 mV, effectively masking any reduction in reset noise. In the future further electromagnetic shielding will be introduced. 2. Reset voltage ramp - The reset ramp voltage was produced by a USB data acquisition card. This ramp signal may suffer from power supply fluctuations in the DAQ. 3. Reset amplifier - Each pixel has an in-pixel amplifier to deliver the reset ramp voltage to the pixel. To save power, the amplifier power supply is gated with the row and column acknowledge signals. Each time the pixel is reset, the amplifier is turned on and off. It is possible that the amplifier cannot reach equilibrium in the reset period. Alternatively the amplifier also starts with the negative terminal voltage outside the input range, effectively saturating the device. This may exacerbate the amplifier equilibrium issues. Future design iterations will include tighter timing constraints on the amplifier design to ensure functionality. 4. Clock feed-through - The reset signal drives the gate of an NMOS device while the source of the NMOS device is the integration node. When the voltage ramp abruptly falls, capacitive coupling between the gate of the reset transistor and integration node will pull the integration node towards ground. If this coupling is large enough, it will introduce variability in the reset voltage. This problem may arise due to the small active area of the device. As mentioned above, reset noise only becomes pronounced for small values of integration capacitance, which occur in advanced technologies. To simulate these small capacitances in a 0.5 μm technology, the active area of the pixel was drastically reduced and is therefore not the dominant capacitance at the integration node. This

causes the effect of clock feed-through to appear larger than in more advanced technology where the reset transistor would also be scaled in size. Future studies should implement this pixel in a small feature-size process to assess performance.

Another disappointment was that the sensor was unable to effectively image micro-beads for micro-particle control. The sensor was integrated with a bench-top microfluidic system similar to that described by Probst *et al.* [95]. The microfluidic chamber was placed on a Nikon Eclipse TS100 inverted microscope with 20x Plan Fluor objectives. 5 μm fluorescent micro-beads with 468 nm excitation and 508 nm emission spectra were loaded into the microfludic chamber. The AER array was mounted to the camera port of the microscope. While micro-beads in the reservoir ports could be observed with the sensor, imaging a particle in the chamber was difficult. The primary difficulty with the system was that the array size was small (22 x 22 pixels) and that the active area of each pixel was small. This made locating a single bead in the reservoir very challenging, since the total active area of the device is at most 22 times larger than a particle if the particle is on a single pixel, and at most 10 times larger than a particle if the particle is covering a 2 X 2 set of pixels. Not only does this make finding the particles difficult, but since the microfluidic control algorithm must be aligned to the orientation of the sensor in a specific location within the chamber, particle steering could not be demonstrated. Future generations of this chip will increase both the active area of the sensor as well as the array size. Increasing the chip from a 1.5 mm X 1.5 mm die to a 3 mm X 3 mm die, the array size can be increased to 64 x 64 pixels, a factor of 9 increase in the overall observable area.

Severe resource constrained environments require alternative imaging solutions

Table 3.1: Summary of AER Pixel Characteristics

Technology	0.5 3M 2P μm CMOS
Power Supply	5V
Array Size	22 (H) x 22 (V)
Fill Factor	4%
Pixel Reset Time	20 μsec
Bandwidth	120 - 22K events/sec
FPN (STD/Mean pixel-pixel) in Dark	1.2 sec

to standard frame based sensors. AER systems are one such sensing architecture that provides a method for data driven sensing that enhances bandwidth performance, reduces power consumption, and subsequent computational load. In this chapter an asynchronous address event representation image sensor array was proposed for micro-particle imaging. A 22 x 22 pixel AER array utilizing an active-reset topology to minimize reset noise and increase the overall SNR of the system was compared to the traditional AER arrays which use a hard-reset topology. The sensor was experimentally verified by observing a 508 nm wavelength spot moving across the focal plane and demonstrated a 4X reduction in bandwidth compared to a standard 8-bit frame based sensor. The fabricated device will be integrated into a contact imaging micro-particle steering system.

Chapter 4

Differential Active Pixel Sensor

4.1   Introduction

Differential sensor topologies are a well known technique for suppressing correlated noise. This section examines the design, model and experimental noise performance from a differential photo-sensor fabricated in a 0.5 μm commercial CMOS process. The sensor is a novel differential active pixel sensor which performs in-pixel correlated double sampling (CDS) to reduce correlated and environmental noise at the expense of increased thermally generated noise sources such as reset and readout noise compared to a comparable single-ended sensor.

4.2   Design and operation

Figure 4.1 shows the schematic of the sensor which was previously reported [42, 43]. Here a thorough noise analysis and experimental characterization is presented.

The theoretical and experimental noise was compared against a similar single ended

pixel shown in Figure 4.2. Both pixels have identical sizes for all transistors and

identical active-area for the p^+/n_{well} reversed bias photodiode.
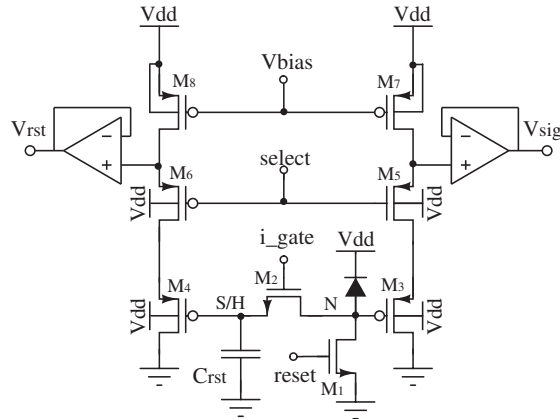
Figure 4.1: Differential sensor and readout chain schematic
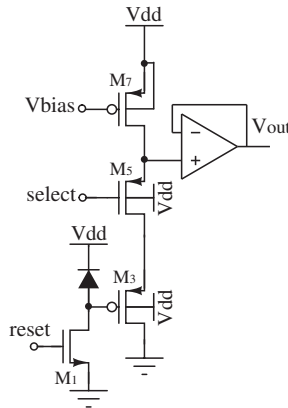
Figure 4.2: Single-ended sensor and readout chain schematic

Transistors M_1 and M_2 represent the reset transistor and sample and hold tran-

sistor respectively. Upon reset transistor M_1 and M_2 are turned on resetting both the

integration node (V_p) and the sample and hold node (V_m) potentials to 0 V. Both

transistors are turned off, and the integration node rises due to the photocurrent

generated in the reverse biased p^+/n_{well} photodiode. At the end of the integration cycle, both the voltage at the integration node, and the voltage at the sample and hold node are read out in parallel, providing noise immunity. The pixel is read out by turning on the PMOS source followers comprised of M_3, M_7 and M_4, M_8 with transistors M_5 and M_6 acting as row select switches giving access to the column bus. NMOS input differential pairs in a unity gain configuration buffer the signal off-chip.

4.3   Noise analysis

To understand the noise of this differential topology, reset and readout noise were examined. Theoretical reset noise contribution due to thermally generated fluctuations were examined at the sample-and-hold node and at the integration node. The theoretical noise due to the readout chain was then calculated including thermal and shot noise but ignoring fixed pattern noise due to fabrication mismatch. The primary readout noise contribution comes from the source follower and the unity gain buffers. The total noise in the system is reported as the root mean square of the noise with units of volts.

4.3.1   Reset Noise

Reset noise is due to random fluctuations in electrons in the parasitic resistive elements and their subsequent integration onto a capacitive node. This is commonly referred to as kT/C noise because of its form. Reset (kT/C) noise is often the largest of the thermally generated noise sources, because it is inversely proportional to the

capacitance at the sensing node (which is generally small). Therefore the reset noise in this system is dominant at the sample and hold node as well as at the integration node. Figure 4.3 shows the parasitic elements present at these nodes. The parasitic elements include gate to channel capacitance, gate to source overlap capacitance, gate to drain overlap capacitance, as well as junction capacitance from the source to substrate. Estimates for these parasitic capacitances are shown in Table 1.

At the sample and hold node (V_m) there is equivalent capacitance of 36 fF (C_{S/H_EQ}). This results from the gate source overlap capacitance, gate drain overlap capacitance, and gate to channel capacitance of the PMOS. In addition, there is a gate to source overlap capacitance associated with the I_{gate} switch, and junction capacitance associated with the parasitic n^+/p_{sub} parasitic diode (C_{pd}). The explicit capacitor is 20.8 fF, and the parasitic elements contribute an additional 15.2 fF.

Figure 4.3: Parasitic devices at the integration and sample-and-hold nodes of differential sensor

At the integration node, once again there are parasitic capacitors associated with the PMOS source follower transistor. These include capacitances due to gate source overlap, gate drain overlap, and gate to channel coupling. In addition there are two gate to source overlap capacitances and two parasitic n^+/p_{sub} diodes associated with the NMOS switches. Finally, there is a parasitic capacitance associated with the

74

Table 4.1: Summarized estimates of capacitances at integration and sample-and-hold nodes of single-ended and differential image sensors

Capacitance	Model	Estimate
Explicit poly-poly	$C_{poly}WL$	20.80 fF
Poly substrate	C_{poly_sub}	3.96 fF
NMOS n+ diffusion	$C_jWL + C_{jsw}(2W + 2L)$	3.20 fF
p^+/n_{well} bottom	$C_jWL(1 - \frac{V_{RB}}{PD_j})^{-M_j}$	272.4 fF
p^+/n_{well} side	$C_jWL(1 - \frac{V_{RB}}{PD_{jsw}})^{-M_{jsw}}$	16.8 fF
PMOS gate channel	$3/2 C_{ox}WL$	2.35 fF
PMOS gs/gd overlap	$C_{OL}W$	0.476 fF
NMOS gate channel	$1/2 C_{ox}WL$	1.75 fF
NMOS gs/gd overlap	$C_{OL}W$	0.615 fF

1000 μm^2 active area reversed biased p^+/n_{well} photodiode. Including parasitics, the integration node has an estimated capacitance of 297 fF.

Although the parasitic diodes and the explicit photodiode have associated parasitic resistance, the resistance of the NMOS switches is significantly smaller, and therefore provide the dominant resistive term. The circuit was simplified to its dominant and equivalent terms as shown in Figure 4.4, where R_s is the parasitic resistance of the NMOS switches, C_{S/H_EQ} is the equivalent capacitance at the sample and hold node, and C_{PD_EQ} is the equivalent capacitance at the integration node.

From this model the theoretical reset noise can be calculated following the procedure described by Nemirovsky *et al.* [96]. To calculate the noise it was assumed that once the reset and sample and hold switches have been turned off, the noise contribution is static for the duration of the integration cycle. Therefore, the reset noise is equivalent to the noise across the integration and the sample and hold node,
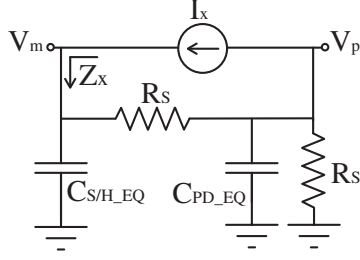
Figure 4.4: Simplified reset noise model of differential sensor

immediately prior to integration. To determine the noise across the nodes, the equivalent impedance is calculated as a function of frequency, and then integrated over the bandwidth of the circuit to obtain the total noise. Applying a test voltage source V_x between the integration and sample and hold nodes of the equivalent circuit, nodal analysis of the circuit in Figure 4.4 is used to solve for the equivalent impedance.

$$-jfC_{S/H\_EQ}V_m + \frac{V_p - V_m}{R_s} + I_x = 0 \qquad (4.1)$$

$$jfC_{PD\_EQ}V_p + \frac{V_p - V_m}{R_s} + \frac{V_p}{R} + I_x = 0 \qquad (4.2)$$

$$V_p - V_m - V_x = 0 \qquad (4.3)$$

Defining the input impedance as $Z_x(f)=V_x(f)/I_x(f)$, the power spectral density across the output nodes is:

$$S_{rst}(f) = 2KT\Re(Zx(f)) \qquad (4.4)$$

Integrating the power spectral density of the noise over all frequencies yields:

76

$$\int_{-\infty}^{\infty} S_{rst}(f)df = \frac{\alpha+1}{\alpha} \frac{KT}{C_{SH\_EQ}} \tag{4.5}$$

where $\alpha=C_{PD\_EQ}/C_{S/H\_EQ}$.

C_{PD_EQ} and C_{S/H_EQ} were estimated to be 297 fF and 36 fF, respectively, so in the differential sensor the total reset noise should be 360 μV, while the single ended sensor should have a reset noise of 117 μV.

4.3.2   Readout Noise

The readout noise of the sensor is due to the intrinsic physical noise sources of the MOSFETs in the source follower and readout buffer. The noise sources in the transistors include: 1) thermal noise due to the random thermal motion of the electrons in the channel and 2) flicker noise due to mobile carriers being trapped or released from interface traps at the silicon-oxide interface. These two noise sources are modeled by current sources across the drain source terminals as [96]

$$S_{I_d} = 4\gamma kT g_m + \frac{K_f I_d}{C_{ox}WLf} \tag{4.6}$$

where $\gamma = 2/3$ or $1/3$ depending on the region of operation, K_f is a process-dependent parameter and C_{ox}, W and L are the oxide capacitance per unit area and the geometric parameters of the MOSFET. Each noise source is then referred to the input node,
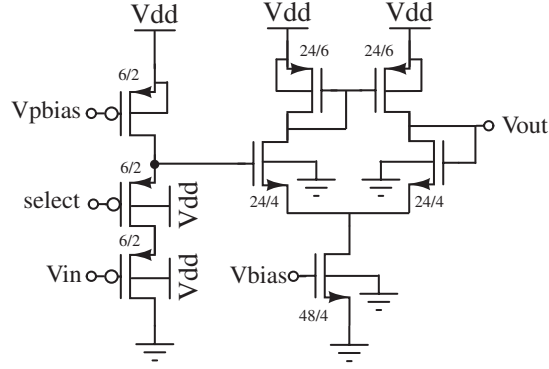
Figure 4.5: Schematic of readout circuit used for single-ended and differential sensor

summed and integrated over the bandwidth as

$$v_{n_{rdout}}^2 = \int_{-\infty}^{\infty} S_{v_{in}}(f)\, df \qquad (4.7)$$

A schematic for the readout chain is shown in Figure 4.5. The output noise of

the differential pair buffer was experimentally verified using a spectrum analyzer (Fig

4.6). This allowed us to extract the process dependent parameter K_f, which was also

used to determine the noise of the source follower.

The PMOS readout buffer introduces a significant body effect due to the 6V

supply ($V_{in}/V_{out} = 0.6$). The total input-referred readout noise of one readout path is

estimated to be 125 μV, that of the single-ended sensor. Therefore the readout noise

of the differential sensor will be 175.3 μV.

4.3.3   Experimental Results

The reset and readout noise were estimated as a function of optical power. A

similar test setup to that described in Chapter 3 Figure 3.8 was used. A grating

78
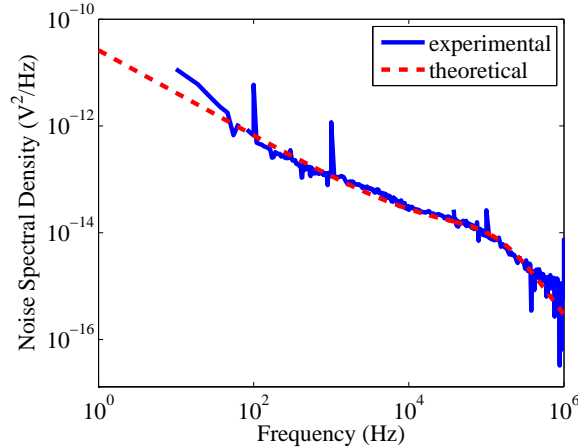
Figure 4.6: Measured output noise of the readout buffer

monochromator (Cornerstone 620, Newport Oriel Inc.) was used as a light source. A 20 nm slit assembly was used to obtain high optical power without sacrificing resolution at a center wavelength of 650 nm. The output light from the monochromator was directed into the integrating sphere through a fiber-optic coupler to minimize thermal coupling from the monochromator to the sensor. Illumination power was controlled by inserting neutral density filters between the output of the monochromator and the input port of the integrating sphere to obtain light intensities from $20 pW/mm^2$ to $50 nW/mm^2$. The chip was mounted to the output of the integrating sphere. The detector was reset for 1 ms with a 1 V clock pulse to minimize charge injection and clock feed-through. The integration time varied depending on optical power, which was measured with an optical power meter (Newport Inc. Model 1830-C) at the top port of the integrating sphere. The power supply Vdd is 6 V and is provided by a Duracell® lantern battery to allow noise characterization in the absence of power supply fluctuations. Care was taken to minimize interference and coupling from external sources. The total noise in the system is reported as the root mean square of

the noise with units of volts.

The definitive work which derives a method for measuring and estimating quantum efficiency, responsivity, and noise components was proposed by Fowler *et al.* [97]. The method for estimating reset and readout noise is summarized as follows. The total variance of the measured reset voltage is the sum of reset noise and readout noise variance. Using estimated readout noise and the measured reset noise, the true reset noise can be estimated.

$$Var[V(i)] = \sigma_{readout} + \sigma_{reset} \qquad (4.8)$$

The output voltage between two successive measurements is equal to:

$$V(i) = gQ_i + V_{noise}(i) - V_{noise}(S_1) \qquad (4.9)$$

where g is the front end gain of the sensor, Q_i is the accumulated charge due to photocurrent and dark current, and V_{noise} is the voltage due to total reset and readout noise at samples (S_1) and (i) respectively. By subtracting successive measurements, reset noise is eliminated.

Modeled as a stochastic process, the photocurrent and dark current are Poisson processes, while the readout and reset noise are assumed to be zero mean Gaussian processes. The mean and standard deviation between successive samples are as follows:

$$E[V(i)] = g_e q(\lambda_{ph} + \lambda_{dc})i\tau \qquad (4.10)$$

80

$$Var[V(i)] = g_e^2 q^2 (\lambda_{ph} + \lambda_{dc}) i\tau + 2\sigma_{readout}^2 \qquad (4.11)$$

where λ_{ph} is the photocurrent, λ_{dc} is the dark current, g is the sensor gain, i is the sample number, τ is the time interval between samples, and $\sigma_{readout}$ is the standard deviation of the readout noise.

Due to the nonlinear capacitance vs. voltage characteristic of the photodiode and other effects, short path segments from the overall integration path are selected that closely approximate linear regions. A linear least-square solution is then found that best fits readout noise and shot noise across the same segment in all sample paths under the same illumination conditions. This method, or variations on this method, is used extensively throughout this work.

Experimental estimates for reset and readout noise were obtained following the method described by Fowler *et al.* [97]. Figure 4.7 shows experimental input-referred reset noise. The average reset noise for the differential pixel is 333.5 μV, while the average reset noise for the single-ended pixel is 153.6 μV. These compare well with the theoretical predictions for reset noise of 360 μV and 117 μV, respectively. The discrepancies in these measured results are within the tolerances of fabrication mismatch.

Figure 4.8 shows the input-referred experimental results for the readout noise. In this case the differential sensor readout noise matches well with the theoretical calculations. The average differential readout noise from the trials is 169.0 μV, while the average experimental single-ended readout noise is 107.0 μV. This compares with
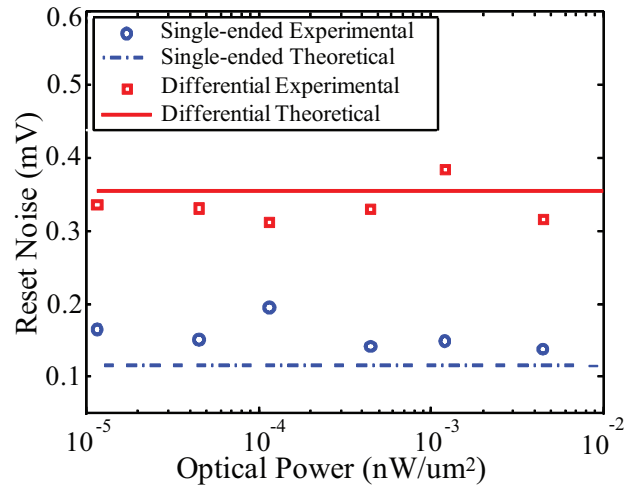
Figure 4.7: Measured reset noise of single-ended and differential image sensor
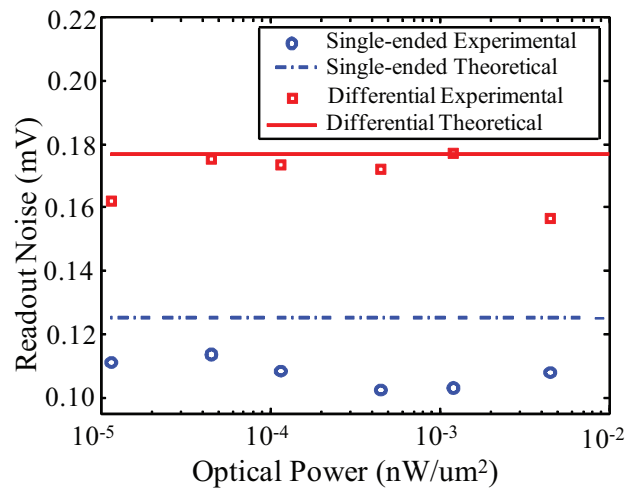
Figure 4.8: Measured readout noise of single-ended and differential image sensor

a theoretical readout noise of 175.3 μV and 125 μV respectively. Once again these are within the anticipated ranges of fabrication mismatch.

4.4   Suppression of Correlated Noise

Differential structures are well known for suppressing correlated noise. Although the differential sensor exhibits higher fundamental noise than a comparable single-ended sensor due to an increase in the number of components, its correlated noise suppression allow for better overall performance. An experiment was performed to the examine sensor performance in the presence of correlated noise. A bench-top BK Precision Model #1761 power source was used as supply voltage which is rated with a 1 mV ripple and noise between 5 Hz to 1MHz. The same experiments were performed as above but with a 5V Vdd with the BK Precision power supply. Again sensor measurements were taken over illumination intensities from 20pW/mm^2 to 50 nW/mm^2 and the noise decomposition algorithm described above was used to estimate the effective reset and readout noise. The resulting reset and readout noise as a function of illumination are shown in Figure 4.9. The differential sensor significantly suppresses the power supply noise as summarized in Table 4.2. The differential sensor was reduced the reset noise from 0.65 mV to 0.45 mV a 1.42X reduction, while the differential sensor reduced the readout noise from 1.15 mV to 0.125 mV a 9.2X reduction. Taking into account that the circuit has fundamental noise floor of 400 μV the differential circuit suppresses the power supply noise by 5X over the single-ended sensor.

(a)   (b)
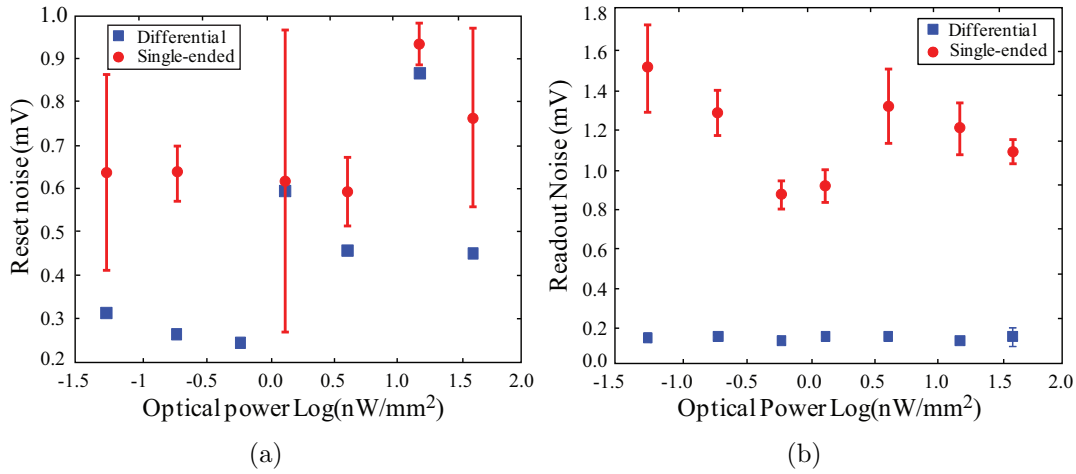
Figure 4.9: a)Measured reset noise of single-ended and differential image sensor with 1 mV power supply ripple. b)readout noise of single-ended and differential image sensor with 1 mV power supply ripple.

Table 4.2: Summary of Correlated Noise Suppression

Single	0.6472 mV	1.1514 mV
Differential	0.4556 mV	0.1252 mV
Reduction	1.42 X	9.20 X
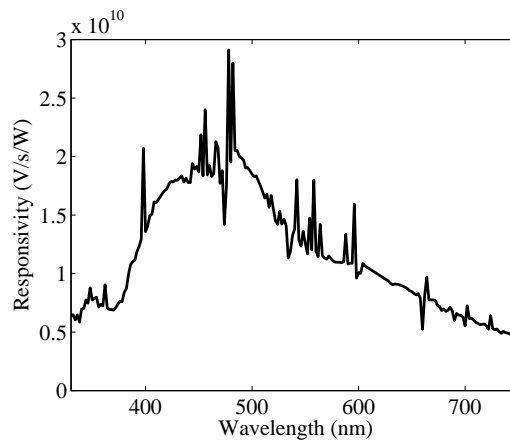
Figure 4.10: Experimentally derived responsivity of the differential active pixel sensor, showing highest responsivity for blue wavelengths.

The sensor was experimentally characterized for responsivity as a function of wavelength and linearity as a function of light intensity at several wavelengths. A monochromator (Newport Cornerstone 260 1/4M, model 74100) was used to select specific wavelengths with spectral resolution of 2 nm. The light intensity was varied using neutral density filters at the output of the monochromator, and an integrating sphere was used to obtain spatially homogeneous light. The light intensity was independently measured using a calibrated photometer (Newport 818-UV) fitted with a 5 mm diameter pinhole and an optical power meter (Newport 1830-C). Spectral responsivity is given by the amount of photo-current generated per incident photon at a particular wavelength and is principally determined by the wavelength-dependent absorption of light in silicon. As a consequence junctions at different depths exhibit different spectral responses [98]. The differential APS was experimentally verified to have the highest responsivity in the blue-green region of the electromagnetic spectrum Figure 4.10. The detector's measured noise and performance characteristics are summarized in Table 4.3. Note that the relatively low conversion gain results from the large area photodiode used in this experiment; this should improve for smaller diodes. The readout and reset noise were experimentally estimated by examining the statistics of many sample paths [99].

The performance of the differential pixel sensor is summarized in Table 4.3. The readout noise is 175.3 μV, reset noise is 360 μV, supply voltage 5V, power consumption 68μW, dynamic range 59 dB, maximum signal 3.5V, dark signal 4.1 mV/s, conversion gain 530 nV/e$^-$, and a detection limit of 2.2×10^8 photons/cm^3. The above design can be significantly improved by reducing reset noise, which is functionally achieved

Table 4.3: Summary of Differential Active Pixel Sensor Characteristics

Readout noise	175.3 μV
Reset noise	360 μV
Supply voltage	5 V
Power consumption	68 μW
Dynamic range	59 dB
Maximum signal	3.5 V
Dark signal	4.1 mV/s
Conversion gain	530 nV/e$^-$
Detection limit	2.2×10^8 photons/cm^2
Correlated Noise Suppression	5X

through increasing the in-pixel sample and hold capacitance.

4.5   Summary of Results and Critical Analysis

The noise performance of a differential sensor with in-pixel correlated double sampling has been examined. A theoretical noise model was developed and experimentally verified for the reset and readout noise components of the system. The results show that both reset and readout noise increase due to increased complexity within the circuit. However, in practical applications and measurement scenarios the benefits in correlated noise suppression are anticipated to outweigh the increase in fundamental noise [43].

One particular problem with the current design of this device is the leakage current at the sample and hold node. Because the sensor operates in hard reset, both the integration node and sample and hold node are set to zero volts during the reset phase. At the end of the reset phase, the isolation gate and reset transistor are turned off. Some electrons from the NMOS switches are pushed onto the sample and hold

node as well as integration node. While these charges are relatively inconsequential at the large capacitance integration node, they can be noticeable at the sample and hold node. These negative charges can push the voltage at the sample and hold node below zero volts. Parasitic p-n junctions from the sample and hold node to the substrate will become forward biased, causing more leakage than in the anticipated reversed bias case. This issue can be resolved by providing a separate reset voltage above ground, however, leakage at the sample-and-hold node cannot be eliminated entirely.

Active reset techniques can mitigate reset noise as well as fixed pattern noise (fabrication mismatch); however, because this sensor uses a hard reset technique, active reset techniques are difficult to apply. Fixed pattern noise can be mitigated through column or chip level CDS, but this somewhat defeats the purpose of in-pixel double sampling.

Chapter 5

Handheld Fluorometer

5.1   Introduction

Today fluorescence imaging is one of the most widely used methods in cellular biology. The popularity of fluorescence imaging is due to the specificity that can be achieved in detecting biochemical attributes. Thousands of natural and man-made fluorophores exist to detect and quantify a wide variety of analytes. Examples of these include the natural autofluorescence of NADH, which is a biproduct of cellular respiration, as well as the artificial fluorescence of FURA-2, a calcium indicator. Fluorescent markers are also a critical part of DNA analysis, biological agent detection, and can be used to discriminate different types of cells.

Fluorescent substances absorb light in one range of wavelengths and emit light in another longer range of wavelengths. The shift in wavelength is known as the Stokes shift and is illustrated in Figure 5.1. The shift in wavelength is due to the absorption and emission properties of the substance. Figure 5.1 is a generic Jablonski
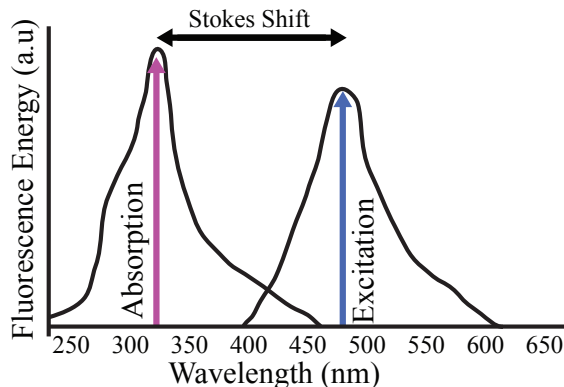
Figure 5.1: Illustration of stokes shift. Light absorption occurs at a lower wavelength (335 nm) and emission occurs at a higher wavelength (500 nm).

diagram representing the radiative and non-radiative paths. The Jablonksi diagram illustrates the state transitions required for fluorescence emission. Light is absorbed and the fluorophore is excited from its ground state S_0 to a higher energy state i.e. S_2. The excitation energy is often higher than the minimum required energy to enter state S_1. As a result, the fluorophore loses energy along non-radiative paths and intermediate states until it reaches state S_1. From S_1, one way to return to the ground state S_0 is to lose energy in the form of a photon. This emission photon is at a lower energy and therefore longer wavelength than the excitation photon.

While the transition from the S_0 state to a higher energy state due to the absorption of the photon is almost instantaneous, there is a delay between the absorption of the photon and emission of the excited photon. This delay is the lifetime of the fluorophore and represents the average time spent in the excited state. The fluorescence lifetime is an intrinsic parameter of the fluorophore and can be used as a detection parameter. This delay is usually on the order of 10 ns but can be much longer depending on the structure of the fluorophore.

S3 Excited
higher
S2 energy
states
S1

Energy

Absorbed
excitation
light

Emitted
fluorescence
light

S0 Ground State
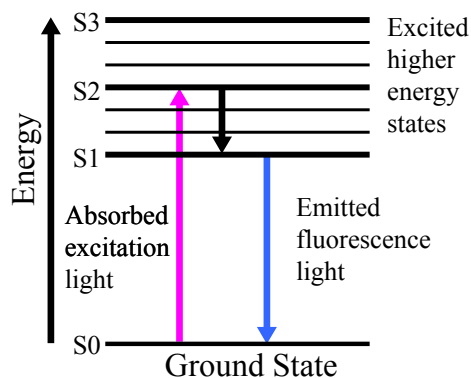
Figure 5.2: Generic Jablonski diagram depicting typical energy state transitions due to absorbed and emitted photons.

One difficulty with detecting fluorescence is that many fluorophores have a relatively low quantum yield. This means that the intensity of emission light is small in comparison to the excitation light. The Stokes shift allows most of the excitation signal to be filtered; however, the emission intensity is still small. While scientists are developing more specific probes with better quantum efficiency and lifetime properties, a method of signal transduction will always be required. Therefore, low-noise high-sensitivity detectors will continue to be an important aspect of any fluorescence detection system.

This chapter discusses a customizable hand-held fluorometry platform capable of performing on-line measurements [100]. The platform uses the CMOS detector described in Chapter 4 and polymer filters cast directly onto the detector surface. While the reported system uses a single CMOS detector, the system can easily be expanded into a 2-D array allowing spatial resolution. In addition, CMOS technology enables application-specific sensor designs; this platform can also incorporate other electronic sensors. The design strategy taken to develop this system is to use

custom sensors designed in commercially available CMOS technologies coupled with multiple polymer-based optical filters and commercially available excitation sources integrated onto a single platform with computer-based control. Many groups have been pursuing micro-fluorometry, and their work can be broken into three distinct areas: optical excitation sources, excitation filters, and detectors. Common excitation sources include standard bench-top spectrophotometers, vertical cavity surface emitting lasers (VCELs), organic light emitting diodes (OLEDs), or photodiodes [101–107]. The main challenges facing these excitation methods are complex fabrication processes or lack of integration. To filter the excitation source an excitation filter is used. Typically optical filtering technologies include absorption and interference based filters. Common optical filtering technologies used in micro-scale fluorometry include absorption and interference based filters. [108–112]. For a complete review of optical filtering technologies see Dandin *et al.* [113]. While filterless fluorescence detection is possible, it requires the exploitation of the fluorescence lifetime, or other temporal techniques which do not work well with all fluorophores. The handheld system reported in this chapter uses a custom CMOS sensor fabricated in a commercially available process with an absorption-based optical filter requiring only one deposition step. This system enables a rapid-prototyping platform for fluorescence measurements covering a wide spectral range. This chapter discusses the design and fabrication of the platform, several configurations and a series of bioassays utilizing different filters and fluorophores.

5.2 Handheld Fluorometer

There are four major components to any fluorometry system, a sample holder to contain the fluorophore, an excitation light source to excite the fluorophore, an excitation filter to block the excitation light source, and a detector to measure the fluorescence emission light. A representative diagram of a fluorescence detection system is shown Figure 5.3(a) . The specific implementation of the fluorometer is shown in Figure 5.3(b) with a UV LED, DIP 40 package with custom CMOS detector, polymer optical filter, a standard microscope cuvette and light-tight package with DAQ. The DAQ controls the LED and CMOS detector via a custom PCB board. The specific details of each component are described below.
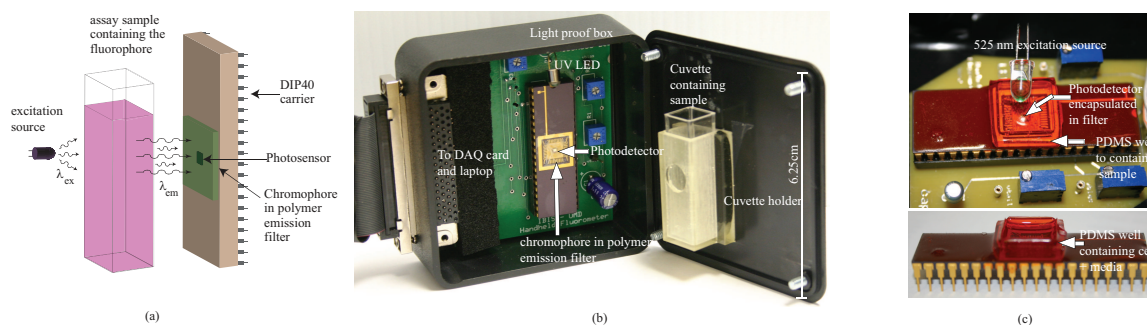
Figure 5.3: (a) Handheld fluorometer components; (b) Photograph of handheld fluorometer for use with a standard cuvette and 400 nm long pass filter; (c) Top and side view of handheld fluorometer for use with custom sample well and 540 nm long pass filter. [1]

5.2.1 Sample Holder

Samples in fluorescence assays are typically liquid volumes and therefore require a container to hold the specific sample volume. Commercially available fluorescent measurement systems use methacrylate cuvettes. For the first generation hand-held

fluorometer a standard cuvette was incorporated into the system design. The commercially available cuvettes measure 1 cm X 1 cm x 4 cm in dimension and can hold up to 3.5 mL of sample. The dimension of the CMOS chip is 1.5 mm X 1.5 mm, and the dimensions of the sensor are even smaller. While this sample volume is clearly larger than necessary it represents a convenient first step to integrated fluorescence. Subsequent experiments used a custom well fabricated directly onto the chip, increasing the coupling efficiency of the sample, decreasing the necessary sample volume and integrating a polymer filter directly into the well material. Figure 5.3(c) shows the integrated sample holder/filter.

5.2.2 Excitation Source

Fluorescence systems require an excitation source to generate the excitation light necessary to stimulate the fluorophore. In a bench-top setting, the excitation light is produced by a broadband source, and filtered using a combination of prisms, mirrors and grating filters to produce a narrow-band source. At the microscale other methods are required. In this work a narrow-band excitation source was chosen in the form of discrete 375 nm (Nichia) and 525 nm (Lumex) LEDs were used depending on the experiment.

5.2.3 Optical Detector

The low quantum efficiency of the fluorophore dictates that the optical detector must have superior noise performance. Although photomultiplier tubes (PMTs)

and charge couple devices (CCDs) have better noise performance than CMOS devices, they are more expensive and more difficult to integrate than CMOS devices. Although the fundamental noise floor of the detector sets the minimum observable signal, portable devices often suffer from additional environmental noise such as power supply ripple or electromagnetically coupled interference, which can set the practical noise floor. As a result of these additional noise sources the differential pixel sensor from Chapter 4 was chosen as a detector due to its ability to suppress correlated noise.

5.2.4   Optical Emission Filter

Typically all fluorescence systems require an excitation filter to block the excitation light which is often orders of magnitude larger than the emitted fluorescence signal due to a fluorophores low quantum yield. These filters are generally either interference filters or absorption filters. In this work absorption filters were used because they require fewer processing steps, are easier to fabricate, and are more robust against fabrication tolerances than interference filters [114]. Two polymer filters were fabricated, both by mixing the appropriate chromaphore into poly-dimethyl-siloxane (PDMS). The rejection spectrum of the filter is determined by the type of polymer, while the magnitude of rejection is dictated by both the thickness of the polymer filter and concentration of chromaphore embedded in the polymer filter. Benzotriazole (BTA, Great Lakes Chemical Inc.) was embedded in PDMS and able to achieve a 60 dB rejection for a 400 nm wavelength excitation source, corresponding to the excita-

94
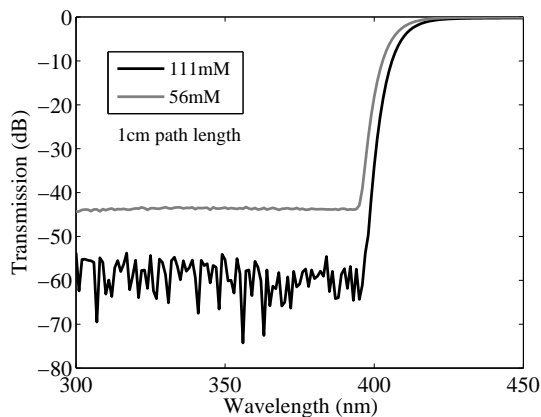
Figure 5.4: Transmission characteristics of 2-(2'-hydroxy 5'-methylphenyl) benzotri-azole in Toluene [1].
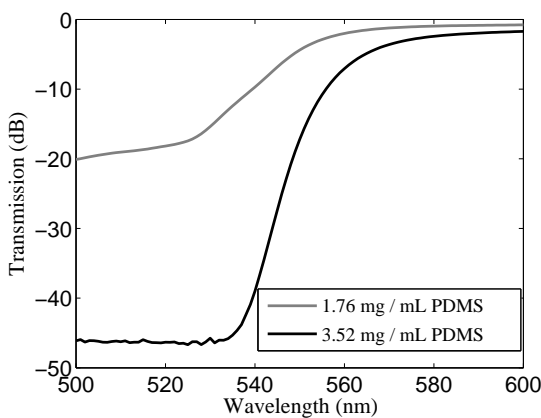
Figure 5.5: Transmission characteristics of Sudan II embedded in PDMS on a glass slide [1].

tion wavelength of common fluorophores such as NADH. The full spectral absorption characteristics of the BTA filter are shown in Figure 5.4. Additionally, Sudan II was embedded into a PDMS filter and shown to achieve a 45 dB rejection at 540nm wavelength, the wavelength used with alamarBlue, a live/dead cell stain. The full spectral absorption characteristics of the Sudan II filter are shown in Figure 5.5. A comparison of other handheld devices is provided in Table 5.1.

Table 5.1: Comparison of this work's handheld device with commercially available handheld fluorometers and research LOC systems [1].

Characteristic	This Work	Shepard et al. [115]	El Gamal et al. [41]	USB4000-FL [116]	Pico*fluor* [117]	Fluorpen [118]
Application	Lab-on-chip/handheld fluorometer	Time resolved fluorescence	Bioluminescence	Handheld fluorometer	Handheld fluorometer	Handheld fluorometer
Detector	p^+/nwell photodiode	nwell/psub photodiode	p^+/n/psub photodiode	linear CCD array (TCD1304AP Toshiba)	Photodiode	PIN Photodiode
Technology	0.5 μm standard CMOS	0.25 μm standard CMOS	0.18 μm CIS process	Not reported	Not reported	Not reported
Power consumption	68μW, 5V	Not reported	26 mW	250 mA (5 V)	Not reported (6V)	Not reported (6V)
Dark noise	4.1 mV/s	10.4 μA/s	2.6 mV/s	50 RMS counts	Not reported	Not reported
Excitation source	375/525 nm LED	Laser diode	None required	470/395 nm LED	365/460/525 nm LEDs	LED
Dynamic Range	59 dB	74 dB	61 dB	49 dB	40 dB	Not reported
Sensitivity	10 μM β-NADH,	Not reported	1.3 fmol ATP	Not reported	1ng/mL ds-DNA with PicoGreen	Not reported
Further processing/noise reduction	No	$\checkmark$	$\checkmark$	$\checkmark$	$\checkmark$	$\checkmark$

5.3 Bioassays

Using the system described above several bioassays were performed including: a cytotoxicity assay and two metabolic assays. Cytotoxicity assays are used to determine the biocompatibility of particular materials. The viability of cells is periodically assessed after a particular material is introduced to the environment, thereby providing an integrated solution for developing novel biomaterials. Metabolic assays offer the potential to observe the metabolic state of a biological cell. These assays are useful for many applications from directly measuring properties about the cells or indirectly measuring the cellular response to an environment serving as a foundation for cell based sensors. The cytotoxcitiy assay and the first metabolic assay use a 375 nm LED with a BTA based filter as shown in Figure 5.3(b), while the second

metabolic assay uses a 525 nm LED with Sudan II based filter as shown in Figure 5.3(c).

5.3.1 Cytotoxicity Assay

Nanoparticles are a relatively new technology in which nano-sized particles are manufactured to have specific properties. These particles may be magnetic, exhibit fluorescence or function as drug carriers. When used as drug carriers for biological purposes, it is important that the nanoparticles are non-toxic to the host, therefore the scientific community developing these nanoparticles must fully characterize the cytotoxicity. Poly(amidoamine) (PAMAM) dendrimers are a family of highly uniform macromolecules that exhibit significant branching. These dendrimers have potential uses in oral drug delivery, but the mass, shape, size and surface chemistry affect the transportation across the epithelium in the gut [119, 120]. The handheld fluorometer is shown to aid the analysis of two PAMAM dendrimers and provide a foundation for massively parallel cytotoxicity studies. Based on the optical filtering properties of our first generation fluorometer, the AQUA live/dead stain assay (Invitrogen) was chosen. The AQUA live/dead stain binds with amines intensifying the fluorescence. With live cells the stain can only interact with amines on the surface, while in dead cells, the stain permeates the cell and interacts with amines on the exterior and interior. Therefore dead cells exhibit a higher fluorescent signal than live cells. The AQUA live/dead stain has peek excitation at 375 nm and peak emission at 526 nm matching well with the handheld detector.
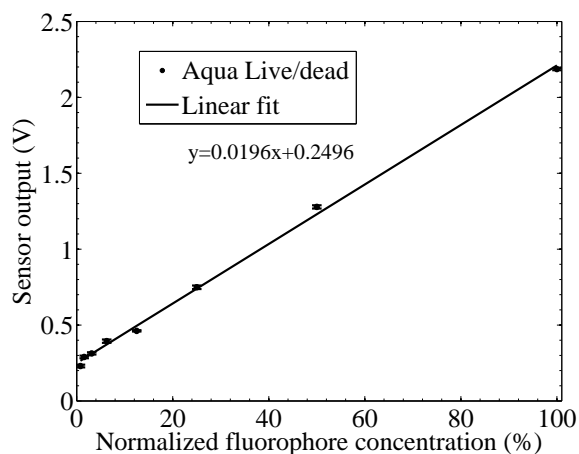
Figure 5.6: Sensor output is a linear function AQUA live/dead stain. Note that the error bars are extremely small [1].

An AQUA stain calibration curve was determined using the handheld sensor. The stain was dissolved in HBSS-BSA starting with the recommended dosage (100%) and serially diluted. Five samples at each concentration were measured with the resulting calibration curve with error bars is shown in Figure 5.6. The calibration curve is highly linear and exhibits a low detection limit was found to be less than 12% of the recommended dosage.

Human intestinal adenocarcinoma cells (Caco-2 cell line, ATCC) cells were exposed to two types of PAMAM dendrimers: G3.5 and G4 (Sigma-Aldrich), and monitored with the handheld fluorometer. The G4 family is known to be toxic, while the G3.5 family is known to be non-toxic [119, 120]. The Caco-2 cells were cultured using a standard cell culture procedures in a T-75 flask at 37^oC, 5% CO_2 in a humidified incubator. After the cells reached 95% confluence, they were harvested to form a cell suspension of 500 cells/μL.

The experiment consisted of seven 2ml test samples: one control sample free of dendimers, three G3.5 samples and three G4 samples. The G3.5 and G4 samples
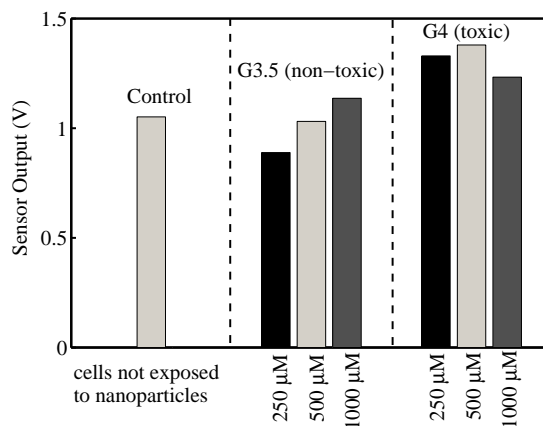
Figure 5.7: Sensor output for cells exposed to the PAMAM dendrimers [1].

each had a dendrimer dosages of 250, 500 and 1000 μM. Each of the test samples were incubated at 37ºC, 5% CO_2 for 75 minutes, after which 5 μL of the stain was dissolved in dimethyl sulfoxide (DMSO) and added to the cell suspension. The test samples were then incubated in ice for 30 minutes. Each sample was centrifuged and washed with a 1% HBSS-BSA (bovine serum albumin) and re-suspended in HBSS-BA solution. The samples were placed in the hand-held detector. Fluorescence measurements are shown in Figures 5.7 with the computed viability shown in 5.8. The results indicate that the G4 dendrimer sample exhibits consistently higher fluorescence than the G3.5 dendrimer samples confirming that the G3.5 cells had been compromised. Unfortunately, the fluorometer was unable to determine the different dosages of dendrimers in the toxic case. More samples must be examined to average out variability in cell density but were not included in this study due to limitations in sample volume and reagents. Despite the variations, the hand-held results match well with previously determined measurements taken with traditional cell viability assays reported by Jevprasesphant *et al.* [120]).
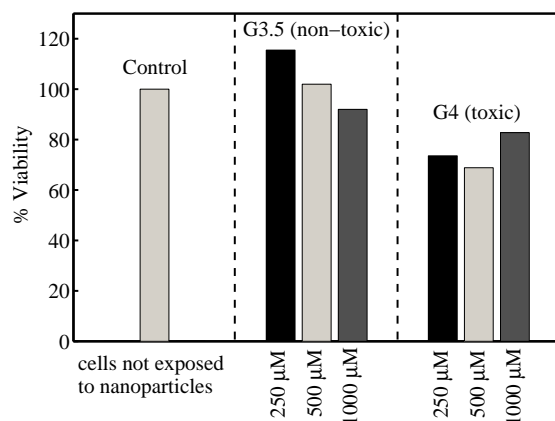
Figure 5.8: Viability of cells exposed to the PAMAM dendrimers [1].

5.3.2 Metabolic Activity Assay I (NADH)

The cytotoxicity assay is inherently an end-point assay, since all measurements occur after the experiment has been completed. While this is useful for some applications, for many applications it is desirable to perform on-line measurements, *i.e.*, measurements taken during the course of the experiment. These on-line measurements allow the collection of greater experimental statistics and in some cases reuse of materials. The hand-held fluorometer design in this chapter is capable of obtaining sequential measurements over a long period of time enabling on-line data collection over the course of minutes, hours or even days depending upon the experiment. One example of a useful metabolic experiment that requires on-line fluorometry system is the measurement of nicotinamide adenine dinucleotide (NADH), an auto-fluorescent fluorophore that is a byproduct of cellular respiration. In yeast cells NADH in reduced form or NADH in oxidized form is produced depending on the cellular pathways described in Figure 5.9. Although yeast cells are not necessarily harmful, in this work they serve as a surrogate for any potentially harmful pathogen. Real-time measure-
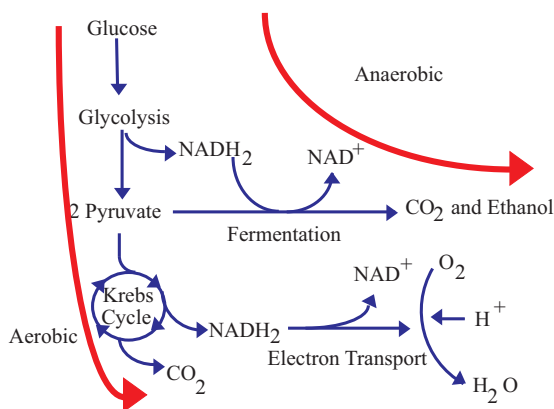
Figure 5.9: Metabolic pathways for glucose in yeast cells. NADH is repeatedly recycled and its concentration depends on the type of respiration occurring [1].

ments of NADH may therefore be useful in detecting the presence of a pathogen in a water supply. The peak excitation wavelength of NADH is 380 nm and the peak emission wavelength is 460 nm. For these metabolic experiments the test setup in Figure 5.3(b) with a 375 nm excitation LED and a BTA polymer filter is used.

NADH Calibration Curve

To determine the level of NADH present in a solution, the system must be characterized against a known NADH level. This calibration curve was obtained using β-NADH (Sigma-Aldrich) in 1X TRIS-EDTA solution of pH 8 that was successively diluted from 11.012 mM to 0.672 μM. The resulting handheld fluorometer calibration curve, taken with a sensor integration time of one second, was compared against a standard spectrophotometer calibration curve in Figure 5.10. The results of each calibration curve were normalized against a peak signal intensity, indicating that the handheld fluorometer can successfully detect NADH concentrations over several orders of magnitude, but it is not quite as sensitive as a standard bench-top sys-
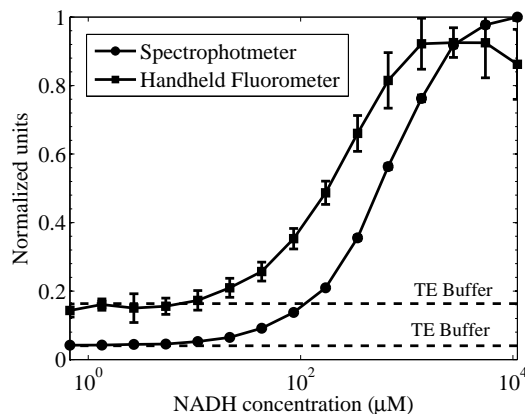
Figure 5.10: Sensor output as a function of β-NADH concentration. Units are normalized to allow comparison with results from standard spectrophotometer, where normalized units = sensor output/max output [1].

tem which uses optics and a photomultiplier tube.(SpectraMax® M2/M2e microplate reader, Molecular Devices). The detection limit of the handheld fluorometer was determined to be 10 μM and the NADH experience self quenching at concentrations above 1000 μM

NADH On-line Assay

The production of NADH in yeast cells is directly related to the metabolic activity of the cells. The metabolic activity of the cells is affected by several factors; however, the primary confederations in this experiment are the concentration of glucose available, the amount of oxygen in the media, and the PH of the media. Yeast cells (Baker's yeast, 1 g/20 mL media) were cultured in yeast peptone dextrose (YPD) over a two day period at 37°C. The cells were then washed in sterile water and re-suspended with a serial dilution in media. Because it is difficult to count the number of cells visually, instead the cell concentration is reported using optical den-
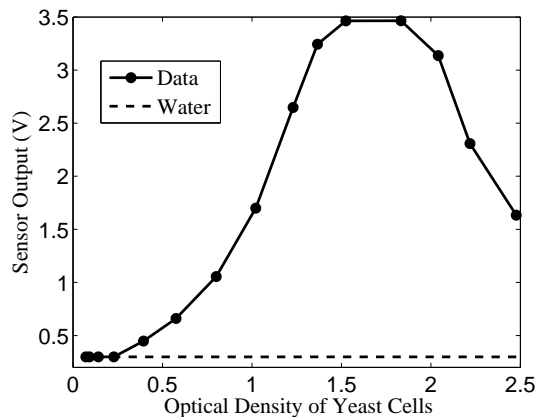
Figure 5.11: Sensor output as a function of optical density of yeast cells [1].

sity (OD). Optical density is a common method for reporting the concentration of cells, and measured using a standard spectrophotometer at 600 nm wavelength. The initial response of the cells measure with the fluorometer, using a 1 second integration time, are shown in Figure 5.11, where at high concentrations the cells experience self-quenching, and the excitation light cannot penetrate to the cells directly above the detector. The sensor experiences a linear response for optical densities below 1.2 indicating that all future experiments should use cell densities below this OD.

As indicated above, the production of NADH depends on both the amount of glucose and oxygen in the system, which affects whether the yeast are respiring aerobically or anaerobically. Depending on the dynamics of the NADH measurements, the metabolic state of the cells can be inferred. Initially, media with germinating yeast spores should start with a low NADH concentration. As the amount of available oxygen decreases, electron transport in the metabolic cycle stops, causing an increase in NADH. Eventually the cells switch from aerobic an anaerobic respiration causing the measured fluorescence response to decrease as the NADH is converted to NAD
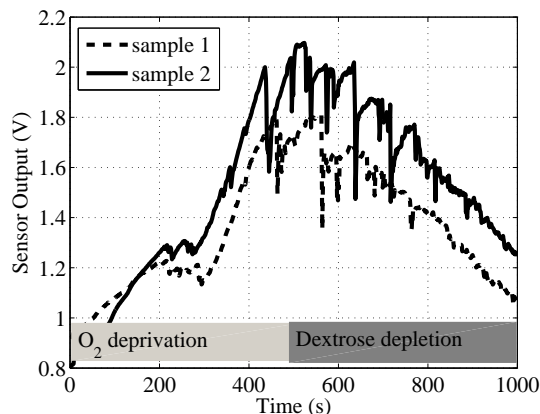
Figure 5.12: Sensor output versus time as yeast cells germinate in dextrose solution, reflecting the change in fluorescence due to changing NADH levels [1].

[121, 122]. While the level of oxygen dictates the kind of respiration, the level of glucose influences the rate of respiration and therefore the rate of NADH production. Dry yeast, 0.3g, was placed in 3 mL of 1 g/mL warm dextrose solution to increase metabolic activity. The sensor output was recorded in one second intervals over 17 minutes. The resulting fluorescence curve shown in Figure 5.12 shows a rise induced by oxygen present in the solution, followed by a fall initiated by the change from aerobic to anaerobic respiration. Because NADH is a small molecule and able to pass through the membrane, it is impossible to tell whether the NADH is intra-cellular or extra-cellular without separating the cells from the media.

5.3.3 Metabolic Activity Assay II (alamarBlue®)

To assess the handheld fluorometer for use as an alamarBlue® assay, Bovine Aortic Smooth Muscle Cells (BAOSMC, Cell Applications, Inc) were plated into the custom sample holder with integrated Sudan II filter as shown in Figure 5.3 (c). This well serves as both a storage mechanism for the cells, which is closely coupled to the

sensor surface, increasing collection efficiency, as well as an optical filter to suppress fluorescence excitation light. A combination of growth media (Cell Applications) and alamarBlue® indicator was added to the well with a 1:10 ratio. The entire device was place in a water-proof box and placed inside a cell incubator set 37^oC and 5% CO_2. This experiment demonstrates an immediate advantage over bench-top techniques, which are unable to fit in an incubator. The sample was monitored over a 10 hour period taking fluorescence readings every 10 minutes, due to the slow time dynamics of cellular processes. The alamarBlue® indicator changes from a non-fluorescent species to a fluorescent species in the presence of metabolic activity. Another advantage of this assay system is that the measurements are taken periodically and do not disrupt the cells in any way. An LED with 525 nm (Lumex Corp.) peak wavelength was used to excite the alamarBlue® which has a peak excitation of 530-560 nm, and a Sudan II filter with 45dB rejection at 525nm was used to filter the excitation light. The results over the 10 hr experiment are shown in Figure 5.13. There is a clear rise throughout the entire experiment indicating that the cells experienced metabolic activity. Towards the end of the experiment the rise drops off indicating that either the cells were no longer viable, or more likely, all of the alamarBlue® had been reduced. To assess the viability of cells longer than 10 hours, the alamarBlue® must be replaced. At the end of this experiment the viable BAOSMC cells were observed visually under a microscope. Indicating that the reduction of the alamarBlue® was due to viable cells.
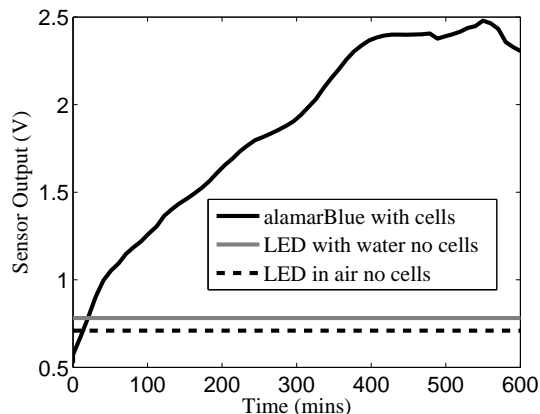
Figure 5.13: Sensor output versus time for BAOSMC cells in media and alamarBlue solution, reflecting the reduction of the dye by the cells to a fluorescent form [1].

5.4   Summary of Results and Critical Analysis

A handheld fluorometer was designed, fabricated and tested with a variety of fluorescence assays. The fluorometer consists of a commercially available LED as an excitation source, a custom CMOS differential image sensor, two custom polymer filters, a commercially available cuvette as well as a custom sample holder depending upon the application. The sensor displays readout noise of 175.3 μV, reset noise of 360 μV, dynamic range of 59 dB and conversion gain of 530 nV/e$^-$ while the two filters, BTA and Sudan II in polymer matrices, pass wavelengths longer than 400 nm and 540 nm, respectively.

The fluorometer was used to detect the AQUA live/dead stain, NADH with detection limit 10 μM. and alamarBlue, three common fluorescent assays. Additionally, the sensor demonstrated detection of an endpoint live/dead assay, an on-line autofluorescent metabolic assay, and an on-line live-dead metabolic assay. Although only three assays were performed in this work, it is clear the system can be configured

for additional functionality.

The key advantages of this system over bench-top system and other microfluo-rometric systems is that this system is easily configurable. It can incorporate a wide variety of commercially available LED excitation sources and a one-step polymer filter deposition process for rapid prototyping. Additionally the size of the device allows it to provide real-time measurements in a cell incubator, without the need for disturbing the cells for the entire 10 hour experiment.

Although the current system is mesoscale, each device is completely scalable in size presenting a direct path for microscale integration. Future development of this system will focus on system scale-down including the integration of a data acquisition and control system removing the need for a tethered data acquisition system, increasing the number of sensors in the device including capacitive, electric field, and impedance sensors, incorporating a microfluidic sample preparation system which can load samples into a microvial for analysis. Additionally, an array of optical detectors will be fabricated to allow spatial resolution for either parallel sample analysis or other spatially dependent fluorescence.

Chapter 6

CTIA Bioluminescence

6.1 Introduction

Biological agent detection is an increasingly important challenge. New tools, techniques and detection systems must be developed in order to meet this challenge. Ideally these detection systems should be sensitive, rugged, portable, reconfigurable, and distributed.

One promising technology uses CANARY cells at its core. CANARY cells are genetically engineered human B-cells, that have been modified to be sensitive to particular biological agents leveraging the specificity of the human immune system. B-cells have receptors sensitive to a unique antigen, thus providing the superior specificity. In addition to being sensitive to a unique predetermined antigen, the cells have also been modified to include a sequence of DNA that expresses a green fluorescent protein, aequorin, that emits photons when the B-cells experience a binding event as depicted in Figure 6.1.

The specific sequence is as follows: 1. B cells are exposed to the bioagent. 2. The antigens cross-link with the antibodies at two or more locations on the cell surface. 3. A biochemical signal transduction cascade is triggered resulting in calcium release 4. The calcium release causes aequorin to emit photons. 5. The photons are detected by an external measurement system.
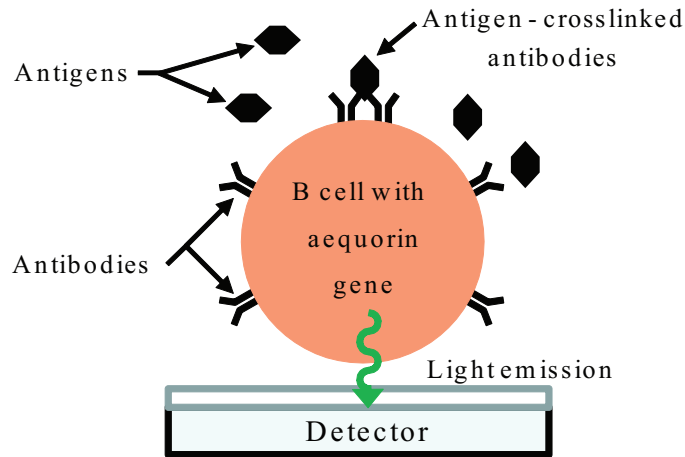
Figure 6.1: CANARY Cell functional diagram [5]

In bench-top systems, these CANARY cells have been shown to successfully detect specific antigens within 10 minutes. One such bench-top system, BioFlash, has been developed by Innovative Biosensors, Inc [6]. This system has been shown to detect up to 21 different biological agents within minutes.

While these systems work well, they are bench-top systems, relying on relatively large mechanical multiplexing, sample preparation, and photo-multiplier tubes (PMT) as a detection element. Although bench-top devices are sufficient for many applications including detection and monitoring of biological agents in government building, it is desirable to scale the cost and form factor of these sensors to a hand-held size for ubiquitous deployment.
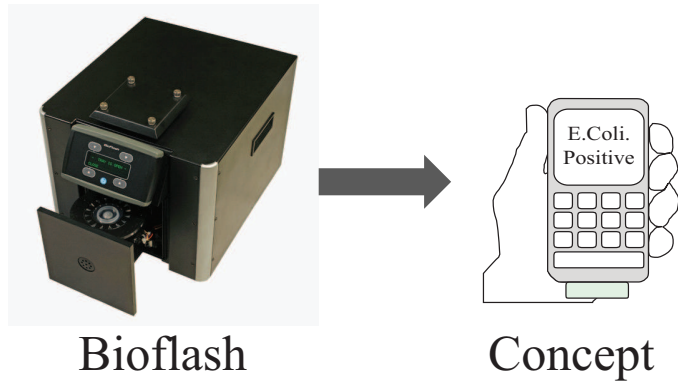
Bioflash   Concept

Figure 6.2: Conceptual diagram showing scale-down of Bioflash to handheld device [6].

A PMT can be considered hand-held in size; however, it is a single detector element and therefore requires other mechanisms to achieve sample multiplexing. Pathogen sample preparation, multiplexing, and interaction are achieved through mechanical elements which are large and do not easily scale to hand-held size. Microfluidics offer an alternative to some mechanical components. Microfluidic systems have demonstrated separation and purification of cell sized particles and other biomolecules through: electrophoresis, dielectrophoresis, and electro-osmotic flow [123–127]. Sample-CANARY cell interaction can also be facilitated through microfluidics by either forcing an interaction with osmotic pressure, or through the use of magnetic nano-particles in a magnetic field. Diffusion and facilitated interaction by osmotic pressure are difficult for creating the necessary physical interaction between sample and B cells. Under low pressure little interaction between the sample and cells is achieved, but under moderate pressure the cells tend to deform and slip out of the microchamber, and at high pressure the cells tear. Magnetic nano-particles offer an attractive alternative for facilitating an interaction between the pathogen and B

cells, in which magnetic beads are loaded into the B cells and an external magnetic field is used to mix the sample and B cells together.

Of the many devices for low-light detection, photo-multiplier tubes, charge-coupled devices, photo-avalanche devices, and active pixel sensors are the most common elements. Photo-multiplier tubes (PMTs) are the gold standard for low-light imaging. They provide robust, low-noise, event driven detection of single photons. While PMTs have superior noise performance compared to other devices, they are not without their drawbacks. The primary drawbacks of these systems include price, magnetic sensitivity, and fragility. Additionally, spatial resolution must be achieved through secondary devices or optics, since PMTs have one large detector.

Charge-coupled devices (CCDs) are more rugged than PMTs, less expensive, relatively insensitive to magnetic fields, and have spatial resolution, generally at the expense of thermal noise, frame-based scanning and speed. While they have more noise than PMTs, they still offer excellent performance. Although CCDs are fabricated in silicon, generally CMOS electronics cannot be fabricated on the same device. Avalanche-photon detectors (APDs) can be fabricated in standard CMOS technologies as well as more exotic materials such as silicon carbide. Silicon versions of these devices generally have more noise than their CCD counterparts, but can provide high front-end gain, high quantum efficiency and fast timing resolution. High front-end gain is an important feature which minimizes the effects of down-stream noise along the readout path. These devices can be fabricated in arrays, but they require specific multiplexing techniques and aggressive bandwidth considerations.

Active pixel sensors (APSs) use a reverse-biased p-n junction to collect photo-

generated electrons. Active pixel sensors can be fabricated in standard CMOS processes which can incorporate signal processing on-chip and generally have better noise performance than their APD counterparts, but this comes at the expense of lower quantum efficiency and lower front-end gain. For these reasons, active pixel sensors represent the majority of commercially available imaging systems.

As mentioned before, PMTs are the gold standard for sensitive detectors for fluorescence and bioluminescence applications. For example, the Hamamatsu H7155 PMT has a quantum efficiency of 11% at 500nm, a noise count of 50 counts/sec, and an active area of 8 mm^2. Assuming photons and dark current follow a Poisson distribution, the standard deviation of the signals is proportional to their mean the signal-to-noise ratio is defined as:mamatsu H7155 PMT has a quantum efficiency of 11% at 500nm, a noise count of 50 counts/sec, and an active area of 8 mm^2. Assuming photons and dark current follow a Poisson distribution, the standard deviation of the signals is proportional to their mean the signal-to-noise ratio is defined as:

$$SNR = \frac{P_{signal}}{P_{noise}} = \frac{(\eta q \lambda_{ph})^2}{Noise + \eta^2 q^2 \lambda_{ph}} \tag{6.1}$$

where, P$_{signal}$ is the power of the signal, P$_{noise}$ is the power of the noise and η is the quantum efficiency, q is the electron charge, and λ_{ph} is the photon arrival rate. Intensity is the mean signal amplitude, and Noise is the mean noise amplitude. Defining the NEP as the number of photons required to obtain an SNR of 1.

$$NEP = (\eta q \lambda_{ph})^2 - \eta^2 q^2 \lambda_{ph} - Noise = 0 \tag{6.2}$$

For this device, we need 68 photons/sec to obtain an SNR of 1.

Given the active area of the device the noise floor is incredibly low. While CMOS technology cannot achieve this number, there is no need for such a detector as large as the PMT, and in fact, the size of the detector is often a burden to the system, since it prevents multiple simultaneous assays. Representative detectors from various technologies were compared with respect to area, dark current per area, dark count per area, quantum efficiency, and a scaled dark current. For commercially available devices, the dark current was calculated for the device size, while for research devices the dark current was calculated for a device with diameter 250 μm. These results are tabulated in Table 6.1 Clearly the PMT devices have superior noise performance over all other technologies, but are larger than necessary. CCDs, Photodiode, APSs, SPADs and APDs are all much closer in performance.

The same statistics were used to determine the number of photons required to obtain an SNR of 1 shown in Table 6.2. Again, for commercially available devices, the number of required photons to achieve an SNR of 1 was calculated. For research devices each device was scaled to a diameter 250 μm and then the required number of photons to achieve an SNR of 1 was calculated. For event-based detectors the photon-detection efficiency is equivalent to the quantum efficiency of a standard detector.

Data in Table 6.2 shows that it is clear that CMOS image sensors present a viable option for achieving biological agent detection multiplexing while facilitating a sample/B cell interaction though the use of magnetic nano-particles. Active pixel sensors and specifically, integration based active pixel sensors, suffer from several noise sources, which include: reset noise, readout noise, environmental noise and thermally

113

Table 6.1: Detector Metrics for Research and Commercially Available Devices

Part A: Photo-detectors						
Type	Part	Area (mm^2)	Dark Current (pA/cm^2)	Dark Count	Quantum Efficiency (470 nm)	Dark Current (pA)
CCD	Kodak KAC-00401 [128]	25.40	900.00	N/A	60%	0.4416
CCD	Kodak KAI-0330 [129]	28.04	500.00	N/A	36%	0.2453
Photodiode	Perkin Elmer VTB1013 [130]	1.6	1,250.00	N/A	23%	0.6133
APS	Bolton et. al (2002) [34]	1.4	4.29	N/A	55%	0.0021
APS	Eltoukhy (2006) [41]	0.050	1,000.00	N/A	40%	0.4906
APS	Sander	0.049	169.58	N/A	40%	0.0832

Part B: Photon-counting Devices						
Type	Part	Area (mm^2)	Dark Current (pA/cm^2)	Dark Count	PDE (470 nm)	Dark Current (pA)
PMT	Perkin Elmer C982 [131]	19.63	2.45E-03	3	15%	0.0005
PMT	Hamamatsu H7826 [132]	50.24	6.37E-02	200	15%	0.0320
SPAD	Gulinatti (2005) [133]	7.85E-03	1.22E+04	6,000	35%	6.0000
SPAD	Daniel (2008) [134]	1	4.32E+03	220	26%	17.280
SPAD	IBIS	6.36E-03	4.03E+04	16,000	60%	19.7530
APD	Hamamatsu MPPC-100 [135]	1	4.80E+03	300,000	73%	48.0000
APD	Hamamatsu MPPC-100 [135]	1	9.60E+01	6,000	1%	0.96000

generated dark current. Reset noise is the uncertainty in the number of charges left on the integration capacitance after resetting the device. Methods for removing this noise include correlated double sampling, multiple-non-destructive sampling, and active-reset. Fixed pattern noise can be removed with double delta sampling as well as active-reset methods. Environmental noise usually comes from the effects of external electromagnetic fields or on-chip coupling. Proper shielding as well as differential techniques can mitigate some of these environmental noise effects. Finally, thermally generated dark current accounts for one of the most influential noise sources and is due to the thermal generation of carriers in the p-n junction at the front end of the detector.

Thermally generated carriers, or dark current, cause noise at the front end of the detector and are therefore amplified by any subsequent gain through the system. In addition, this noise cannot be removed by any of the aforementioned techniques.

Table 6.2: Required Photons for Research and Commercially Available Devices

Part A: Photo-detectors					
Type	Part	Quantum Efficiency (470 nm)	Dark Current (pA)	# charges	Photons for SNR=1
CCD	Kodak KAC-00401	60%	0.4416	2,759.8	88
CCD	Kodak KAI-0330	36%	0.2453	1,533.2	109
Photodiode	Perkin Elmer VTB1013	23%	0.6133	3,833.0	269
APS	Bolton et. Al (2002)	55%	0.0021	13.1	7
APS	El Gammal (2006)	40%	0.4906	3,066.4	139
APS	IBIS (This work)	40%	0.0832	520.0	51

Part B: Photon-counting Devices					
Type	Part	Quantum Efficiency (470 nm)	Dark Current (pA)	# charges	Photons for SNR=1
PMT	Perkin Elmer C982	15%	0.0005	3.0	12
PMT	Hamamatsu H7115	15%	0.0320	50.0	51
SPAD	Gulinatti (2005)	35%	6.0000	37500.0	554
SPAD	Daniel (2008)	40%	17.280	108,000.0	288
SPAD	IBIS	60%	19.753	123,500.0	586
APD	Hamamatsu MPPC-100	73%	48.000	300,000.0	751
APD	Hamamatsu MPPC-100	1%	0.960	6,000.0	5,310

The rate of generation depends on the material, doping level, defects, and biases of the junction. While the average dark current can be subtracted from the output of the system, the current closely resembles a Poisson process, and therefore the random fluctuations due to this generation process degrade the SNR of the system.

6.2 Review of low-dark current CMOS devices

Several techniques have been developed to minimize the dark current through careful selection of materials, pixel geometries, and architectures.

6.2.1 Materials

Both the quantum efficiency and noise performance of active pixel sensors are determined by the material properties of the photo-active area. In typical commercially available CMOS processes, the active area is created by one or a combination

of photogates, photodiodes or photo-transistors. Photogates use an applied voltage on a gate oxide above a silicon area to deplete carriers and create a potential well. Photogates have high quantum efficiency but suffer from higher noise due to additional lattice imperfections at the silicon-oxide interface. Alternatively photodiodes are created form p-n junctions. These junctions are typically n^+/p_{sub}, n_{well}/p_{sub} and p^+n_{well}. The junction depth determines the spectral characteristics of the photon quantum efficiency while the doping levels determine the noise characteristics. Photodiodes created from n_{well}/p_{sub} junctions have the highest SNR [136] Many industrial processes use what is known as a pinned photodiode. These structures are comprised of a n-type material sandwiched between the p-type substrate and a later of p+, essentially forming two junctions. This method reduces the noise caused by surface defects by connecting them to ground rather than the integration node. This method also increases the quantum efficiency by using two junctions rather than just one.

6.2.2   Geometry

The quantum efficiency and noise performance of active pixel sensors are also dependent on the geometry of the active area. Increased doping concentration decreases the junction width while increasing lattice imperfections giving rise to a higher number of intermediate electron state and therefore increasing the junction thermal noise. Additionally, active area shape determines the local electric field which can give rise to field assisted carrier generation or quantum tunneling. The geometric effects on device performance have been discussed elsewhere [137].

6.2.3 Architecture

From an architectural perspective, dark current can be reduced by current skimming or limiting the applied bias voltage across the detector junction. The current skimming approach adds an additional current equal in magnitude but opposite in direction to that of the dark current. While current skimming reduces the fixed patter noise that arises from the dark current, it actually increases the overall noise because there are now two noise sources the detector junction and the additional in-pixel current source. Alternatively it has been demonstrated that limiting the voltage across the detector junction decreases the magnitude of the dark current and also reduces the resulting temporal noise in the system.

This work focuses on a system approach which reduces dark current generation by reducing to reverse bias across the p-n junction to nearly zero. Reducing the reverse bias of the p-n junction to zero reduces the net thermally generated current flowing across the junction to zero. While the forward and reverse current are equal in magnitude making the total current across the junction zero, each current contributes to the overall noise of the system. However, it has been shown that not only does this biasing regime minimize the thermally generated dark current, but it also maximizes the overall SNR, despite marginally lower quantum efficiency [2]. To minimize the reverse bias of the p-n junction, both transistors and capacitive trans-impedance amplifier pixels have been utilized [34, 36].

While the capacitive trans-impedance amplifier (CTIA) pixel can efficiently bias the junction near zero while decoupling the gain from the size of the photo-active

area, these devices suffer from mismatch. Typically, input-referred mismatch across the chip and from device to device has a standard deviation of over 10 mV. While this may not seem significant, most of the noise suppression comes when the reverse biases is within a few millivolts of zero. For arrays of devices this input-referred mismatch means that a bias must be chosen near zero but high enough to avoid forward-biasing some of the p-n junctions.

Figure 6.3 shows the experimental results of dark current as a function of reverse bias. An increase in bias of 10 mV can double the dark current.
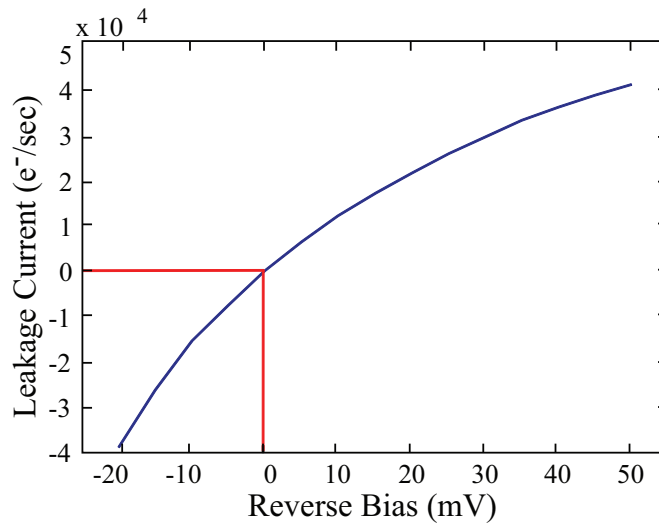
Figure 6.3: Dark current as a function of reverse bias of a circular n-well/p_{sub} junction near 0 V.

6.3   The CTIA Pixel

Capacitive trans-impedance amplifier pixels use a trans-impedance amplifier with a capacitor in the feedback path to integrate the photo-current while maintaining a fixed potential at the photo-diode node. The schematic of the pixel is shown in
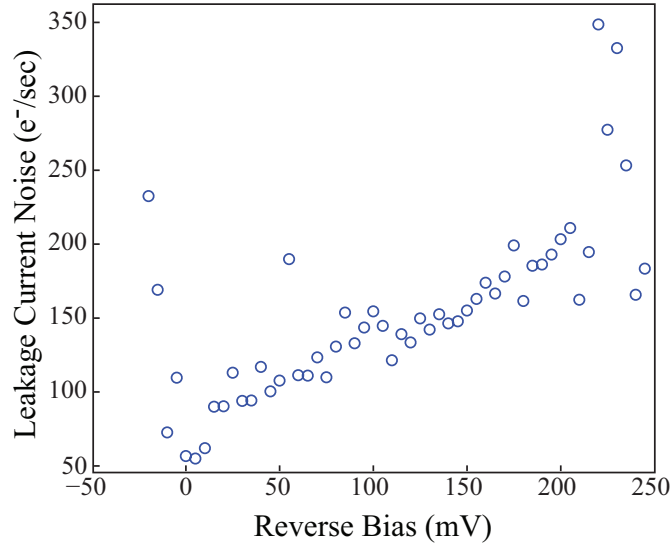
Figure 6.4: Dark current noise as a function of reverse bias of a circular n-well/p_{sub} junction near 0 V.

Figure 6.5 and is similar to that proposed by Vijayaraghavan *et al.*, except the pixel provides an analog output rather than a pulse-rate output [138]. An analog output allows the use of a multiple non-destructive sampling scheme which provides a richer description of system dynamics. The photodiode is connected to the negative terminal of the amplifier with an NMOS transistor acting as a switch between the photo-diode node and an external reset voltage V_{pd_rst}. The positive terminal of the amplifier is connected to an external bias, V_{comm}, which dictates the reverse bias of the p-n junction, V_{pd}, when the system operates in integration mode. A capacitor, C_{int}, connects the output of the amplifier back to the negative terminal of the amplifier to provide feedback and act as an integrator. An additional amplifier in unity-gain configuration is connected through a switch to the output of the CTIA. Because both inputs of the CTIA are near ground, the output of the CTIA is in open loop, but not well defined, and the unity gain amplifier forces the starting integration voltage in

the pixel. Finally, a third amplifier in a unity gain configuration buffers the output

off-chip. A schematic of the amplifiers is presented in Figure 6.6.
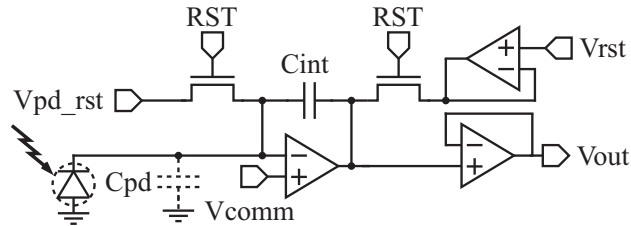
Figure 6.5: Schematic of pixel architecture. Pixel is reset to V_{pd} during reset phase, and held to V_{comm} during the integration phase. V_{out} is set to V_{rst} during the reset phase, and rises as C_{int} collects photo-induced electrons [7].
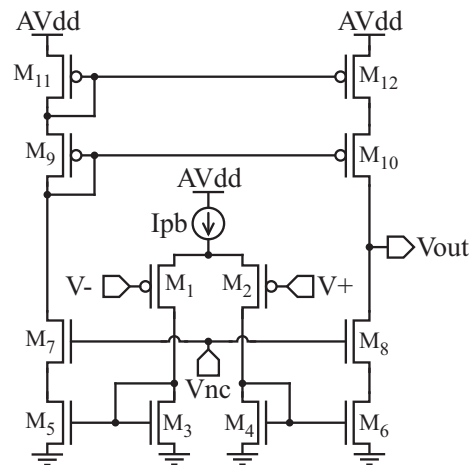
Figure 6.6: Schematic of in-pixel amplifier [7].

6.3.1 Amplifier Noise Analysis

The readout noise of the sensor is due to the intrinsic physical noise sources

of the MOSFETs in the source follower and readout buffer. The noise sources in

the transistors include: 1) thermal noise due to the random thermal motion of the

120

electrons in the channel and 2) flicker noise due to mobile carriers being trapped or released from interface traps at the silicon-oxide interface. These two noise sources are modeled by current sources across the drain source terminals as [96]:

$$S_{I_d} = 4\gamma kT g_m + \frac{K_f I_d}{C_{ox} W L f}$$

(6.3)

where $\gamma = 2/3$ or $1/3$ depending on the region of operation, K_f is a process dependent parameter and C_{ox}, W and L are the oxide capacitance per unit area and the geometric parameters of the MOSFET. Each noise source is then referred to the input node, summed and integrated over the bandwidth as:

$$v_{n_{rdout}}^2 = \int_{-\infty}^{\infty} S_{v_{in}}(f)\, df$$

(6.4)

A schematic for the amplifier is shown in Figure 6.6. Experimental results indicate that the chip noise is 915 μV.

6.3.2 Pixel Quantum Efficiency

The quantum efficiency of the N$_{well}$/p$_{sub}$ junction was experimentally determined and shown in Figure 6.3.2. A similar test setup to that described in Chapter 3 Figure 3.8 was used. A monochromator (Newport Cornerstone 260 1/4M, model 74100) was used to select specific wavelengths with spectral resolution of 2 nm. The light intensity was independently measured using a calibrated photometer (Newport 818-UV) fitted with a 5 mm diameter pinhole and an optical power meter (Newport

1830-C). For each trial, an integration time of 0.1 seconds and the photo-response of the pixel was taken at a sampling rate of 1000 samples/sec. For each wavelength, 100 trials were performed, and the average quantum efficiency has been reported for each wavelength. The quantum efficiency was determined by measuring the photo-response of the pixel and dividing the slope of the output voltage by the electron conversion gain to obtain the number of electrons generated per second and compared against the known photon flux. The peak quantum efficiency is 40% at 450 nm, and the quantum efficiency drops to 35% at 500 nm, corresponding to bioluminescent wavelengths.
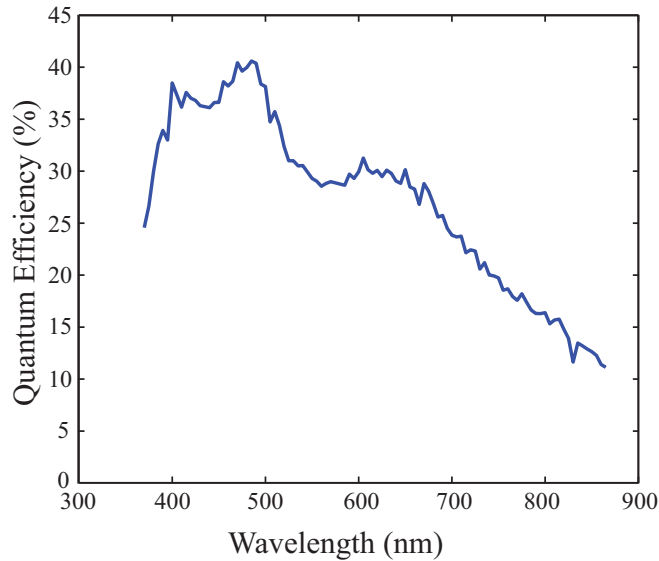
Figure 6.7: Quantum Efficiency of a 0 V reverse bias N_{well}/p_{sub} as a function of wavelength.

6.3.3 Pixel Operation

The operation of the pixel is as follows: During reset, the photodiode node and the positive terminal of the CTIA amplifier are set to V_{comm}, and the output of the CTIA is set to V_{rst}. After reset both NMOS switches open the CTIA is sent

into a feedback mode. Ideally, the photodiode is held at V_{comm} through amplifier feedback and as electrons are generated in the p-n junction pulling voltage V_{pd} lower, the output of the CTIA rises to compensate and hold V_{pd} at V_{comm}. In integration mode, the change in voltage due to an electron generated at the photo-diode is:

$$\Delta V_{photon} = \frac{q}{C_{int}} \tag{6.5}$$

In practice, mismatch, reset switching charge injection, and reset noise can be seen by an immediate jump in the output voltage. A representative voltage trace is shown in Figure 6.3.3.
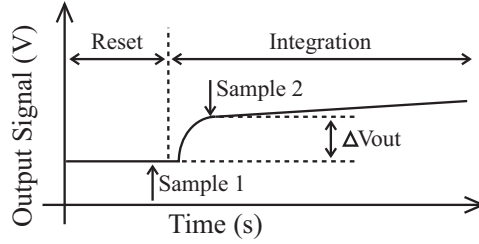
Figure 6.8: Representative drawing of time trace of output voltage during reset and integration period. ΔV_{out} arises from charge injection, reset noise, and amplifier mismatch, and can be observed by successive sampling during the reset and integration phase [7].

This initial jump follows the equations relating the change in voltage at the photodiode node to the change in voltage at the output as described by Equation 6.6

$$\Delta V_{out} = G_{\Delta V_{in}} \Delta V_{in} = \frac{C_{pd}}{C_{int}} \Delta V_{in} \tag{6.6}$$

where ΔV_{in} is the change in input voltage, C_{pd} is the photodiode capacitance, C_{int}

123

is the integration capacitance, and ΔV_{out} is the resulting change in output voltage. While the effect of the charge injection, mismatch, and reset noise all cause an initial jump in the output of the CTIA, only mismatch causes the photodiode node, V_{pd}, to shift away from V_{comm} during operation. Based on prior fabricated test data the input-referred mismatch is on the order of 10 mV.

6.4 Experimental Results of CANARY Cell Detection

To demonstrate the effectiveness of the CTIA pixel as a bioluminescence detector, an experiment was performed using CANARY cells in cell media. The experimental group consisted of CANARY cells and cell media, while the control group consisted of only cell media. This control group ensures that any observed response is due to bioluminescence, and not electromagnetic coupling due to a pH change in the ionic solution. In each experiment, ionomycin was then added via micro-syringe to initiate a cellular response. Ionomycin is a common stimulant which raises the internal calcium level of cells. This rise in calcium initiates a biochemical cascade which produces bioluminescence. The bioluminescence is the detected by the sensor. The experimental test setup is shown in Figure 6.9. The CMOS chip and test board were mounted in a Serpac Light-Tight Enclosure. A syringe was used to deliver ionomycin to the sample contained in a small well on top of a glass slide covered with indium tin oxide (ITO). A National Instruments USB-6259 data acquisition card provided

the control signals and acquired the sample measurements.
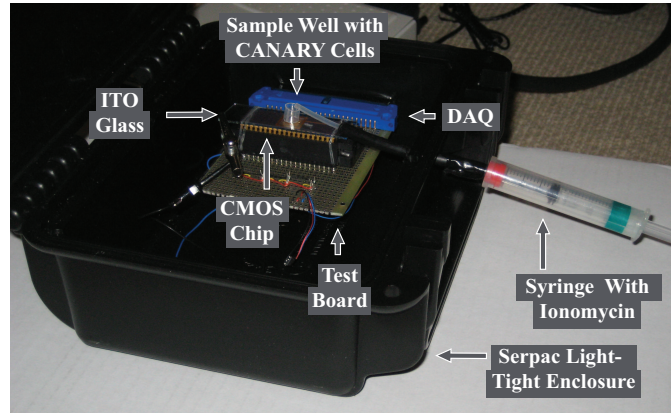
Figure 6.9: Experimental setup detecting CANARY cells in cell media in response to application of Ionomycin.

Initial tests showed that due to the high front-end gain of the detector and the relatively large volume of ionic fluid, the sensor produced a strong response due to movement of the microsyringe and the addition of the ionomycin to the cell media. There are several ways to mitigate this kind of interference including adding an electro-chemical ground to the solution or ensuring that the pH of each solution is maintained. Overcoming interference in this experiment was achieved using a glass slide covered with indium tin oxide (ITO), a well known transparent conductive material that acts like an electric shield.

Both the experiment and control were performed where the detector was interrogated at a sampling rate of of 2000 samples/second. To overcome the readout noise in the system, a running average 2000 points was used to filter and smooth the response. Since the detector is an integration-based system, the results were downsampled to a rate of one sample per second the change in voltage was calculated between successive samples and converted to the units of electrons/second using the

125

detector conversion gain of the sensor. The results in Figure 6.10 clearly indicate that a bioluminescence response was observed in the CANARY cell experiment with a maximum response of 1500 electrons/second, and no response was observed in the control experiment. Based on the I-V curve in Figure 6.3 it is clear that if the detector was not biased within 2 mV of ground, the bioluminescnce signal would have been completely overwhelmed by dark current. These results emphasize the need for optimally biased detectors.
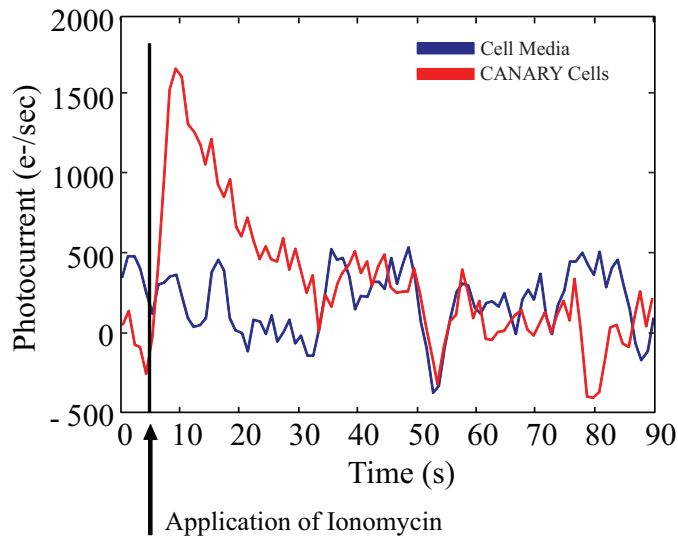
Figure 6.10: Experimental results detecting cell media and CANARY cell response to application of Ionomycin.

This work demonstrates an offset correction technique to minimize the offset which appears in the feedback amplifier of CTIA pixels thereby minimizing the dark current across the array. This offset correction technique utilizes a non-volatile analog offset correction mechanism in the form of floating gate transistors. Floating gate transistors store an analog voltage offset in non-volatile memory in the form of an electrically isolated gate of a transistor. The physical mechanisms are similar to

126

those used in flash drives. The circuit uses an in-direct programming method with a combination of tunneling and hot carrier injection to either add or remove charge as necessary. Offset correction is performed sequentially until the offset has been minimized within the limits of the process.

6.5   Mismatch: Monte Carlo Simulations

Monte Carlo simulations were performed with the Cadence Analog Environment. To accurately model mismatch in the system, length and width mismatch were assumed to have a standard deviation of 3 %, and a standard deviation in threshold mismatch of 5 mV. Two hundred trials were simulated. The output of the pixel, and the photo-diode voltage as a function of time are shown in figure 6.11(a) and 6.11(b) respectively. During reset the photodiode voltage is all set to 0 V, while the output voltages are set to approximately 1 V. The approximation is due to the mismatch associated with the in-pixel voltage buffer. An initial jump in voltage is observed due to any offset or charge injection in the system but settles within 10 ms. Histograms of the change in photodiode voltage and output voltage during reset and 10 ms after reset are shown in Figure 6.12(a) and 6.12(b) respectively. The change in the output voltage is a scaled version of the offset and follows Equation 6.6. Figure 6.13 shows a scatter plot of the change in input offset against the change in output voltage. As expected there is a clear inverse correlation between the input offset and the output offset, indicating that the observation of the jump in output voltage is a valid metric to correct the input offset within the system. The results of these Monte Carlo sim-

ulations indicate that the standard deviation of the photodiode node voltage is 7.7 mV and the standard deviation of the output node voltage is 93 mV.
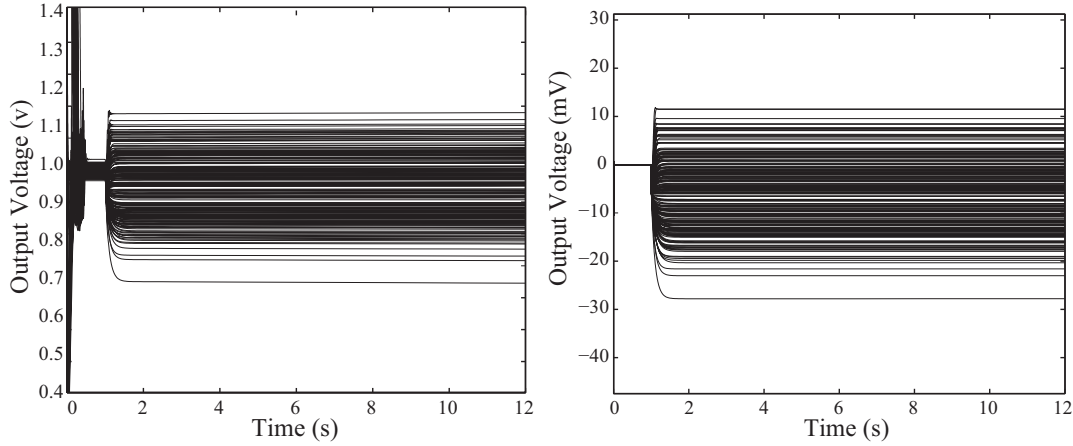
(a) Voltage trace as a function of time of the output voltage for 200 Monte Carlo simulations [7].

(b) Voltage trace as a function of time of the photodiode node voltage for 200 Monte Carlo simulations [7].

Figure 6.11: Voltage traces as a function of time.
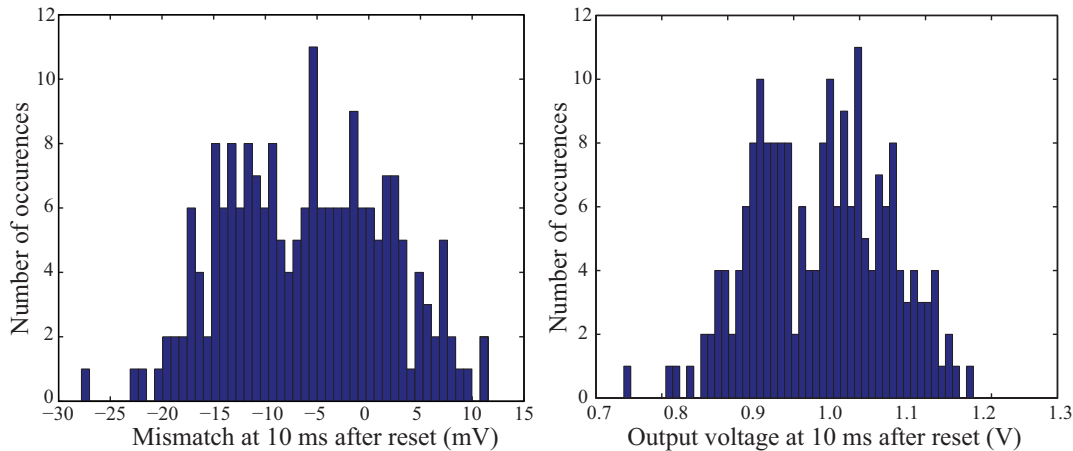
(a) Histogram of the photodiode voltage 10 ms after the start of the integration cycle.

(b) Histogram of the output voltage 10 ms after the start of the integration cycle.

Figure 6.12: Histogram of voltage mismatch at the photodiode node voltage and output node voltage.
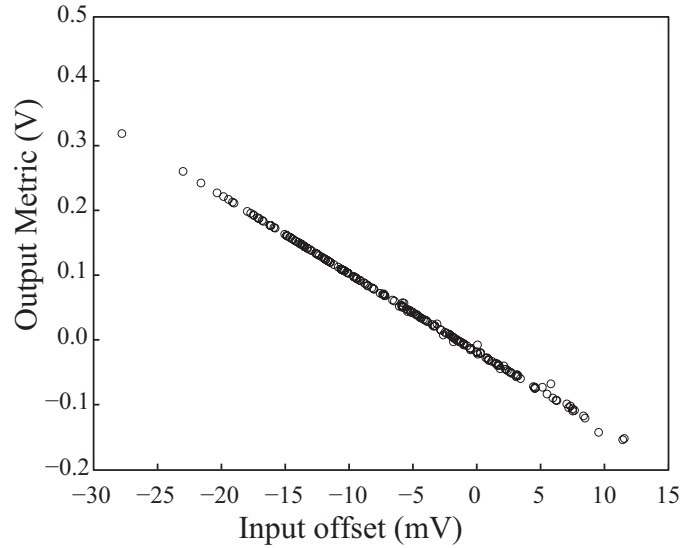
Figure 6.13: Scatter plot of the jump in voltage at the output plotted against the jump in voltage of the photodiode node, indicating an inverse correlation between output metric and input-referred offset [7].

6.6   Effects of Scaling

An important aspect of any system is its performance as a function of device size and technology. In many cases, mismatch does not significantly improve as technology size decreases. However, the doping concentrations tend to increase, subsequently increasing field assisted dark current generation. As a result, forcing a 0 V reverse bias on the detector junction will become more important for future technologies. Other effects include increasing the size of the detector, or decreasing the integration capacitance. Changes in detector size reflect the application-specific nature of these sensors, while the integration capacitance is independent of detector size and directly responsible for the front-end electron-gain. Higher front end gain reduces the effects of downstream noise and usually increases the SNR of the system. Each of these factors affects the charge injection, readout noise, or the resulting observed effect of

the mismatch.

6.6.1   Reset Noise

The pixel is designed to accommodate multiple random-access non-destructive sampling. As a result, the majority of reset noise can be removed through successive sampling. Although reset noise does not play a significant role in the SNR of the system, it does create variability in the initial offset of the pixel and therefore affects the full well capacity, which in turn affects the overall dynamic range. Full well capacity refers to the number of electrons that can be integrated before device saturation. Reset noise is present at both the photodiode node and the integration node. Equation 6.7 describes the reset noise of a simple capacitor-switch.

$$\sigma_{reset} = \sqrt{\frac{kT}{C}} \tag{6.7}$$

The output-referred noise due to the reset noise at the photodiode node is:

$$\sigma_{V_{pd}} = \frac{C_{pd}}{C_{int}} \sqrt{\frac{kT}{C_{pd}}} \tag{6.8}$$

The output-referred noise due to the reset noise at the integration node is:

$$\sigma_{V_{int}} = \frac{kT}{C_{int} + C_{int\_stray}} \tag{6.9}$$

Given a system where the $C_{pd} = 300$ fF and $C_{int} = 30$ fF, the gain is 10, the output-referred reset noise due to the photodiode node is approximately 1.17 mV,

while the reset noise at the integration node contributes approximately 0.26 mV noise. While this noise would be considerable if not for the multiple non-destructive sample, it does not severely impact the full well capacity of the pixel. If we increase the photodiode capacitance by an order of magnitude, *i.e.* increase the device size by a factor of 10, the photodiode node reset noise would jump to 6.43 mV while the integration node reset noise would remain 0.26 mV.

The output referred mismatch is scaled directly by the gain. Given $C_{pd} = 300$ fF, $C_{in}t = 30$ fF and the gain is 10. For a typical input referred mismatch of 10 mV, the resulting output-referred mismatch is 100 mV. Moreover, increasing the photodiode size by an order of magnitude to 3 pF, the output referred mismatch increases by an order of magnitude to 1 V. This increase significantly affects the full well capacity of the system. Also, recall that this is a standard deviation, not a worst-case scenario. Assuming a worst case scenario of 3σ the resulting output mismatch could be as high as 3 V, or the entire full well capacity. Since detector size is primarily dictated by application, and therefore independent of technology. Additionally, mismatch does not significantly improve with decreases in technology size, so the usable well capacity for a system in an advanced technology significantly decreases, emphasizing the need for mismatch compensation techniques.

6.7 Mismatch Compensation

In an ideal world, the manufacturing process would create perfect transistors, capacitors, resistors and every other component we use in a design. In practice small

variations occur at every step of the manufacturing process, from mask creation, to doping, to etching, to material deposition. These small variations are compounding and result in observable variability among devices. Of the variations that occur, the most common observable effects are variations in the device size, *i.e.* length and width, and for active devices variations in threshold. These variations can be systematic, due to gradients across the chip, or completely random due to ionic charge interaction. While this mismatch has a minimal effect on digital circuits, it can have a large affect on analog electronics. There are many methods for reducing the degree of mismatch from one device to another including: 1. From a manufacturing perspective, maintaining density rules. 2. From a layout perspective, using common centroid techniques and dummy devices mitigate gradient based mismatch. 3. From an architectural perspective, switch-cap based offset techniques for dynamic analog circuits can remove offsets at the expense of clock feed-through. While all the prior techniques provide some mismatch mitigation, their ability to provide sub milli-volt mismatch reduction is limited. Furthermore, under some applications it is actually desirable to introduce mismatch into the system. The afore-mentioned methods do not provide a way to introduce pre-defined mismatch in a consistent designable way with sufficient resolution. More recently, several analog non-volatile storage mechanisms have been reliably integrated into production-based CMOS processes to achieve analog trimming. Of these non-volatile storage mechanisms, floating gate structures provide a mechanism to achieve on-chip analog mismatch compensation.

6.7.1 Floating Gate Devices

Floating gate circuits use MOSFET devices with an electrically isolated gate. The electrical isolation is achieved with a layer of oxide directly covering the gate. These electrically isolated devices use some of the same physical principles behind the success of EPROM, EEPROM, and todays common flash drives. Floating gate circuits have been used in a number of component architectures, including: trim current sources, autozero amplifiers, cancel/store offset in comparators and ADCs, to correct non-linearity in image sensors, store large arrays of analog parameters, as well as neuromorphic applications [139–144]. Floating gate devices generally rely on two underlying mechanisms for non-volatile charge storage hot carrier injection and Fowler Nordheim tunneling.

6.7.2 Hot carrier injection

Hot carrier injection occurs when a carrier (electron or hole) gains enough energy to surmount the energy barrier of the insulator (gate oxide). For transistors, this occurs under specific conditions. In silicon, electrons or holes gain momentum in the presence of an electric field. Due to lattice imperfections, impurities, dopants and phonons. These electrons experience collisions which reduce their momentum and overall energy. It low electric fields the total electron energy remains relatively low, and this process results in a linear relationship between the electron drift velocity and the applied electric field. At high electric fields; however, the electron can gain sufficient energy to exceed the 1.41 eV required to break an electron-hole pair bond

and cause impact ionization. In this scenario, some fraction of the electrons create additional mobile electron-hole pairs. These electrons with excess energy above the barrier voltage are considered to be hot carriers. These hot carriers are capable of surmounting the oxide barrier and in the presence of a vertical electric field are injected onto the electronically isolated gate node. This injection current can be modeled following the equation described in Equation 6.10 where I_{s0} is the current through the transistor, α, β, and δ are fit parameters based on test data, V_{gd} is the gate to drain voltage and V_{gs} is the gate to source voltage [8].

$$I_{inj} = \alpha I_{s0} exp \left[-\frac{\beta}{(V_{gd} + \delta)^2} + \lambda(V_{gd} - V_{gs}) \right] \tag{6.10}$$

6.7.3 Tunneling

Flowler-Nordheim tunneling (tunnelling) operates by an entirely different mechanism from hot-carrier injection. Fowler-Nordheim tunneling is a quantum effect. Quantum theory dictates that electrons act as both particles and waves. In addition, an electron's position follows a probabilistic density function known as the time-independent Schroedinger equation, which is shown in Equation 6.11,

$$-\frac{h}{2m}\frac{d^2}{dx^2}\Psi(x) + V(x)\Psi(x) = E\Psi(x) \tag{6.11}$$

where $\hbar$ is Planck's constant divided by 2π, m is the mass of the particle, x is the particle position in one dimension, Ψ is the Schroedinger wave function, and V(x) is the potential energy of the particle.

This probability density function dictates that rather than an electron having an exact position, it can be found on a continuum of positions with some probability. The most important aspect of quantum theory, with respect to tunneling, is that these probability density functions are continuous with respect to position, and therefore do not necessarily go to zero at the boundary of a potential well, or a discrete change in potential barrier height, such as the channel to the gate oxide of a device. As a consequence, if the potential barrier is sufficiently narrow, there is a finite probability that an electron will "appear" on the other side of the barrier.

Tunneling occurs when a sufficient voltage is applied across an insulator. For MOS devices, the tunneling voltage is applied to the gate of the transistor with respect to the source, drain and body which are all tied together and described by Equation 6.12, where I_{tun0} is a scale current, W and L are the width and length respectively, V_{ox} is the voltage across the oxide, and V_f is a constant that varies with oxide thickness[8]. Schematic, layout and cadence simulation models are shown in Figures 6.14, Figure 6.15, Figure 6.16 respectively. A special cadence representation is needed to overcome the floating node condition that arises in the simulator due to the electrically isolated floating gate node.

$$I_{tun} = -I_{tun0}WLe^{\left[-\frac{V_f}{V_{ox}}\right]} \qquad (6.12)$$
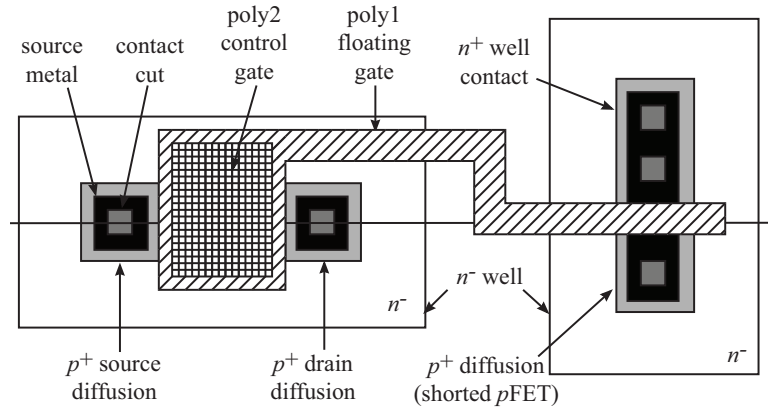
Figure 6.14: Layout of typical floating gate injection and tunneling structures [8].
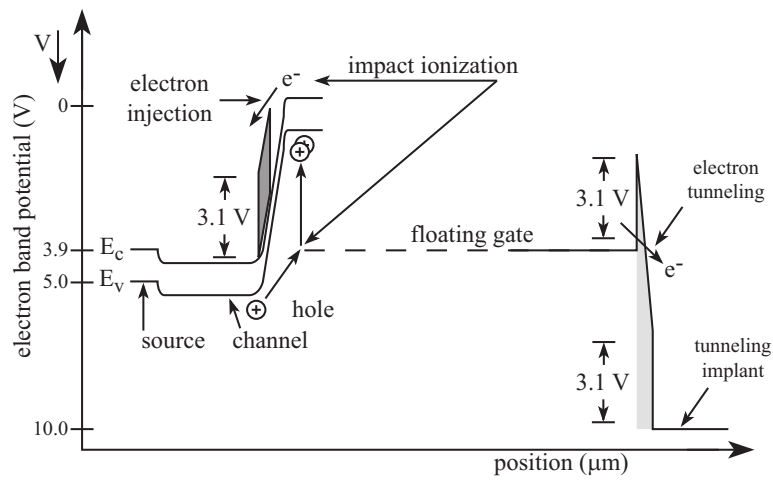
Figure 6.15: Floating gate band diagram for injection and tunneling [8]
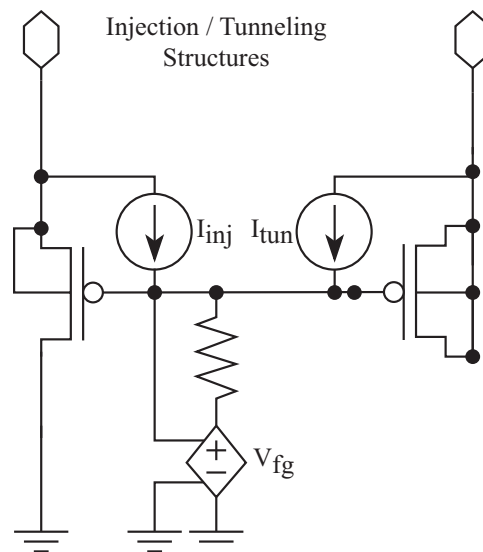
Figure 6.16: Schematic of Cadence floating gate representation for simulations.

136

Table 6.3: Summary of Other FG Pixels

Author	Year	Detector Type	Array Size	Programming Method	Programming Reference	Programming Style	Programming Objective	Mode of Operation
M. Zhang *et al.*	1995	Photodiode	8 x 9	Tunneling	Intra-pixel	Parallel	Minimize FPN	Integrating
A. Aslam *et al.*	1998	Floating Bulk	128 x 1	Tunneling	Extra-pixel	Sequential	Minimize FPN	Continuous
M. Cohen *et al.*	2001	Vertical PNP	64 x 64	Injection	Extra-pixel	Sequential	Minimize FPN	Continuous
A. Pesavento *et al.*	2002	Photodiode	26 x 1	Injection & Tunneling	Intra-pixel	Parallel	Minimize FPN	Continuous
Y. Wong *et al.*	2007	Photodiode	144 x 144	Injection	Intra-pixel	Parallel	Minimize FPN	Continuous
G. Fikos *et al.*	2008	Photodiode	32 x 32	Injection	Intra-pixel	Sequential	Minimize FPN	Continuous
This Work	2011	Photodiode	16 x 16	Injection & Tunneling	Extra-pixel	Sequential	Maximize SNR	Integrating

6.7.4   Other FG Image Sensors

There are several examples of image sensors with floating-gate mismatch compensation. For brevity only the most significant work from each author is discussed. While each design is slightly different the overall objective is to minimize pixel-to-pixel mismatch across the array. One of the earliest examples of in-pixel mismatch compensation using floating gate transistors was by M. Zhang *et al.* which uses an in-pixel parallel tunnelling programming technique for a binary image sensor [145]. A. Aslam *et al.* Aslam used the floating bulk of a PMOS transistor as a detector with electron tunneling directly into the device [146]. Cohen *et al.* In 2001 Cohen et al. demonstrated a logarithmic pixel using injection to achieve extra-pixel serial adaptation [147]. A. Pesavento *et al.* Performs a spatial derivative function while removing its offset through both injection and tunneling with an auto-zeroing floating gate amplifier [148]. Wong *et al.* In 2007 Wong et al. demonstrated a design similar to Cohen *et al.*, a logarithmic pixel that utilizes floating gates injection to minimize mismatch, however programming was achieved in parallel dramatically speeding up programming time [142]. G. Fikos *et al.* In 2008 Fikos et al. demonstrated a logarithmic pixel that utilizes in-pixel injection [149]. All of the devices mentioned above focus on minimizing the fixed pattern noise, or in some cases introducing fixed pattern noise . While removing fixed pattern noise increases image quality and dynamic range, much of the benefit can be replicated by off-chip signal processing. For the binary image sensor reducing the mismatch actually occurs in a comparator along the readout path. This trimming simply changes the threshold voltage of the comparator

in each pixel so that each pixel has the same temporal response a specific input light intensity. For the continuous time systems described above, mismatch results in a fixed DC voltage variation at the output of the system . While this fixed variation may reduce dynamic range, similar mismatch reduction can be accomplished through digital post-processing. These systems remove this fixed DC offset but do nothing to address the inherent noise in these systems. In many cases, the offset correction actually introduces more noise by increasing the current.

The purpose of the work herein is to minimize the dark current at the photodetector and hence maximize the SNR of the system. This is a subtle but significant difference compared to the other offset correction systems. Reducing the dark current not only minimizes fixed pattern noise associated with the dark current, but also minimizes the resulting temporal noise due to the dark current. Unlike the previously described methods this leads directly to an increase in dynamic range as well as an increase in the overall signal to noise ratio of the system.

6.8 System Architecture

Floating gate compensation can be used to minimize fabrication mismatch or other static offsets in a design. Compensation works best when the injection and tunneling process occur as near to the circuit operating point as possible. In this system, the voltages at the inputs of the amplifier are near 0 V allowing tunneling, but making injection difficult due to the voltage requirements for tunneling and injection process. As a result, a different compensation configuration must be used.

6.8.1 Pixel Architecture

The pixel described herein is nearly identical to that shown previously, except the CTIA amplifier has been modified to include a floating gate on transistor M_{12} in schematic 6.6. A schematic of the resulting CTIA with floating gate compensation is shown in Figure 6.17. To assess the viability of performing offset correction at a floating gate transistor M_{12}, the correlation between the input-referred mismatch to the mismatch at the gate of transistor M_{12} was simulated. While the introduction of a floating gate decreases the coupling efficiency to the channel of the transistor due to the resulting capacitive divider, there is little effect on circuit performance because the operational gain is dictated primarily by the feedback capacitor. Figure 6.18 shows a histogram of the voltage mismatch at the gate of transistor M_{12}, corresponding to a standard deviation in output voltage of 4.3 mV.
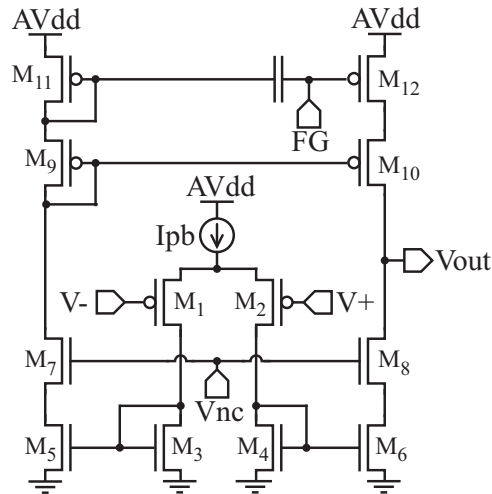
Figure 6.17: Schematic diagram of the CTIA amplifier with a floating gate on transistor M_{12}

Figure 6.19 shows a scatter plot of the change in voltage at PMOS transistor

140
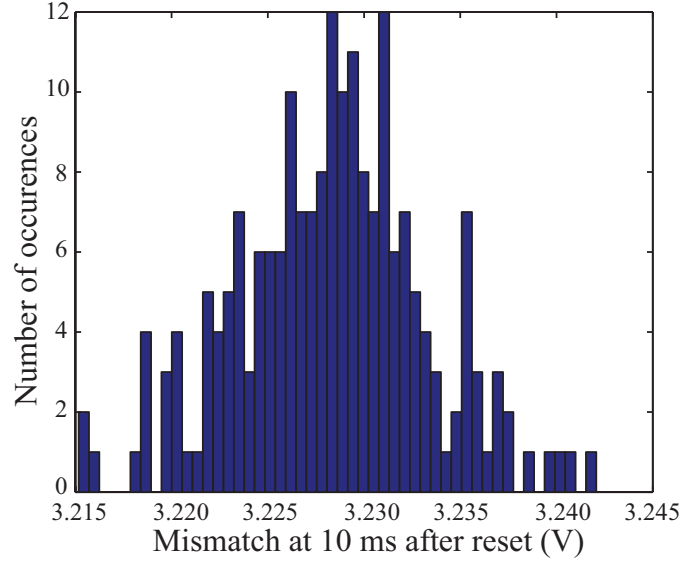
Figure 6.18: Histogram of offset voltage at the gate PMOS transistor after 10 ms

M_{12} against the input-referred offset. There is a clear inverse relationship between the mismatch at these two nodes.

To achieve mismatch compensation separate injection and tunneling structures were included in each pixel, and are the same as those described in [150, 151]. The injection/tunneling structure is shown in Figure 6.20. Depending on the I/T control bit, this structure either produces a pulse which injects a small packet of charge onto the floating node or tunneling which tunnels a small packet of charge off the node. Supply voltage V_{tun} dictates the magnitude of the current tunneled onto the floating node, while I_{Vdd} and V_{binj} determine the magnitude of current injected onto the floating node. The pulse duration can also be used to control the amount of charge injected/tunneled off the floating node.

141
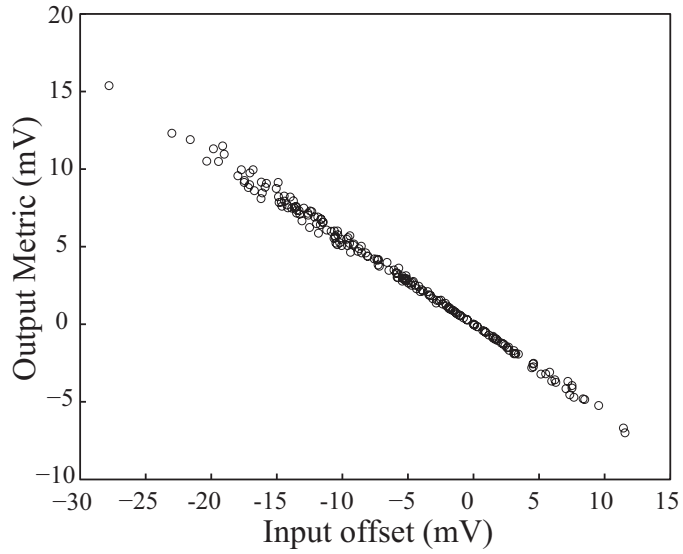
Figure 6.19: Scatter plot of the jump in voltage at the gate of PMOS transistor plotted against the jump in voltage of the photodiode node, indicating an inverse correlation between output metric and input-referred offset
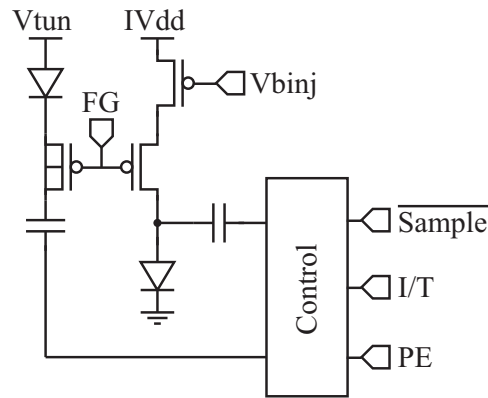
Figure 6.20: Schematic of an indirect injection/tunneling structure used to reduce amplifier mismatch

6.8.2 Array Architecture

The array architecture is shown in Figure 6.21. This system consists of an array of floating-gate based CTIA pixels with random access peripheral control to allow multiple non-destructive sampling of each pixel and provide better statistics about system performance. A chip level amplifier buffers the pixel voltages off-chip. Additionally, a single pixel is included and is shielded by metal. This shielded pixel provides a dark reference that is used to determine and set global biases. The chip layout is shown in Figure 6.22.
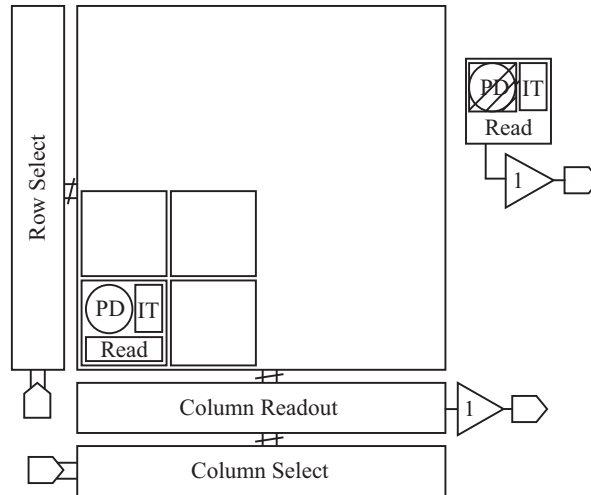
Figure 6.21: Schematic of pixel array, with row and column access circuits, individual pixels include a photodiode (PD), Injection/Tunneling circuit (IT) and readout electronics (Read).

The chip level simulation training sequence is as follows: 1. A pixel is selected from the array 2. The output voltage is sampled during reset 3. The output voltage is sampled 10 ms after the start of the integration cycle 4. The difference in the output voltage at during reset compared to after reset dictates whether injection or tunneling will occur. In this case, a positive jump in output voltage indicates that the

143
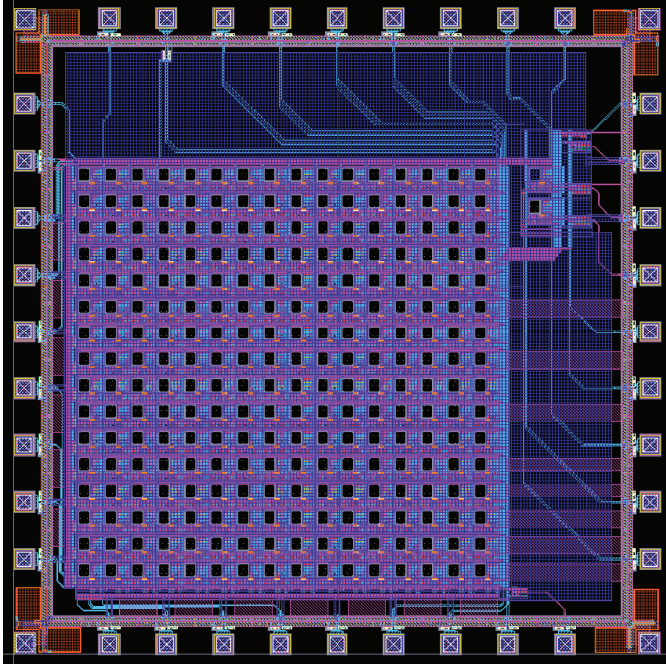
Figure 6.22: Layout of entire chip.

voltage on the floating gate must increase i.e tunneling is required, while a negative jump in offset indicates the voltage on the floating gate must decrease i.e. injection is required. 5. A short digital pulse is provided to either the injection or tunneling circuit to add or remove a small packet of charge from the floating gate. 6. The evaluation process is repeated bringing the offset successively closer to zero. 7. The entire programming process is then repeated for the next pixel in the array.

As mentioned, both reset noise and charge injection also cause an initial jump in the output voltage. The dark current across the detector junction is a function of the reverse bias across the device. As the voltage across the device approaches zero, the net current flow also approaches zero. To overcome the effects of dark current, a small packet of charge is either injected onto or tunneled off of the floating gate nodes at each training cycle. As each successive training cycle brings the reverse

144

bias of the detector closer to 0 V, the net dark current also becomes closer to zero. Although the jump in output voltage due to reset noise may be relatively large, the actual variation at the photodiode node will be small as the kTC noise is spread over the larger photodiode capacitance. In addition, kTC noise is random zero-mean noise, so successive training cycles will drive the mean offset towards zero. Charge injection on the other hand is a non-zero mean process. But again, the actual change in voltage at the input of the transistor is relatively small. In addition, so long as the charge injection is similar to that of the other pixels, the resulting offset correction will be a similar DC offset across every pixel. This offset across the array can then be compensated for through a global bias. To summarize, the effects of dark current tend to zero after successive training intervals, the effects of reset noise are white Gaussian so the net effect on training is negligible over a sufficient number of training cycles, and the effects of charge injection are small and similar across the array such that they can be compensated for by using a global bias.

6.9   Monte Carlo Simulations after tunneling-injection

To assess the ability of correcting the input-referred offset, the input-referred offset of Monte-Carlo simulations were scaled by an ideal calculated offset, representing the charge applied to the floating gate component. A representative voltage trace is shown in Figure 6.23 while the resulting histogram of the input-referred offset is shown in the following Figure 6.24:

The resulting standard deviation of the input-referred mismatch is 196 μV. A

145
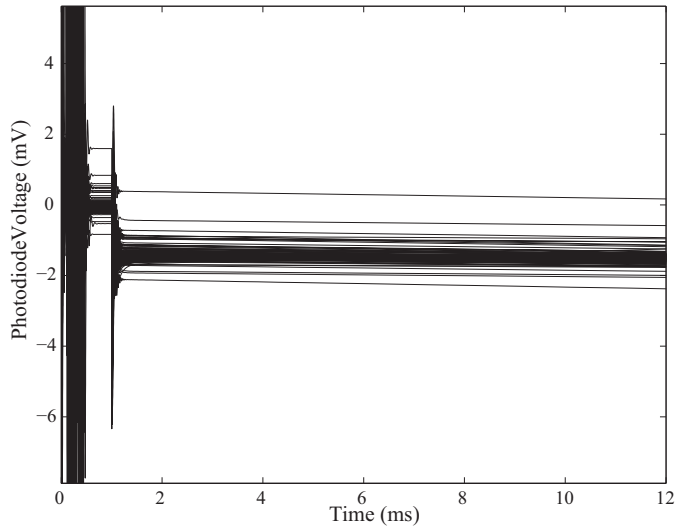
Figure 6.23: 200 Monte Carlo simulations: photodiode voltage traces as a function of time after mismatch compensation.
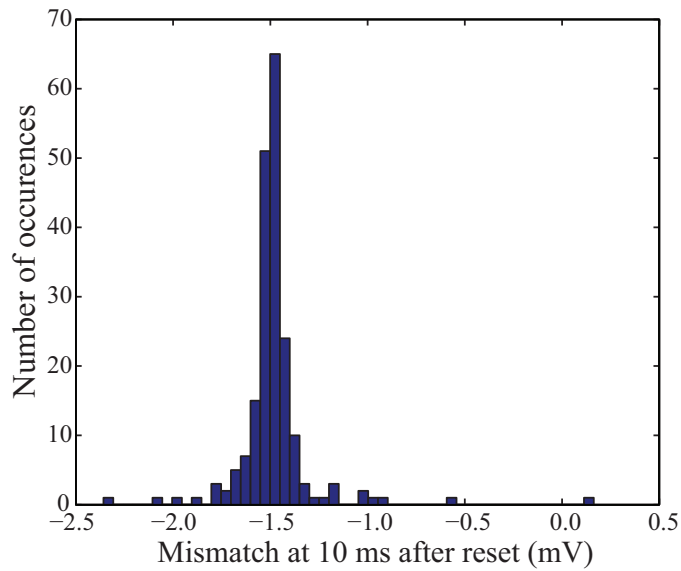
Figure 6.24: Histogram of the photodiode voltage after mismatch compensation 10 ms after the start of the integration cycle.

corresponding reduction of approximately 40 X. In practice, the ability to correct this mismatch will rely on several factors primarily dictated by other noise sources in the system. It is apparent that there is an input-referred offset of approximately -1.5 mV in the corrected system. As previously mentioned, while global offsets are not ideal, they can be corrected through a global bias. The reduction in offset affords an average lower reverse bias across the p-n junction of each pixel across the array. This subsequent reduction in reverse bias decreases the overall average dark current and thus reduces the noise and increases the SNR across the array. As a matter of practice, the lowest bias that can be set for the device across the away should be at least three times the standard deviation of the input-referred offset to ensure all diodes are reversed biased.

6.10 Experimental Results

The design was fabricated in a 0.5 μm process. A micro-photograph of the chip is shown in Figure 6.25(b). While the calibration method described above worked well in simulation, the change in voltage due to charge injection, approximately 1 V, was too large to use the mismatch metric previously described. As a result the output metric could not be used to determine the sign or magnitude of the mismatch. For the experiments below, the dark current was instead estimated over the duration of the integration time for each pixel, resulting in a longer calibration time.

The initial dark current statistics were collected for the pixels across the chip. In this work these statistics are referred to as foundry statistics. An integration time

147

|(a) Picture of PCB|(b) Picture of CTIA chip,|(c) Picture of CTIA pixel|
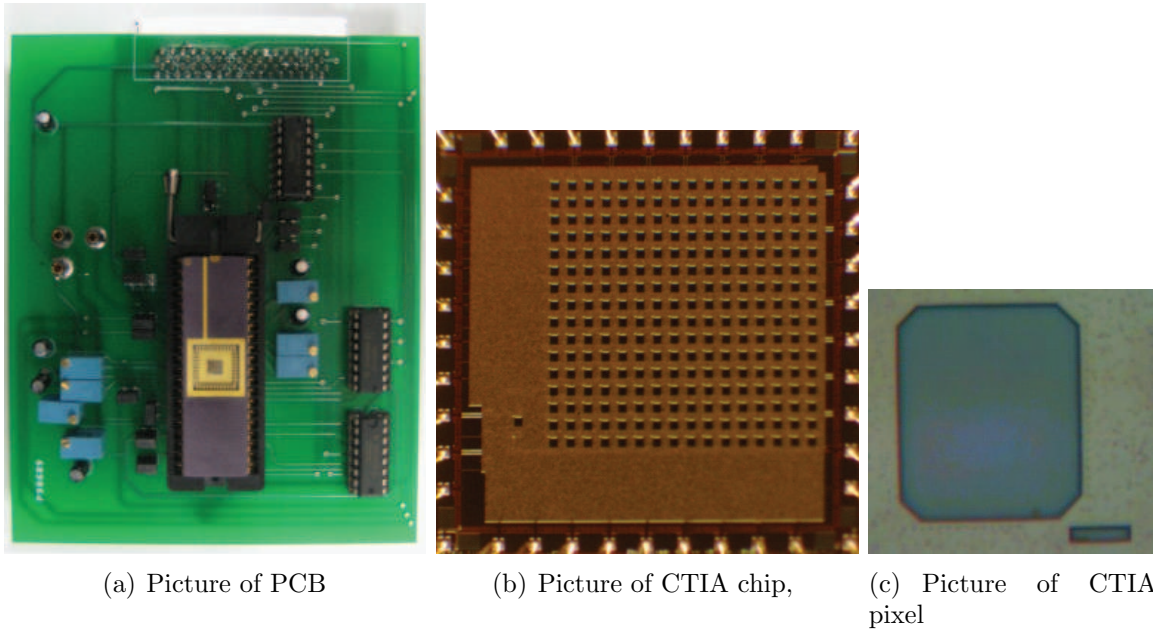
Figure 6.25: Picture of the CTIA based (a) PCB, (b) chip, and (c) pixel.

of 1 second was chosen, and the dark current of each pixel in the array was measured by estimating the slope using a least-squares fit of the output voltage taking into account the appropriate electron conversion gain. Programming was then enabled, with a tunneling voltage, V_{tun}, of 8.2 V and a charge pump voltage supply of of 5 V. For each iteration, the pixels were integrated for 1 second and the slopes were estimated using the same least-squares fit method. Depending on the slope of the voltage trace injection or tunneling was performed. In this experiment, if the current was greater than 10,000 e$^-$/sec tunneling was performed, if the current was less than 10,000 e$^-$/sec injection was performed. The units of electrons per second are used to easily compare this system against other systems using the noise effective power metric. The magnitude of the tunneling and injection voltage supplies and the programming bounds dictate the rate of converges for the system. A 3-D plot of the mismatch as function of iteration is shown in Figure 6.26, with a clear convergence

148

in dark current towards 0 e⁻/sec. Figure 6.27 shows that the initial current across the pixel array has a standard deviation of 5.6E5 e⁻/sec, while the final standard deviation is 3.2E4 e⁻/sec, showing a 17 X reduction across the array.
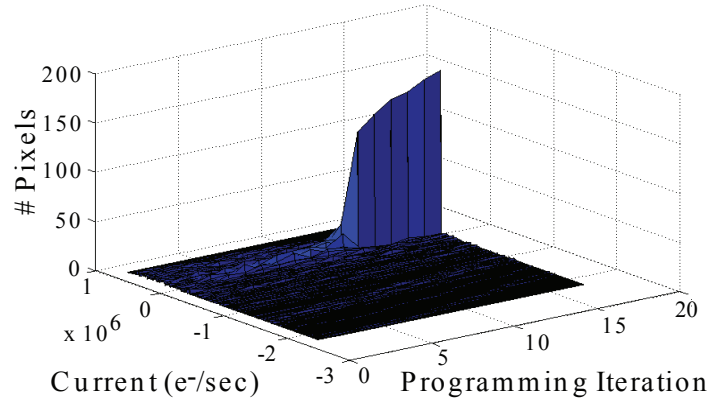
Figure 6.26: 3D graph of mismatch as a function of programming iteration for factory chip.
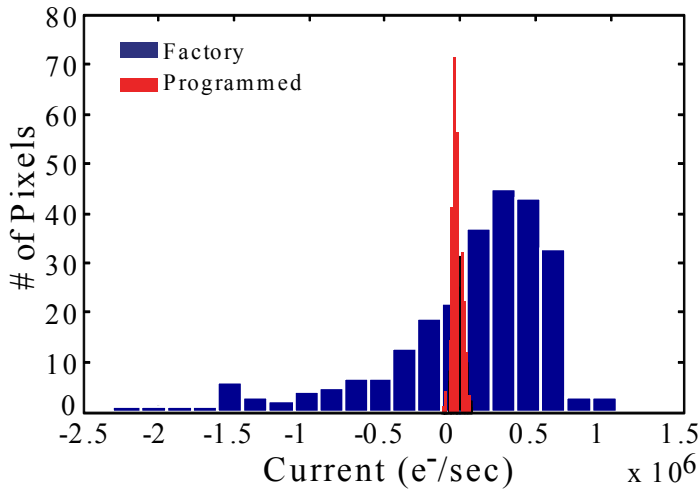
Figure 6.27: Histogram of factory chip mismatch and programmed mismatch.

While this demonstrates a large improvement over the foundry device, this comparison does not indicate that there is a 17 X improvement over a pixel array without mismatch compensation. This is because there is an initial charge on each

149

floating gate due to the ionic solutions and implantations used in the fabrication process. These residual charges would not be present on a comparable non-floating gate device. To obtain a more realistic measure of the improvement due to the floating gate mismatch compensation technique, the entire chip was exposed to UV light for two hours, which effectively removed any residual charge on the floating gate devices. After UV erasing, programming was enabled, with a V_{tun} of 7.8 V and a charge pump voltage supply of of 4.3 V. These lower voltages were chosen to achieve finer control for the tunneling and injection process. The dark current statistics were collected using a 5 second integration time. The UV-erased pixel array had a standard deviation of 8.3E3 e$^-$/sec which matches well with our simulation results. Again, programming was performed on the array, this time with a 5 second integration time and with more stringent boundary conditions. In this experiment, if the current was greater than 100 e$^-$/sec tunneling was performed, if the current was less than 100 e$^-$/sec injection was performed. After programming, dark current statistics of the array were measured with a resulting dark current standard deviation of 158 e$^-$/sec, corresponding to a 57 X improvement. The experimental results are marginally better than the simulation results because the tunneling and injection biases were reduced to achieve tighter bounds on the mismatch correction. The histograms of the UV-erased and programmed results are shown in Figure 6.28. A summary of the chip characteristics is provided in Table 6.5.

150
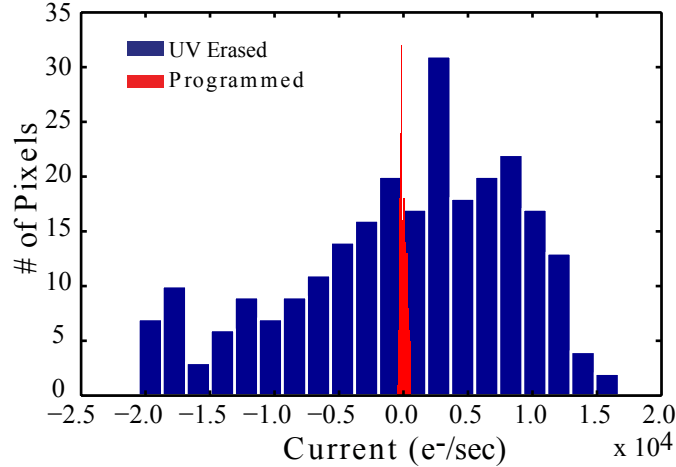
Figure 6.28: UV erased and re-programmed under tight constraints.

Table 6.4: Example Optimization Variables

q	1.6E-19 Coulombs
C_{int}	100 pF
I_p	0.41 photons/sec μm^2
I_d	0.027 photons/sec μm^2
C_{det}	89 aF/μm^2

6.10.1 Noise reduction UV vs Programming

The reduction in dark current across the array increases the overall dynamic range and reduces the fixed pattern noise that arises from spatially varying dark current. Thermal carrier generation in a junction is considered to be a random process with Poisson statistics where the variability in the dark current is proportional to the magnitude of the dark current. As a result of this decrease in dark current, there is a fundamental reduction in the noise associated with that dark current. Figure 6.29 shows the noise associated with the dark current for each pixel with UV erasing and mismatch compensation programming under tight constraints. There temporal noise associated with the dark current is reduced by 49% on average across they entire array.

151
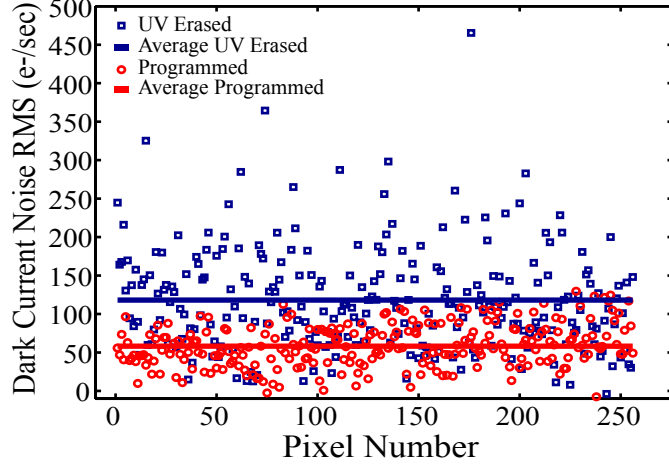
Figure 6.29: Resulting RMS noise associated with dark current for a UV erased and a re-programmed array under tight constraints.

6.11   Optimal Design

The previous discussion focused primarily on the reduction of dark current. In this section the optimal relationship of active area, integration capacitor, and amplifier noise is examined.

Recall that the SNR is:

$$SNR(t) = \frac{P_{signal}}{P_{noise}} = \frac{E[signal]^2}{std[Noise]^2} = \frac{\mu_{signal}^2}{\sigma_{noise}^2 = \sigma_{reset}^2 + \sigma_{readout}^2 + \sigma_{dark}^2 + \sigma_{photons}^2}$$

Assuming the system uses correlated double sampling or some other multi-sampling method, and that the dark current and photon arrival rates follow a Poisson distribution, the SNR(t) becomes:

$$SNR(t) = \frac{g_e^2 q^2 \eta^2 \lambda_{ph}^2 t^2}{g_e^2 q^2 \lambda_d t + \eta^2 g_e^2 q^2 \lambda_p t + g_v^2 \frac{kT}{C_{total}} + g_v^2 2\sigma_{readout}^2}$$

where η is the quantum efficiency of the pixel, λ_{ph} is the photon arrival rate, λ_d is the dark current generation rate, q is the electron charge, g_e is the electron gain, g_v is the voltage gain, k is Boltzmann constant, T is the temperature in Kelvin, and $\sigma_{readout}$ is the readout noise of the CTIA.

Further assumptions are made including C_{int} is fixed, while the photo-arrival rates, λ'_{ph}, and dark current generation rate, $lambda'_d$, are proportional to the active are of the pixel, additionally, the capacitance of the detector C'_{det} is also proportional to the active area of the pixel.

$$SNR(t) = \frac{\left(\frac{q}{C_{int}}\right)^2 \eta^2 A_d^2 q^2 \lambda'^2_{ph} t^2}{\left(\frac{q}{C_{int}}\right)^2 A_d q^2 \lambda'_d t + \left(\frac{q}{C_{int}}\right)^2 \eta^2 A_d q^2 \lambda'_{ph} t + \left(\frac{A_d C'_{det}}{C_{int}}\right)^2 2\sigma^2_{readout} + 2\sigma^2_{readout}}$$

Assuming we want to achieve an SNR of 1, within one second, we can choose our active area and solve using the quadratic formula.

$$A_d^2 \left[\left(\frac{q}{C_{int}}\right)^2 \eta^2 q^2 \lambda'^2_{ph} t^2 - 2\left(\frac{C'_{det}}{C_{int}}\right)^2 \sigma^2_{readout}\right] - A_d \left(\frac{q}{C_{int}}\right)^2 \left(q^2 \lambda'_d + \eta^2 q^2 \lambda'_{ph}\right) t - 2\sigma^2_{readout} = 0$$

$$A_d^2 \left(q^4 \eta^2 \lambda'^2_{ph} t^2 - 2C'^2_{det} \sigma^2_{readout}\right) - A_d q^4 \left(\lambda'_d + \eta^2 \lambda'_{ph}\right) t - 2C^2_{int} \sigma^2_{readout} = 0$$

Table 6.5: Summary of CTIA Pixel Array Characteristics

Array size	64 x 64 pixels μV
Readout noise	900 μV
Reset noise	4.7 mV
Supply voltage	4.1 V
Power consumption	2 μW
Dynamic range	68 dB
Maximum signal	3.3 V
Dark signal	0.5 mV/s rms
Conversion gain	5.3 μV/e$^-$
Pixel active area	3642 μm^2
Pixel Size	100 μm x 100 μm

Solving the quadratic formula we find.

$$A_d = \frac{q^4 \left(\lambda'_d + \eta^2 \lambda'_p \right) t + \sqrt{q^6 \left(\lambda'_d + \eta^2 \lambda'_p \right)^2 t^2 - 8 \left(q^4 \eta^2 \lambda'^2_p t^2 - 2C'^2_{det} \sigma^2_{readout} \right) C^2_{int} \sigma^2_{readout}}}{2 \left(q^4 \eta^2 \lambda'^2_p t^2 - 2C'^2_{det} \sigma^2_{readout} \right)}$$

Table 6.4 summarizes the design variable assumptions. Optimizing the active area based on these constraints yields an active area of 22,500 μm^2. If we allow our timing constraint to relax to one 5 sec, our optimal active area becomes 3642 μm^2, corresponding well with our fabricated system.

6.12   Summary of Results and Critical Analysis

This chapter presents an offset correction method intended to reduce the noise associated with thermally generated carriers in the reverse bias p-n junction of a capacitive trans-impedance amplifier based active pixel sensor. A metric was established using the difference between the output voltage during the reset phase, and the output voltage just after the start of the integration cycle. The metric was shown

to correlate well with the input-referred offset of the pixel, as well as secondary node in the CTIA amplifier to which mismatch compensation is applied. Mismatch compensation in this circuit is achieved through the injection or tunneling of electrons onto an electrically isolated gate of a PMOS transistor. The output metric was sequentially assessed and tunneling and injection circuits were used to achieve in-direct programming to raise or lower the charge stored on the isolated node accordingly. The offset correction method can reduce the input-referred offset by a factor of 10X, corresponding to a similar reduction in dark current across the chip.

While this method produces superior noise suppression to other CMOS sensors, it has several drawbacks. The photodetector junction must be held extremely close to 0 V reverse bias for the best noise suppression. To accomplish this, an amplifier is used, but the 0 V reverse bias is nearly outside the input operating range of the amp, so specific care must be taken in the design of the feedback amplifier. A second drawback is that the effectiveness of the CTIA is limited by its thermal sensitivity of the CTIA. If the environmental temperature changes, the biasing conditions of the circuit must change. Third, the CTIA makes the pixel larger than a standard three transistor pixel increasing the footprint. Fourth, the injection and tunneling structures used also increase the pixel footprint. In future designs, the injection and tunneling structures will be simplified to a more compact solution. Fifth, the sensor is very sensitive, so precautions must be taken to shield the device from environmental electromagnetic interference such as ionic variability in the test solutions, one such solution is to include a grounded layer of ITO on top of the pixel array. Despite these drawbacks the sensor significantly reduced dark current across the array. A future

iteration of this chip will be integrated with a microfluidic cell capture system with individual vials for simultaneous bioluminescence measurements.

A similar technique is currently being pursued to develop pixel-by-pixel detector optimization for CMOS based quantum-well infra-red detectors. There is a growing trend to incorporate multiple spectrally-specific detectors on a single imaging platform for infra-red imaging. These systems can achieve hyper-spectral sensitivity but required different biasing conditions based on the specific material junctions used. Current commercially available CMOS readout systems can at-most provide two inter-digitated biasing configurations. The work described in this chapter shows that independent pixel-by-pixel biasing can be achieved to obtain a highly optimally biased detector.

Chapter 7

Low Dark Current Pixel

7.1 Introduction

This chapter describes the theory of operation and presents experimental results for a CMOS pixel designed for high-speed low-light imaging applications. The pixel has been designed and fabricated in a commercially available three metal two poly 0.5μm CMOS process. The architecture actively reverse biases the photodiode near zero volts to achieve lower dark current than a standard three-transistor one photodiode pixel sensor, while increasing the front end gain and linearity. The dark current is reduced by approximately 75% at large reverse biases, while the gain is increased by the ratio of photodiode capacitance to integration node capacitance. In our test structure this corresponds to a 50X increase in gain.

7.2 Design and operation

Figure 7.1 shows the schematic of a low-dark current pixel along with a feedback amplifier proposed by Ji *et. al.* A large n^+-p_{sub} photoactive area of $1000\mu m^2$ is used so that the dark current is large enough to measure. This amplifier may be included in-pixel, or implemented at the chip level.

Transistor M_1 is the reset transistor. M_{sf} is a PMOS transistor for the source follower readout buffer. M_{rsel} is the row select switch which gives the pixel access to the column bus. All transistors in this pixel are $6\lambda/2\lambda$ (W/L), except M_2, which is $6\lambda/4\lambda$ (W/L). The increased length of M_2 helps to minimize the Early effect over the integration period and maintain a large V_{gs} at low light levels. Maintaining a large V_{gs} is important because practical implementations of the feedback amplifier which generates the gate voltage for transistor M_2 have a limited output swing.

Similar pixel structures have been reported. M_2 has also been used as a shutter to synchronize integration across a pixel array [152]. In [75], M_2 is used as a transfer gate, similar to the operation of a photogate pixel. Operation in this manner allows correlated double sampling. M_2 has also been used as a transfer gate during integration to achieve high conversion gain and good linearity [153].

This pixel has the same structure and therefore can be operated in any of the operational modes described above. However, none of these structures employ the transistor as an analog component. In this work M_2 is used as a common gate output buffer to the photodiode and bias the photodiode near zero volts to reduce dark current. Biasing the photodiode near zero volts will minimize all dark current related

artifacts.

The positive terminal of the feedback amplifier is biased near ground while the negative terminal of the photodiode is connected to the negative input of a feedback amplifier and the source of M_2. The negative terminal of the photodiode is pinned near zero bias by connecting the output of the amplifier to the gate of M2 in a negative feedback configuration.

The amplifier's design is determined by the dual requirements for low input and output common mode voltage. A threshold drop occurs from the gate to source of M2, so ultimately the ability to drive the negative terminal of the photodiode near zero bias is dictated by the amplifier input/output operating range. A p-type input single stage folded cascode structure is used in order to operate with common mode input near zero volts, and the folded cascode allows for the output swing to operate near zero volts to satisfy these requirements.
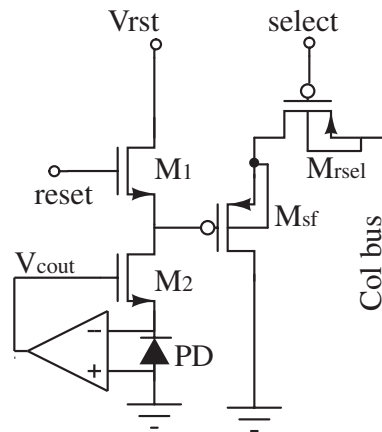
Figure 7.1: Four transistor pixel with one photodiode and feedback schematic [9].

Transistor M_2 has the additional benefit in that it decouples the integration

node from the photodiode node. The front end gain is inversely proportional to the capacitance of the integration node. By separating the photodiode node from the integration node, the integration capacitance is now due to the parasitic capacitances of M_1, M_2, and M_{sf} and the floating diffusion region. Higher front end gain improves the noise performance of the system. In addition, this capacitance does not scale with the photodiode area, so a larger active area will collect more photons but maintain the high front end gain.

7.2.1   Experimental Results

The two pixels were allowed to integrate over a two volt operating range, and record the results for 100 sample paths. The pixel was powered by a 4.5V battery pack consisting of three AA batteries in order to eliminate power supply fluctuations. From this data, the dark current front end gain and linearity of the sensor can be determined. The reset voltage was provided from an analog output of a data acquisition card (NI PCI-6281, M Series) and set to 3.5V. This voltage was chosen to ensure that the initial voltage upon reset remains within the operating range of the source follower output buffer.

Because dark current can only be measured indirectly by observing changes in the output voltage, a similar method to that of Fowler is used [97]. The main difference between our method and the method presented by Fowler is that instead of breaking the traces into equal sets of time, the traces were broken into equal increments of voltage (50 mV), and extract the corresponding time steps to estimate

the gain, dark current and linearity. In this case, this is a better method because it allows us to compare the dark current and gain around a particular reverse bias given a small variation about that bias.

The integrated voltage will increase approximately linearly as a function of time over short integration path segments. Because dark current is observed as a Poisson process, the phenomenon that the variance of the integrated voltage increases approximately linearly as a function of time is exploited. Therefore the slope of the mean signal and the slope of the variance are the critical parameters at each bias voltage.

The slope of the voltage in the dark can be described by:

$$Slope_{voltage} = \frac{\Delta V}{\Delta t} = \frac{g_{(Vrev\_bias)} I_{dk(Vrev\_bias)} \Delta t}{\Delta t} \tag{7.1}$$

where the gain $g_{(Vrev\_bias)}$ is in terms of V/e^- and $I_{dk(Vrev\_bias)}$ is in terms of e^-/s. The slope of the variance of the integrated voltage in the dark can be described by:

$$Slope_{variance} = E(\frac{(\Delta V)^2}{\Delta t}) = \frac{g^2_{(Vrev\_bias)} I_{dk(Vrev\_bias)} \Delta t}{\Delta t} \tag{7.2}$$

The dark current was estimated in number of electrons per second around a particular reverse bias across the photodiode by looking at the ratio between the slope of the average dark signal voltage squared to the slope of the variance.

$$I_{dk(V_{rev\_bias})} = \frac{Slope^2_{voltage}}{Slope_{variance}}$$

$$= \frac{(g_{(Vrev\_bias)}I_{dk(Vrev\_bias)})^2}{g^2_{(Vrev\_bias)}I_{dk(Vrev\_bias)}}$$
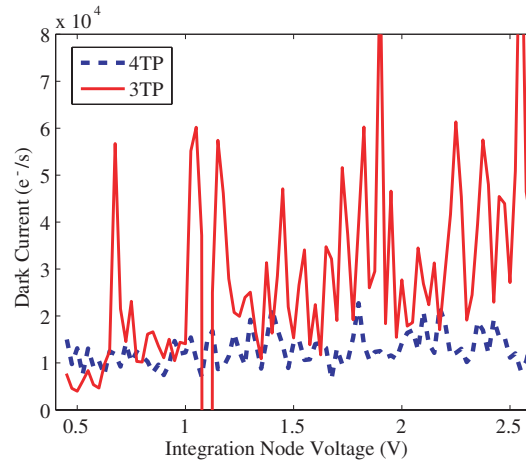
Figure 7.2: Dark current as a function of reverse bias for a standard three transistor pixel and low-dark current four transistor pixel. Shows up to 75% reduction in dark current [9].

The dark current as a function of reverse bias is depicted in Figure 7.2. The dark current estimates of the three transistor pixel show an upward trend as a function of voltage at the integration node, indicating the existence of signal dependent variations in the dark current. The dark current of the four transistor pixel is almost constant regardless of the integration node voltage, indicating that the dark current is no longer affected by signal dependent variations. At reverse biases larger than 2.5V, the active reverse biasing of the photodiode's junction to near zero volts has reduced the dark current by 75% (i.e from 4E4 to 1E4).

Similarly, the gain can be determined around a particular bias by looking at the ratio between the slope of the variance to the slope of the dark current voltage.

$$g_{(V_{rev\_bias})} = \frac{Slope_{variance}}{Slope_{voltage}} = \frac{g^2_{(Vrev\_bias)}I_{(Vrev\_bias)}}{g_{(Vrev\_bias)}I_{(Vrev\_bias)}} \qquad (7.3)$$
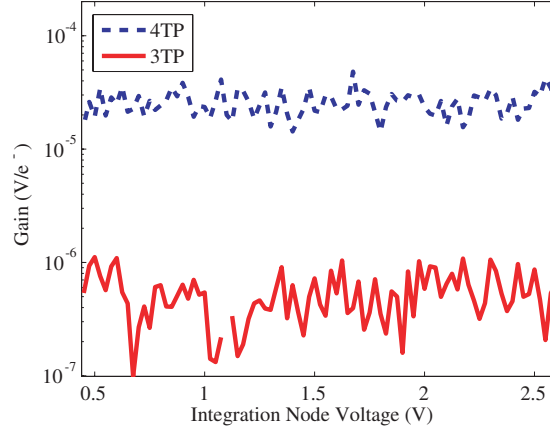
Figure 7.3: Front end gain of sensor as a function of reverse bias of a standard three transistor pixel and low-dark current four transistor pixel. Shows approximately a 50X increase in front end gain [9].

The gain as a function of reverse bias is depicted in Figure 7.3 for both a standard three transistor pixel and the new four transistor pixel. The average gain of the new four transistor pixel is $2.58E - 5$ V/e^-. This corresponds to an integration node capacitance of 6.2 fF, as compared to 7.2pF in layout. The average gain of the three transistor pixel is $5.35E - 7$ V/e^-. This corresponds to an average integration node capacitance of 300 fF, which compares to 343.5 fF. These values accurately reflect the equivalent capacitance predicted by layout.

The linearity was quantified by examining how the slope of the voltage at the integration node changes as a function of reverse bias. In this work nonlinearity of

the sensor is defined as the slope of the voltage (mV/s) subtracted from the ideal gain divided by the ideal slope 7.4. The ideal slope is average slope of the voltage over the operating range is 311 mV/s for the 4TP and 12.5 mV/s for the 3TP.

$$Nonlinearity = \frac{Slope_{voltage} - Slope_{ideal}}{Slope_{ideal}} * 100 \qquad (7.4)$$

Figure 7.4 shows this nonlinearity, the percent deviation from the ideal slope, as a function of reverse bias. The 4TP pixel has a much higher linearity than the 3TP pixel. Over the range of 0.4V to 2.6V the standard deviation of this nonlinearity is 9.7% for the 4TP and is 47.6% for the 3TP.
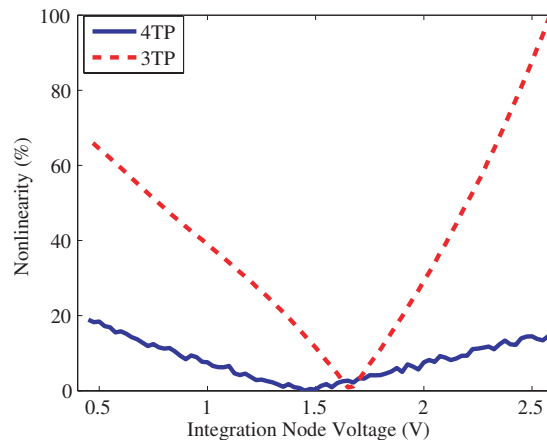
Figure 7.4: Nonlinearity of sensor as a function of reverse bias of a standard three transistor pixel and low-dark current four transistor pixel. Shows approximately a 5X improvement in linearity [9].

7.2.2 Radiation Detection Experimental Results

Active pixel sensor (APS) arrays have been driven by the digital camera industry. Typical APS arrays feature nine million pixels. Some APS arrays have frame

164

rates as high as 10,000/second. APS arrays represent a potential solution to high-density low-cost x-ray imaging. X-rays can be directly absorbed in the pixel, or can indirectly convert scintillator light to electrical current. Noise reduction improves energy resolution, and reduces patient dose [154]. Minimizing noise remains a challenge in CMOS x-ray imaging [155].

A 4.5V Vdd source was used to power the pixel and Vcom was set to ground. A standard unity-gain source follower buffer was simulated to model the readout path and downstream noise. All transistor sizes within the pixel are the minimum feature size for a standard 0.5 μm CMOS process. Simulation results were collected using the standard pixel as well as a low-noise pixel. In these experiments Vcom was set to 0V, thereby to minimizing the thermally generated dark charges generated in the n+/psub junction used to collect ionized electrons from the radiation. Similarly, the standard 3TAPS, was simulated with 4.5 V Vdd and a standard source follower readout buffer. However, without the addition of transistor M4 and the feedback amplifier, the n+/psub suffers from excess thermally generated carriers and reduced front end gain. The integration node is equivalent to the detector node, so the detector starts off with a high reverse bias leading to excess dark current. Here we model the dark current as a current an order of magnitude larger than the LNAPS dark current. In the experiments, five second integration times were used to demonstrate SNR enhancement of low-noise pixel. A 4.5 V battery was used as a power supply for each device under test. Both detectors were exposed to simulated 75 keV x-rays for a 12 second burst. A laptop with custom Labview program was used to record from each of the pixels at a sampling rate of 10 Hz and screen-captures were used to save

the data.

Results are shown in Fig. 7.5 and Fig. 7.5.
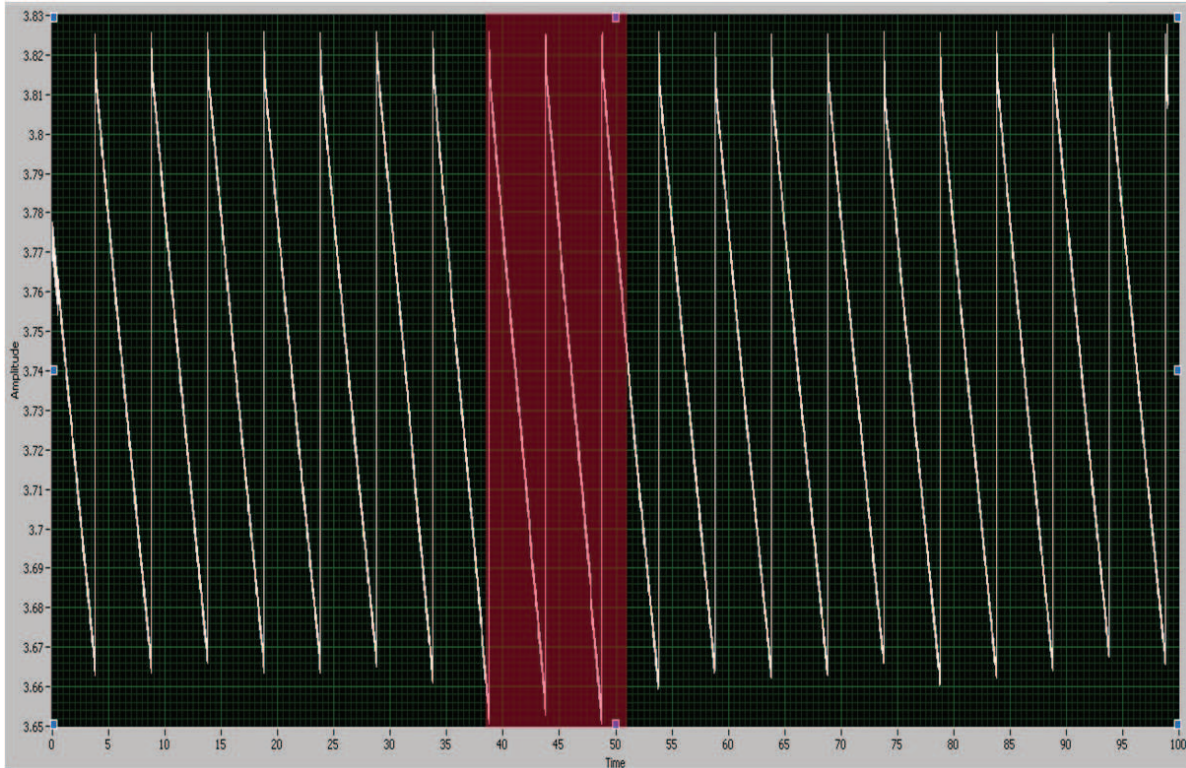
Figure 7.5: Standard 3TAPS experiment: 75 keV X-ray dose applied between times 39-51s (highlighted in red) [9].

Comparison of standard and low-noise APS experimental results showed that clamping the photodiode voltage near zero reduced thermal and field assisted dark current generation, leading to higher SNR. Experimentally, we observed a ten-fold increase in overall contrast-to-noise ratio (Fig. 7.7).

We observed that the use of a feedback loop significantly improved on-chip APS radiation detection. We expect similar results for indirect radiation detection (i.e., scintillators on APS array). Potential applications for the use of low-noise high-density APS arrays include low-dose x-ray CT scanners [155] , Compton gamma

166
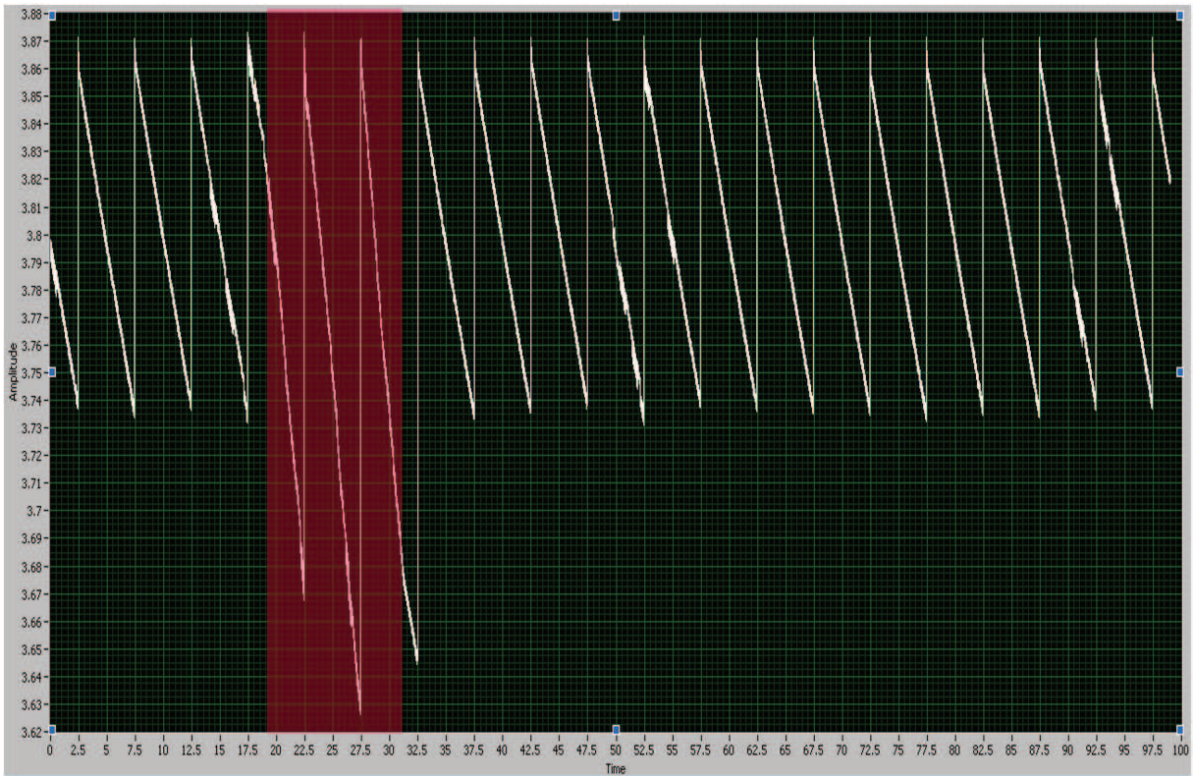
Figure 7.6: LNAPS experiment 75 keV X-ray applied between times 18-30 s (highlighted in red) [9].
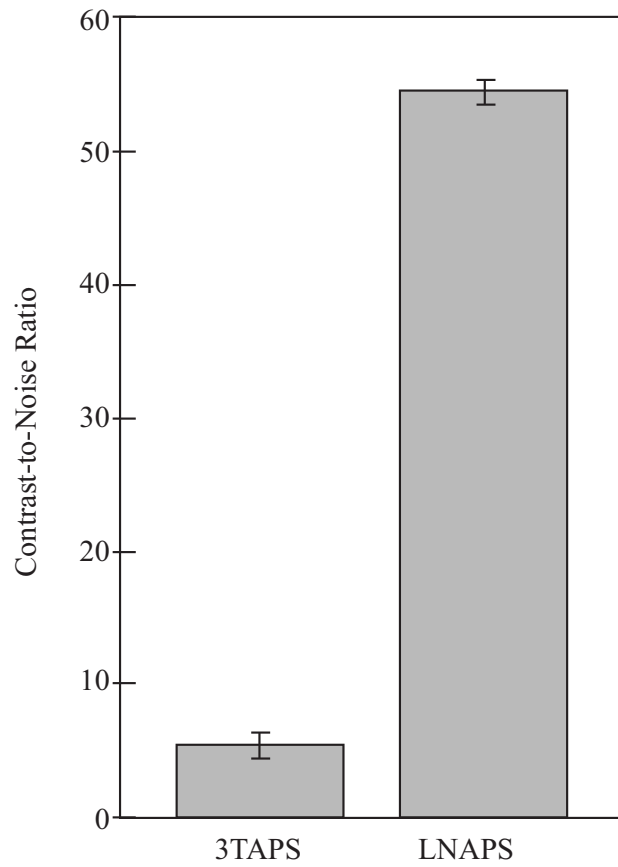
Figure 7.7: Contrast-to-noise ratios for standard 3TAPS (left) and LNAPS elements (right) [9].

cameras with low data-rate requirements [156], and implantable optical microscopes, compact gamma imagers for surgical applications [157]. Modified APS arrays improve CNR for radiation detection. Compact design of LNAPS enables high-density arrays for high-resolution gamma cameras, CT scanners [158]. High gain of LNAPS enables fast timing resolution.

7.3 Summary of Results and Critical Analysis

The suppression of dark current and dark current artifacts by actively biasing the photodiode of an active pixel sensor to zero volts has been experimentally demonstrated. This increases the signal to noise ratio, while improving both the front end gain and linearity of the sensor. The dark current in the new four transistor pixel was reduced by 75% at high reverse biases compared to that of a standard three transistor pixel of equal dimensions. In addition, the gain of the four transistor pixel was two orders of magnitude larger than that of the three transistor pixel because the integration node is decoupled from the photodiode node. While in practice the active area of the photodiode would be smaller than $1000\mu^2 m$, the decoupling will maintain a high gain regardless of the active area size.

A number of problems with the current design became apparent during testing of this device. When implementing this pixel in an array format, a sample pixel sets the M_2 gate voltage across the array a problem arises. For a specific pixel, the illumination will be different than the biasing pixel and will vary in time. In this configuration, the gate voltage M_2 can be considered fixed with reference to the

background illumination level, but does not capture the specific details of the scene. When scene dependent illumination changes, the photocurrent in each pixel changes. In equilibrium the photocurrent and the current through M_2 must be equal. The only way to change the current through M_2 is to change the V_{gs} of M_2 by changing the source voltage (the reverse bias of the photodiode). This voltage rises exponentially toward the equilibrium point regardless of the incident illumination. This is due to the negative feedback nature of M_2. However, when the photocurrent increases the photodiode voltage must decrease to reach equilibrium. This voltage decrease can only happen as a result of photocurrent removing charges from the integration node. The voltage decrease is occurs linearly with time at a rate proportional to the illumination. Because the capacitance at the photodiode node is not equal to that at the integration node, the change in photodiode voltage results in both temporally and illumination dependent sensor nonlinearity.

Another problem with the array format configuration of this pixel is in the ability of the feedback amplifier to drive transistor M_2 of each pixel in the array. The feedback amplifier must be able to drive a very low voltage i.e. less than 0.7 V and a very large capacitance. There is a small drain to gate capacitance of each M_2 that couples the integration node of each pixel to the output node of the feedback amplifier. While each pixel contributes a coupling capacitance, the overall array capacitance may be non-negligible. If used in a frame capture format, or other format whereby many pixels are reset at the same time, the integration node voltage rises quickly pulling up on the output voltage of the amplifier and the gate of M_2. If the gate of M_2 is temporarily pulled high, the photodiode voltage also increases

rapidly as described above. Unfortunately, M_2 cannot provide the necessary negative feedback in this configuration to reverse bias of the photodiode. As a result, when the reset transistor is turned on both the integration node and the photodiode node quickly increase. The photodiode node voltage increases well beyond its equilibrium point corresponding to the incident illumination. As mentioned before, the only way to discharge the photodiode node is by leakage current and photo-generated current. This non-equilibrium condition just after reset causes significant integration nonlinearity in the device.

A similar problem was discovered while testing a single pixel with integrated feedback. In the single pixel feedback configuration, the photodiode is biased to V_{dbias} which near zero volts, not at zero volts. The voltage at the integration node decreases towards V_{dbias}, and eventually passes V_{dbias} and saturates at 0 V. The negative input terminal of the amplifier drops below the positive input terminal of the amplifier. As a result the feedback amplifier raises the gate voltage of M_2 in an attempt to compensate for the input conditions. While this pixel design presents a desirable noise-footprint trade-offs, future designs must incorporated image lag compensation at the photodiode node.

Chapter 8

Integration Time Optimization for Integrating Photosensors

8.1 Introduction

Scientific imaging sensors attempt to minimize noise and, hence, maximize the signal to noise ratio (SNR) to produce optimal image quality. While this works well in a static scene, for time-dependent data, such as fluorescence measurements, the experimental strategy shifts to "How much information can we retrieve during an experiment?" The answer to this question is related to the fundamental and quantitative bound known as the information capacity of the system. In general, this depends on several factors including the power of the light emitted by the fluorescent probe as well as, the reset noise, shot noise, and integration time of the sensor.

For constant illumination (implying an unchanging scene), increasing integration time implies higher SNR; thus, the amount of information during an experi-

ment is maximized for increased integration times. Previously reported sensor arrays that maximize dynamic range through integration time control have been proposed [15, 16]. However, for time varying illumination (such as a moving image or during photo-bleaching of a fluorophore), increased integration time obscures information about the changes while a decreased integration time results in a poor SNR. There is, therefore, an inherent trade-off between the fidelity of an image and the bandwidth.

8.2 Information Capacity and System Model

Information capacity is one way to examine the inherent trade-off between fidelity and bandwidth of a sensor. The sensor can be considered a communication channel where the input signal is the incident illumination, and the output is an electronic signal. The mutual information [159] (a measure of the dependency of the output Y on the input X) is determined by the joint distribution and is defined by Equation 8.1:

$$I\left(X;Y\right) = \sum_{x,y} p\left(x,y\right) \log_2 \frac{p\left(x,y\right)}{p\left(x\right)p\left(y\right)} \tag{8.1}$$

where, I(X;Y) is the mutual information, p(x,y) is the joint probability distribution between random variables X and Y, and p(x) and p(y) are the marginal distributions of random variables X and Y. Information rate is then the information per sample times the sample generation rate defined in Equation 8.2:

$$R = f_s I\left(X;Y\right) \tag{8.2}$$

where f_s is the number of samples per second.

The maximum information rate, or capacity, is a fundamental and quantitative bound on the ability of a physical system to communicate information [159]. Assuming the sensor is a Gaussian channel (a communication channel with additive Gaussian noise,) the capacity (C) of that channel under an average power constraint is determined by Equation 8.3:

$$C = \Delta f \log_2 \left(1 + \frac{S}{N} \right) \tag{8.3}$$

where S is the average signal power, N is the average noise power and Δf is the bandwidth.

While the most common constraint for a channel is the average power constraint, another formulation more suited towards image sensors, is a peak average signal power constraint limited dynamic range in the channel. This is a natural constraint because integrating pixels have an upper bound in which the signal becomes saturated and therefore of no further practical use. It has been shown that the capacity under a peak signal power constraint is [159]

$$C \leq \Delta f \log_2 \left(1 + \frac{2}{\pi e} \frac{S_{peak}}{N} \right) \tag{8.4}$$

for a large enough SNR. If the samples are independent and uniformly distributed between $-\sqrt{S_{peak}}$ and $\sqrt{S_{peak}}$ then this capacity can be achieved. Since the sensor output is constrained in the range from 0 to V volts the capacity [160] can be found to be:

$$C \leq f_p \log_2 \left(1 + \frac{6}{\pi e} DR \right) \qquad (8.5)$$

where

$$DR = \frac{V^2}{12N} = \frac{S}{N} \qquad (8.6)$$

is the dynamic range defined as the ratio of the peak signal power to the average noise. For a static scene with one observation, maximizing the SNR maximizes the amount of information obtained by a sensor about a source signal.

8.3   Synchronous Sensors

8.3.1   Optimization Control Loop

Rather than maximizing the information obtained in one observation, this work attempts to optimize the fidelity bandwidth trade-off by maximizing the information rate. This method maximizes the total information over a given time interval which can be subdivided into an arbitrary number of observations. This is a more practical paradigm for measurements of fluorescence since the reaction time is an important element of the experiment due to effects such as photo-bleaching.

The maximum information rate is derived as a function of illumination and integration time and used to determine the optimal integration time for efficient transduction. With this result the detector's optimal integration time can be determined provided the previous integration time and illumination level are known.

Consider a model to determine the maximum information transmission where
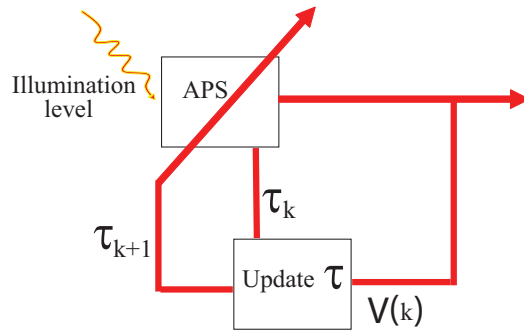
Figure 8.1: Integration time control loop of random access pixel [10].

the input to the detector is the illumination level. The detector transduces the illumination level to produce a voltage, and for a known integration time the voltage corresponds to a unique incident illumination. The information rate can be determined for every integration time and for a range of illumination levels. The maximum information rate is the capacity and occurs at the optimal integration time. Thus, for a given illumination level, this result determines the best integration time. This can be implemented in a control loop (Figure 8.1) where the integration time is optimized for any incident illumination. In this work, the control loop has been implemented as part of the off-chip data acquisition loop rather than as an integrated loop on-chip system.

In a practical sense this means that for any particular experimental scenario (for example, a fluorophore with a particular emission intensity and photo-bleaching effect) we can vary the integration time in the most efficient manner, given the specific characteristics of the detector.

Figure 8.2: Differential active pixel sensor [10].

8.3.2 Noise Models and Information Rate for a Charge Mode Pixel.

The information rate is limited by the noise of the detector. The form of the noise sources differ depending on whether the detector is operated in continuous or integration mode. In this work a differential charge mode pixel (Figure 8.2) was considered [10]. Noise sources considered in this work include reset noise, readout noise, and shot noise. The noise associated with resetting the pixel is:

$$\overline{V^2}_{n_{rst}} = \frac{kT}{C_{out}} \tag{8.7}$$

where k is Boltzmann's constant, T is the temperature, and C_{out} is the capacitance at the integrating node. There is also a noise due to the photocurrent in the diode

177

from the photon shot noise process, which is given:

$$\overline{V^2}_{n_{shot}}\left(t_{int}\right) = \frac{q\left(I_{ph} + I_B\right)}{C_{int}} t_{int} \tag{8.8}$$

where I_{ph} is the photocurrent, I_B is the dark current, C_{int} is the capacitance at the integrating node, and t_{int} is the integration time. The readout noise comprises all other noise sources in the readout chain. The readout noise of the pixel results from thermal and flicker noise in the source follower and readout buffer. The total readout noise results from is determined from the noise spectral density of each transistor [96]

$$S_{I_d} = 4\gamma kT g_m + \frac{K_f I_d}{C_{ox} W L f} \tag{8.9}$$

where $\gamma = 2/3$ or $1/3$ depending on mode of operation, K_f is a process dependent parameter, C_{ox} is the oxide capacitance per unit area and W and L are the geometric parameters of the MOSFET. Each noise source is then referred to the output, summed, and integrated over the bandwidth as:

$$\overline{V^2}_{n_{rdout}} = \int_{-\infty}^{\infty} S_{v_{out}}\left(f\right) df \tag{8.10}$$

Following the formulation described by Ji and Abshire [161], this leads to an information rate for the charge mode pixel:

$$I = \frac{1}{2t_{int}} \log_2\left[1 + \frac{6}{\pi e} \frac{\frac{\sigma_s^2 I_{ph}^2 t_{int}^2}{C_{out}^2}}{V^2_{n_{rst}} + V^2_{n_{shot}} + V^2_{n_{rdout}}}\right] \tag{8.11}$$

where σ_s^2 is the contrast power. This reflects the effect of the non-static nature of the

178
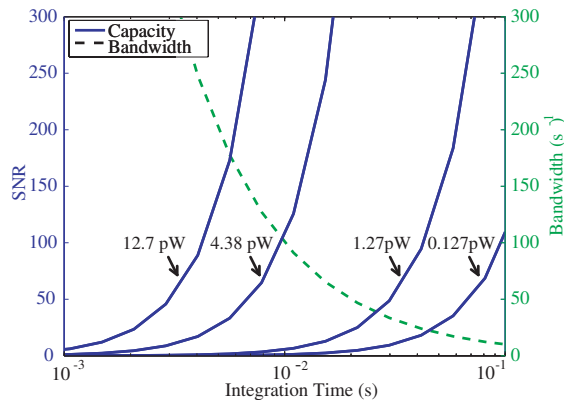
Figure 8.3: Signal-to-noise and bandwidth vs. integration time at 4 illumination intensities. The intensity is in terms incident photon power on active area of detector. Detector active area is 1000 μm^2 [10].

illumination source on the photocurrent and is taken to be 0.1.

Assuming the shot noise and readout noise are stationary and that the photocurrent follows Poisson statistics, the trivial solution to maximizing the SNR is to minimize the noise sources an integrate the signal for as long as possible. Practically the integration limit comes from the front-end gain and the power supply rails of the sensor as well as the stationary assumption of the source.

Figure 8.3 illustrates the trade-offs between image quality, and bandwidth at four illumination levels. The signal to noise ratio is related to the image quality and the inverse of the integration time is related to the bandwidth. For each illumination level, the signal to noise ratio increases with the integration time while the bandwidth decreases. It is possible to find a suitable integration time that accurately represents the light level while, at the same time, allowing the sensor to capture changes.
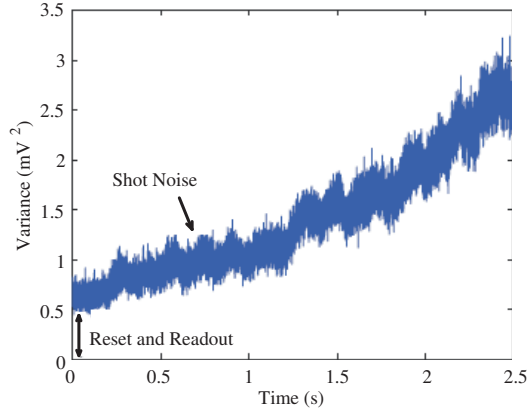
Figure 8.4: Differential sensor noise as a function of time. Reset noise and readout noise appear as an offset while photocurrent noise increases with time for an incident optical power of 12.7 pW [10].

8.3.3 Experimental Results

The reset and readout noise of the differential mode sensor in Figure 8.2 was experimentally determined under varying illumination conditions. This information was then used to determine the information rate and channel capacity for this sensor. The detector requires three control signals: select, reset, and i gate (isolation gate). During the reset cycle, the reset gate and isolation gate are switched off simultaneously. A monochromator combined with an integrating sphere is used as the illumination source and optical density filters are used to vary the illumination level. The readout, photon and reset noise are estimated using the method developed by Fowler *et al.* [97]. The reset and readout noise do not depend on the integration time and ,therefore, contributes a constant offset. The shot noise increases with integration time, as can be seen in Figure 8.4.

8.3.4 Information Rate vs Intensity

To calculate the information rate, an accurate estimate of the dark current must be obtained, as any DC offsets in the data will artificially increase the information rate. At each illumination level the integration time was swept from $t = 10e^{(n/3)}$ μs with n varying from 0 to 28. Roughly this corresponds to 10 μs - 100 ms. One thousand trials were averaged to estimate the output voltage contribution due to dark current. In addition, for each of four illumination levels, one thousand trials were taken to obtain adequate statistics.

Even with this large number of trials, a small variation in mean will create a huge change in information rate at small integration times, because the information rate is inversely proportional to the integration time. As such, a linear least squares fit of the average response as a function of time was used to obtain a well-behaved function of output voltage versus integration time. This well-behaved function was then used in equation 8.11 to produce the curves shown in Figure 8.5.

For the very low light trial, it was observed that the maximum integration time of 100 ms was not enough to achieve a reliable estimate of the information rate, because the peak of the information rate is approximately 0.1 s. For the lowest light level, trial the original data set was augmented with an extra set of integration times ranging from 0.1 s to 10 s with 200 trials. Overall, the data shows the same trends as the theoretical curves. The results imply that integration time is a variable that directly affects the information rate of an imaging system. Figure 8.5 shows low information rates are obtained for very slow and very long integration times,
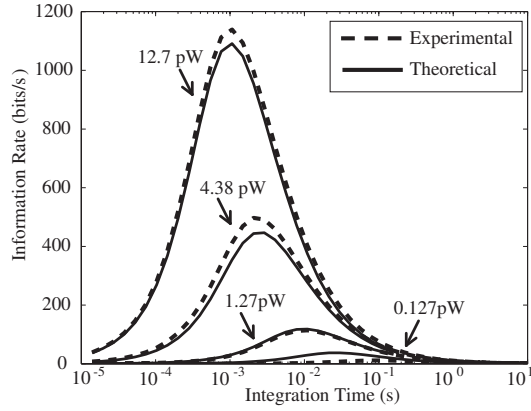
Figure 8.5: Information rate vs. integration time for different illumination levels [10].

with the maximum information rate somewhere between the two extremes. At high illumination levels, the information rate increases as $\frac{1}{\tau_{int}} \log \alpha I_{ph}$, and at low levels, it is proportional to the photocurrent divided by the integration time.

8.3.5 Channel Capacity

The maximization of the information rate yields the channel capacity of the detector. An interpolation of the experimental results can be used to estimate integration times that achieve the maximum information rate. Figure 8.6 shows the capacity and the required integration time for each of the illumination levels. Higher illumination levels yield larger capacities but with shorter optimal integration times.
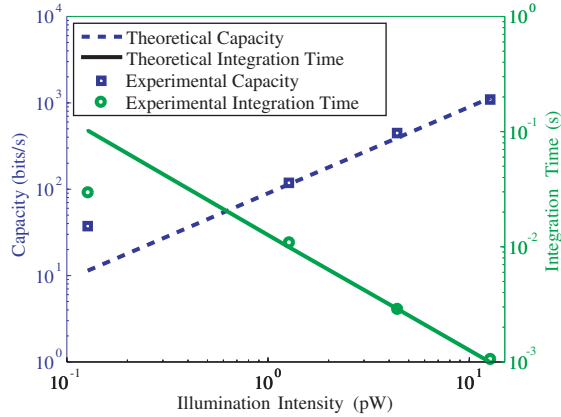
Figure 8.6: Integration time and capacity vs illumination [10].

8.3.6 Bit Energy

An alternative optimization is to maximize the bit energy of each sample. In this optimization, rather than maximizing the capacity of the system, the information rate per power is maximized. In general, this optimization shifts the information rate curves from Figure 8.7 depending on the amount of static power consumption. All circuits have some static power consumption. If there is no dynamic power consumption, i.e. power consumption is constant regardless of system throughput, the bit energy curves are identical in shape with respect to the information rate curves of Figure 8.5 scaled in magnitude depending on the static power consumption. If, however, there is dynamic power consumption, these information rates not only scale in magnitude, but also shift with respect to the optimal integration time. The resulting shift in the curves is always towards higher integration times; however, it is the ratio of dynamic power consumption to static power consumption (γ) that dictates the amount of shift.
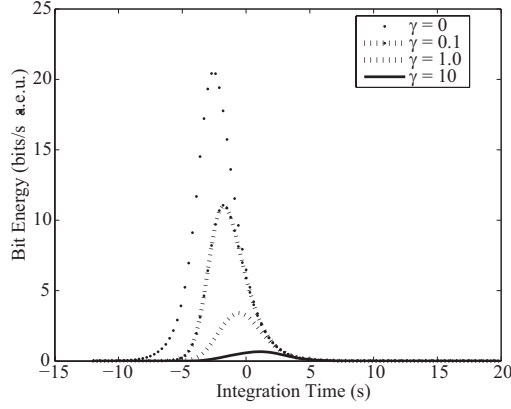
Figure 8.7: Bit energy (Bits/sec · arbitrary energy unit) vs. time (seconds) as a function of γ (static power to dynamic power consumption).

8.3.7 Extensions to Array Architecture

A similar optimization can be performed for an array of sensors. In the case of multiple detectors in an array format, it is assumed that each pixel/detector provides an independent measurement of interest. In this case the objective function we wish to maximize is the sum of the total information available and is described by:

$$I_{system} = \sum_{k=1}^{K} I = \sum_{k=1}^{K} \frac{1}{t_{int\_k} + t_{rst}} \log_2 \left[1 + \frac{6}{\pi e} \frac{\frac{\sigma_s^2 I_{ph\_k}^2 t_{int\_k}^2}{C_{out}^2}}{V_{n_{rst\_k}}^2 + V_{n_{shot\_k}}^2 + V_{n_{rdout\_k}}^2} \right] \quad (8.12)$$

where k is the kth pixel and K is the total number of pixels in the array. The trivial solution is to choose an optimal integration time for each pixel; however, each pixel can only be accessed in a serial manner; therefore, there is a constraint on the integration time of the pixels. This constraint can be written as:

$$\sum_{k=1}^{K} \frac{t_{rst}}{t_{int\_k}} < 1 \quad (8.13)$$

184
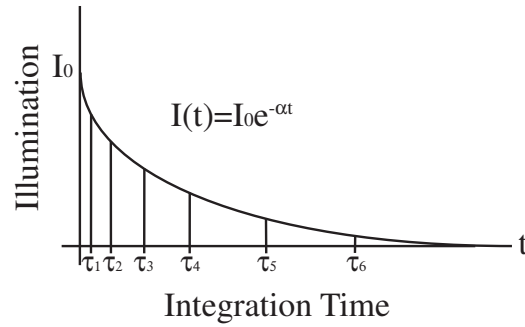
Figure 8.8: Example of integration time vs. intensity for photo-bleaching effect.

This constraint accounts for the non-zero read and reset time associated with sampling each pixel, and therefore, the total number of pixel reads cannot exceed $1/t_{rst}$. This set of equations can be solved by any non-linear optimization algorithm.

The analysis presented only holds for stationary signals, and under real conditions, the stationary assumption is not valid. However, neglecting photo-bleaching, the assumption can be made such that during any particular measurement, the illumination level is relatively constant. This assumption holds under biological conditions such as cell respiration.

Considering an example of photo-bleaching of fluorescence a time-varying input. Photo-bleaching refers to the decreased illumination (due to light exposure) over time of a fluorophore. The best way to achieve maximum information transmission for the detector is to start with short integration times that become longer. It is possible to take into account the prior knowledge of the system, such as the effect of photo-bleaching, to design an optimal sampling scheme for a particular experiment.

Figure 8.8 shows an example of how the optimal integration time might vary in response to a fluorescent probe with a photo-bleaching effect. The initial integration

time is set based on a best guess that will give an output above the noise floor but below saturation. After the first integration cycle, the approximate photocurrent and thus illumination is calculated. This measurement of the photocurrent will be noisy and therefore the estimate of the integration time will be noisy. The estimate of the illumination and corresponding optimal integration time will be updated with every measurement cycle. Observation based filters such as a Kalman filter can be used to tighten this bound.

8.4   Asynchronous Sensors

Asynchronous images sensors are integrating sensors, but rather than have a specified integration time, they have a specified threshold voltage. Once the sum of the photo-generate and dark current reach the specified threshold, a digital amplitude analog time event is generated. The inter-event time encodes the light stimulus with an SNR specified in Chapter 3. The general information rate formula can be applied to these pulse-encoded systems resulting in:

$$IR = \frac{1}{\frac{V_{thr}C_{int}}{q\lambda_{total}} + t_{readout}} ln \left(1 + \frac{6}{\pi e} \frac{\left(V_{thr}C_{int}\frac{q\lambda_{ph}}{(q\lambda_{tot})^2} \right)^2}{\sigma^2_{readout} + \frac{\frac{kTC_{int}}{q} + \frac{V_{thr}C_{int}}{q\lambda_{tot}}}{\lambda^2_{tot}}} \right) \tag{8.14}$$

where, V_{thr} is the event threshold in volts, C_{int} is the integration capacitance, q is the electron charge k is Boltzmann's constant, T is the temperature in Kelvin, λ_{ph} is the electron generation rate due to photons, λ_{tot} is the total dark current and photocurrent generation rate, $t_{readout}$ is the average readout time, and $\sigma_{readout}$ is the
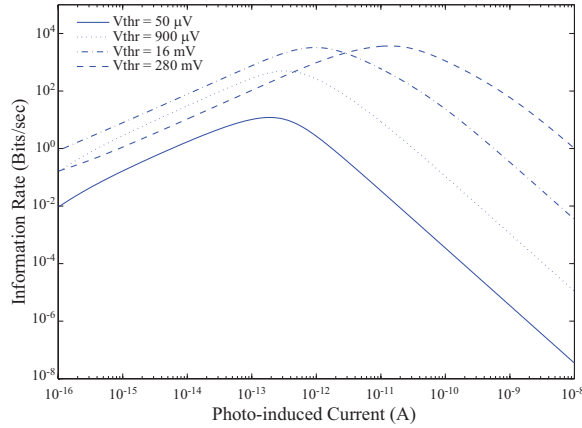
Figure 8.9: Bit energy (Bits/sec · arbitrary energy unit) vs. Photo-generated current (A) for several event threshold voltages.

timing jitter along the readout path. For an array of sensors, the timing jitter will become a function of the number of pixels and event time.

A sample sensor was simulated with the following characteristics. The integration capacitance C_{int} was 30 fF, the dark current was 0.1 pA, a readout time of 10 μs with associated timing variance of .1 μs. Both the threshold voltage V_{thr} and the input illumination intensity were swept parameters. The threshold voltage was swept from approximately 50 μV to 280mV. The illumination intensity was swept from 0.1 fA to 10 nA, from the dark current noise floor to well beyond the expected input intensity range for most applications. The results of the information rate simulation are shown in Figure 8.9.

The results indicate that for each specified threshold voltage, the achievable information rate initially increases with intensity, reaches a unique maximum, and then decreases. The rise is due to an increase in sampling rate and SNR with an increase in intensity; however, the fall-off occurs because timing jitter along the readout path becomes the dominant source of noise for high-intensity short-inter-arrival time
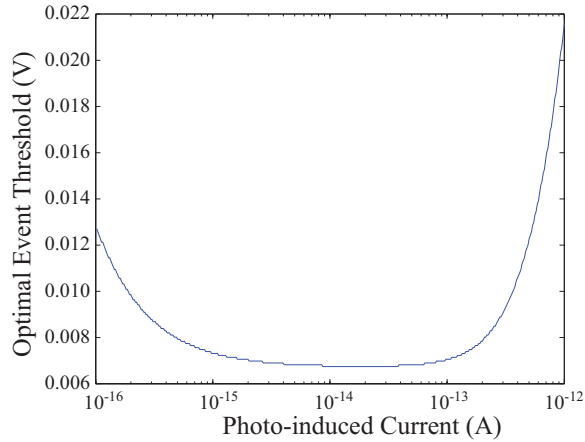
Figure 8.10: Threshold voltage required to maximize information rate as a function of illumination intensity.

events. An interesting feature of these graphs is that for low intensities, i.e. within four orders of magnitude of the dark current, one of the threshold voltages $V_{thr} = 16$ mV achieves a higher SNR than any other threshold voltage. To examine the nature of this relationship, the simulation was performed over four orders of magnitude, from 0.1 fA to 1 pA. The maximum information rate at each illumination intensity was found along with the associated threshold voltage. Figure 8.10 shows the resulting optimal event thresholds as a function of illumination intensity.

The results indicate that the optimal threshold voltage is within 6-20 mV each other for each illumination intensity over four orders of magnitude and within 6-8 mV over two orders of magnitude. In practice, it is difficult to design an AER sensor with a precise 10 mV threshold, but this work can provide guidance for the design of next-generation systems.

A similar analysis can be performed for arrays of such sensors. In this case the primary difference between the single sensor and array formulation is that the mean readout time and readout timing jitter become a function of illumination conditions

and threshold voltage to take into account data collision, queuing and arbitration. AER arrays are already well known for efficient bandwidth allocation and other attractive properties discussed in 3. Integrate-and-fire AER arrays, under sparse data constraints, are optimal not only in a bandwidth allocation and throughput sense, but also in an optical transduction sense.

8.5   Summary of Results and Critical Analysis

In this chapter the information rate and information capacity were used as metrics for optimizing the performance of integration based image sensors. Experimentally extracted reset, readout and photocurrent noise of a differential active pixel sensor were used to maximize its information rate over a range of illuminations. The information rate is maximum at points between very short integration times high temporal fidelity and very long integration times producing high SNR. The resulting optimal integration time for each incident illumination shifts to smaller integration times as the illumination level increases. An alternative optimization is to maximize the information rate per watt, i.e. maximize the bit energy. In resource constrained environments, power consumption is a significant factor and maximizing the bit energy effectively maximizes the device efficiency. Maximizing the bit energy depends not only on the illumination conditions, but the power consumption of the system. The ratio of static power to dynamic power was used as a metric to examine the trends in the bit energy maximization. These results are important not only for determining the performance trade-offs using this system, but invariably the optimization itself

will require power consumption, and therefore, it can be taken into account using these trends. This analysis extends directly to sensor arrays where a single controller data acquisition system and communication bus is shared among all pixels. In this case, the array can be treated as a sum of independent pixels subject to a constraint on the total number of samples possible per second. This is a well known optimization and can be determined though the steepest decent method, the simplex method, or any other appropriate algorithms.

One of the key results of the integration time optimization analysis was that for a small range of illumination conditions, the optimal integration time was inversely proportional to the illumination intensity, which implies that the optimal condition is to integrate the system to a fixed voltage. This fixed integration voltage result is exactly what an integrate-and-fire asynchronous sensor achieves. The second part of this chapter examines a simulation of the information rate of an integrate-and-fire sensor and maximizes the information rate as a function of illumination intensity as well as the event threshold. Typical parameters for an integrate and fire pixel were used including readout time, timing jitter, reset noise, and dark current. The threshold voltage of the integrate-and-fire pixels was swept from 5 μV to 5 V, and the information rate was calculated for each incident illumination. The results confirm that an optimal and nearly static threshold voltage exists over a range of illumination intensities. The implication of this result is that integrate-and-fire sensors can be designed and operated near capacity over a range of illuminations. Additionally, since many integrate and fire pixels use relatively little static power, they exhibit a low static- to dynamic-power consumption ratio, which from the previous analysis

190

maximizes the bit energy without having to re-calculate the optimal conditions as in the integration time optimization case. AER arrays are well known for efficient bandwidth allocation [89]. These results show that integrate-and-fire AER arrays are not only optimal in a bandwidth allocation and throughput sense, but may also be in an optical transduction sense. While the optimal threshold was found to be too small for a practical system built in a 0.5 μm technology, it demonstrates that integrate-and-fire sensors present an attractive solution in advanced technologies.

Chapter 9

Conclusion

This work described the development of two core lab-on-a-chip imaging functions, object detection and optical measurements as well as radiation detection. Contact imaging was evaluated as an imaging paradigm for microsystems. Contact imaging, unlike conventional optical imaging, avoids the use of intermediate optical components such as lenses and the sample of interest is brought in direct contact with the image sensor surface. Contact imaging is favorable because it increase the overall photon collection efficiency as well as reduces system cost, weight and complexity. As a result of this configuration, the contrast of the scene is primarily dictated by pixel size and the optical properties of the sample of interest. A simulation was performed using the ray tracing program LightTools where a small circular object was placed between a light source and an image sensor array. The arrival of each photon was binned into each effective pixel and the resulting image was analyzed to determine the contrast of the scene. An object was classified as detectable if the contrast metric value was above 1. The simulations were performed for various object shapes and op-

tical densities. In all cases examined, an acceptable contrast was obtained beyond 100 μm indicating that the contact imaging paradigm works well in microfluidic systems where the maximum feature dimension is on the order of 100 μm.

An asynchronous imaging system was designed for the application of particle detection. The 22 x 22 pixel integrate and fire based sensor uses an arbitrated readout design and incorporates the necessary circuitry to enable active reset. Active reset is a reset method that uses a feedback amplifier to minimize reset noise at the front end of an integration based pixel. The signal to noise ratio of an integration based AER system was analyzed for inter-arrival time encoding. Unfortunately the active reset circuit was unable to sufficiently suppress reset noise. The array was tested in a bench-top setting to determine the intensity/bandwidth/noise relationships of the device as well as compare the bandwidth and computational load requirements of a typical object detection task against a standard frame-based sensor. The

A differential image sensor was design and fully characterized. Although differential sensors inherently increase the fundamental noise floor of the device, they provide excellent environmental noise suppression. The resulting sensor provided 10X noise suppression while modestly increasing the fundamental noise floor. The sensor was then integrated into a handheld fluorescence detection system. Several biologically relevant experiments were preformed detecting the biotoxicity of Poly(amidoamine) dendrimers, the metabolic cycle of yeast, and a live dead assay for bovine aortic smooth muscle cells.

A low-noise bioluminescence detector array was designed, tested and fabricated. Dark current represents one of the primary challenges in detecting bioluminescence

signals because the magnitude of light created by bioluminescence is incredibly small, and cannot be intensified through external means. The approach taken to minimize the dark current was to clamp the photo-junction of the detector to zero reverse bias, which is known to generate the highest SNR. The effectiveness of this pixel was demonstrated using a genetically engineered CANARY cell exposed to a stimulant. While this technique works well for single devices, arrays of such devices suffer from fabrication mismatch, preventing multiple simultaneous assays on a single device. A floating gate mismatch compensation circuit was introduce to reduce the pixel-to-pixel variability of the biasing structures to ensure that each device provides the highest SNR obtainable. Using the floating gate mismatch compensation method, the standard deviation in pixel-to-pixel dark current was reduced by approximately 10 X.

Finally, integration based sensors were analyzed in the context of an electronic communication channel. The information rate and information capacity of the differential sensor from above were derived and experimentally verified. The results indicate that the integration time of the sensor can be controlled to maximize the capacity of the sensor, which may be useful in the context of fluorescence imaging. Additionally, the results show that over a limited range of illumination intensities the optimal integration time is inversely proportional to illumination intensity. This means that it is optimal to integrate to a fixed voltage. As described above integrate and fire pixels provide this exact function automatically. The SNR derived above was included in an information rate derivation for an integrate and fire device. A simulation was performed using these equations and the results show that there is a near

optimal threshold voltage over several orders of illumination intensity of magnitude a representative device, although the resulting threshold voltage was impractically small (5 mV) given current technology limitations.

Lab-on-a-chip bioanalysis systems are becoming more influential and provide a basis for massively distributed environmental sensors, implantable sensors, biochemical and nuclear agent detectors, among others. This work provides both a theoretical framework as well as experimentally verifies such techniques for the applications of micro-particle detection and optical measurements.

Bibliography

[1] N. Nelson, D. Sander, M. Dandin, S. Prakash, A. Sarje, and P. Abshire, "Hand-held fluorometers for lab-on-a-chip applications," *Biomedical Circuits and Systems, IEEE Transactions on*, vol. 3, no. 2, Apr. 2009.

[2] N. V. Loukianova, H. O. Folkerts, J. P. V. Maas, D. W. E. Verbugt, A. J. Mierop, W. Hoekstra, E. Roks, and P. Theuwissen, "Leakage current modeling of test structures for characterization of dark current in CMOS image sensors," *IEEE Trans. Electron Dev.*, vol. 50, no. 1, 2003.

[3] H. Ji, D. Sander, A. Haas, and P. Abshire, "Contact imaging: Simulation and experiment," *IEEE Transactions on Circuits and Systems I: Fundamental Theory and Applications*, vol. 54, no. 8, 2007.

[4] K. Boahen, "Point-to-point connectivity between neuromorphic chips using address event," *IEEE Trans. Circuits Syst. II*, vol. 47, May 2000.

[5] e. a. M. Petrovick, "Rapid sensors for biological agent identification," *Lincoln Laboratory Journal*, vol. 7, no. 1, 2007.

[6] http://www.innovativebiosensors.com/ibi_environmental_technology.html, 2010.

[7] D. Sander and P. Abshire, "Mismatch reduction for dark current suppression," *IEEE Sensors Conference*, 2011.

[8] K. Rahimi, C. Diorio, C. Hernandez, and M. Brockhausen, "A simulation model for floating-gate mos synapse transistors," *IEEE International Symposium on Circuits and Systems*, 26-29 May 2002.

[9] D. Sander, P. Stepanov, I. Weinberg, and P. Abshire, "Low noise cmos active pixel sensor for digital radiography," *Nuclear Science Symposium Conference Record*, 19-25 Oct. 2008.

[10] D. Sander, N. Nelson, and P. Abshire, "Integration time optimization for integrating photosensors," *IEEE ISCAS*, 18-21 May 2008.

[11] J. R. Lakowicz, "Principles of fluorescence spectroscopy, and 2nd ed." *New York: Kluwer Academic/Plenum*, 199.

[12] E. R. Fossum, "Cmos image sensors: electronic camera on a chip," in *Electron Devices Meeting, 1995., International*, Dec. 1995, pp. 17–25.

[13] N. Reeves, Y. Liu, N. M. Nelson, S. Malhotra, M. Loganathan, J.-M. Lauenstein, J. Chaiyupatumpa, E. Smela, and P. Abshire, "Integrated mems structures and CMOS circuitry for bioelectronic interface with single cells," *IEEE International Symposium on Circuits and Systems*, 2004.

[14] S. B. Prakash and P. Abshire, "On-chip capacitance sensing for cell monitoring applications," *IEEE Sensors Journal*, vol. 7, 2007.

[15] O. Yadid-Pecht, R. Ginosar, and Y. S. Diamand, "A random access photodiode array for intelligent image capture," *IEEE Tran. Elec. Dev.*, vol. 38, no. 8, Aug. 1991.

[16] T. Hamamoto and K. Aizawa, "A computational image sensor with pixel-based integration time control," *IEEE. Proc. Image Processing*, vol. 1, 10-13 Sept. 2000.

[17] H. Tian, B. Fowler, and A. E. Gamal, "Analysis of temporal noise in CMOS photodiode active pixel sensor," *IEEE Journal of Solid-State Circuits*, vol. 36, no. 1, Jan 2001.

[18] B. Pain, G. Yang, M. Ortiz, C. Wrigley, B.Hancock, and T. Cunningham, "Analysis and enhancement of low-light level performance of photodiode-type CMOS active pixel imagers operated with sub-threshold reset," *IEEE Workshop on Charge-Coupled Devices and Advanced Image Sensors*, Jun 9 ,1999.

[19] Y. Degerli, F. Lavernhe, P. Magnan, and J. Farre, "Analysis and reduction of signal readout circuitry temporal noise in CMOS image sensors for low-light levels," *IEEE Trans. Elec. Dev.*, vol. 47, no. 5, May 2000.

[20] J. Lai and A. Nathan, "Reset noise in active pixel image sensors," *Journal Vac. Sci. Technology*, vol. 22, no. 3, May 2004.

[21] B. Pain, G. Yang, T. Gunningham, C. Wrigley, and B. Hancock, "An enhanced-performance CMOS imager with a flushed-reset photodiode pixel," *IEEE Trans. Electron Dev.*, vol. 50, no. 1, 2003.

[22] B. Fowler, M. D. Godfrey, J. Balicki, and J. Canfield, "Low noise readout using active reset for CMOS aps," *Proc. of SPIE*, vol. 3965, 2000.

[23] Y. Chen and S. Kleinfelder, "CMOS active pixel sensor achieving 90 db dynamic range with column-level active reset," *Proc. of SPIE*, vol. 5301, 2004.

[24] S. Kleinfelder, "Novel integrated CMOS sensor circuits," *IEEE Trans. Nuc. Sci.*, vol. 51, 2004.

[25] K. Lee and E. Yoon, "A CMOS image sensor with reset level control using dynamic reset current source for noise suppression," *Proc. IEEE Solid State*, vol. 1, Feb. 2004.

[26] J. Y. et. al., "A 3m pixel low-noise flexible architecture CMOS image sensor," *IEEE ISSC*, 2006.

[27] B. Pain, T. J. Cunningham, B. Hancock, G. Yang, S. Seshadri, and M. Ortiz, "Reset noise suppression in two-dimension CMOS photodiode pixels through column-based feedback-reset," *Tech. Dig. IEDM*, 2002.

[28] M. Ikebe and K. Saito, "CMOS image sensor using negative-feedback resetting to obtain variably smoothed images," *IEICE Trans. Elect.*, vol. 89, no. 11, 2006.

[29] J. Yang, K. G. Fife, L. Brooks, C. G. Sodini, A. Betts, P. Mudunuru, and H. Lee, "A 3m pixel low-noise flexible architecture CMOS image sensor," *ISSC*, 2006.

[30] C.-Y. Wu, Y.-C. Shih, J.-F. Lan, C.-C. Hsieh, C.-C. Huang, and J.-H. Lu, "Design, and optimization, and performance analysis of new photodiode structures for CMOS active-pixel-sensor APS imager applications," *IEEE Sens. J.*, vol. 4, no. 1, 2004.

[31] M. A. Abdallah, E. Dubaic, H. E. Nilsson, C. Frojdh, and C. S. Petersson, "A scintillator-coated phototransistor pixel sensor with dark current cancellation," *Proc. of ICECS*, vol. 2, 2001.

[32] H. Cheng and Y. King, "A CMOS image sensor with dark-current cancellation and dynamic sensitivity operations," *IEEE Trans. Electron Dev.*, vol. 50, no. 1, Jan. 2003.

[33] J. Goy, B. Courtois, J. M. Karam, and F. Pressecq, "Design of an aps CMOS image sensor for low light level applications using standard CMOS technology," *Analog Integrated Circuits and Signal Processing*, vol. 29, no. 1, Oct. 2001.

[34] E. Bolton, G. Sayler, D. Nivens, J. Rocelle, S. Ripp, and M. Simpson, "Integrated CMOS photodetector and signal processing for very low-level chemical sensing with bioluminescent bioreporter integrated circuit," *Sensors and Actuators B*, vol. 85, 2002.

[35] B. Fowler, J. Balicki, D. How, S. Mims, J. Canfield, and M. Godfrey, "An ultra low noise high speed CMOS linescan sensor for scientific and industrial application," *SPIE Proc. Workshop on CCD and AIS*, 2003.

[36] Y. C. Shih and C. Y. Wu, "An optimized CMOS pseudo-active-pixel-sensor structure for low-dark-current imager applications," *Proc. IEEE Int. Symp. Circuits Systems*, vol. 1, May 2003.

[37] ——, "A new CMOS pixel structure for low-dark-current and large-array-size still imager applications," *IEEE Trans. Circuits Sys.*, vol. 51, no. 11, 2004.

[38] H. Ji and P. Abshire, "A CMOS image sensor for low light applications," *Proc. of ISCAS*, 2006.

[39] I. Fujimori, "A 256x256 CMOS differential passive pixel imager with fpn reduction techniques," *IEEE Solid-State Citcuits*, vol. 35, no. 12, pp. 2031 –2037, Dec. 2000.

[40] H. Eltoukhy, K. Salama, A. E. Gamal, M. Ronaghi, and R. Davis, "A 0.18μm CMOS 10^{-6}lux bioluminescence detection system-on-chip," *Proceedings of IEEE ISSCC*, vol. 1, 2004.

[41] H. Eltoukhy, K. Salama, and A. Gamal, "A 0.18-μm (CMOS) bioluminescence detection lab-on-chip," *IEEE Journal of Solid-State Circuits*, vol. 41, no. 3, 2006.

[42] H. Ji, M. Dandin, E. Smela, and P. Abshire, "Integrated fluorescence sensing for lab-on-a-chip devices," *IEEE NLM Life Science Systems & Applications Workshop*, 13-14 July 2006.

[43] D. Sander, M. Dandin, H. Ji, N. Nelson, and P. A. Abshire, "Low-noise CMOS fluorescence sensor," *IEEE International Symposium on Circuits and Systems*, 2007.

[44] E. R. Fossum, "Active pixel sensors - are ccds dinosaurs?" *Proc. SPIE*, vol. 1900, 1993.

[45] U. C. Fischer and H. P. Zingsheim, "Submicroscopic pattern replication with visible light," *Journal of Vacuum Science and Technology*, vol. 19, no. 4, 1981.

[46] ——, "Submicroscopic contact imaging with visible light by energy transfer," *Applied Physics Letters*, vol. 40, no. 3, 1982.

[47] U. C. Fischer, A. Naber, T. Dziomba, J. Koglin, W. Gohde, O. Panzer, and H. Fuchs, "Near-field optical tools to read, and write and copy information at the $100 - 10\ nm$scale," *Proceedings of the SPIE*, vol. 3272, 1998.

[48] J. A. Chakera, S. R. Kumbhare, and P. D. Gupta, "Characterization of X-ray contact microscopic imaging in kev spectral region using laser produced plasmas," *Journal of X-Ray Science and Technology*, vol. 8, no. 2, 1998.

[49] F. Calegari, S. Stagira, C. D'Andrea, G. Valentini, C. Vozzi, M. Nisoli, S. D. Silvestri, L. Poletto, P. Villoresi, A. Faenov, and T. Pikuz, "Table-top soft x-ray imaging of nanometric films," *Applied Physics Letters*, vol. 89, no. 11, 2006.

[50] M. Hayama, "Characteristics of p-i junction amorphous silicon stripe-type photodiode array and its application to contact image sensor," *IEEE Transactions on Electron Devices*, vol. 37, no. 5, 1990.

[51] H. Kakinuma, M. Mohri, M. Sakamoto, H. Sawai, S. Shibata, Y. Kasuya, Y. Ohnuki, and W. Chonan, "Direct-contact type image sensors using a novel amorphous-silicon photodiode array," *IEEE Electron Device Letters*, vol. 12, no. 8, 1991.

[52] S. N. Lu, E. Entcheva, V. Sharma, and L. Tung, "Optical mapping of anatomical reentry in monolayers of cultured neonatal rat cardiac myocytes," *Proceedings of IEEE EMBS*, vol. 1, 1999.

[53] E. Entcheva, S. N. Lu, R. H. Troppman, V. Sharma, and L. Tung, "Contact fluorescence imaging of reentry in monolayers of cultured neonatal rat ventricular myocytes," *Journal of Cardiovascular Electrophysiology*, vol. 11, no. 6, 2000.

[54] H. H. Chen, A. Kumar, Y. Yang, D. Wang, D. Maouyo, N. M. Fried, and X. Yang, "Development of a non-invasive optical imaging method for tracking vascular gene expression," *Proceedings of IEEE EMBS*, vol. 3, 2001.

[55] V. Dubaj, A. Mazzolini, A. Wood, and M. Harris, "Optic fibre bundle contact imaging probe employing a laser scanning confocal microscope," *Journal of Microscopy*, vol. 207, 2002.

[56] E. Entcheva, Y. Kostov, E. Tchernev, and L. Tung, "Fluorescence imaging of electrical activity in cardiac cells using an all-solid-state system," *IEEE Transactions on Biomedical Engineering*, vol. 51, no. 2, 2004.

[57] H. Ji, M. Urdaneta, E. Smela, and P. Abshire, "CMOS contact imager for monitoring cultured cells," *Proceedings of IEEE ISCAS*, 2005.

[58] A. Romani, R. Guerrieri, M. Tartagni, N. Manaresi, and G. Medoro, "Beyond the microscope: embedded detectors for cell biology applications," *Proceedings of IEEE ISCAS*, 2005.

[59] D. C. Ng, M. Matsuo, T. Tokuda, K. Kagawa, M. Nunoshita, H. Tamura, S. Shiosaka, and J. Ohta, "A CMOS image sensor for in vitro and in vivo imaging of the mouse hippocampus," *International Conference on Solid State Devices and Materials*, 2005.

[60] T. Tokuda, A. Yamamoto, K. Kagawa, M. Nunoshita, and J. Ohta, "A CMOS image sensor with optical and potential dual imaging function for on-chip bio-scientific applications," *Sensors and Actuators A*, vol. 125, 2005.

[61] T. Tokuda, D. C. NG, A. Yamamoto, K. Kagawa, M. Nunoshita, and J. Ohta, "A CMOS optical/potential image sensor with 7.5μm pixel size for on-chip neural and DNA spot sensing," *Proceedings of IEEE EMBS*, 2005.

[62] J. Ohta, D. C. Ng, H. Tamura, T. Tokuda, A. Yamamoto, M. Matsuo, M. Nunoshita, Y. Ishikawa, and S. Shiosaka, "Real time in vivo imaging and

measurement of serine protease activity in the mouse hippocampus using a dedicated complementary metal-oxide semiconductor imaging device," *Journal of Neuroscience Methods*, vol. 156, no. 1-2, 2006.

[63] J. Ohta, D. C. Ng, T. Tokuda, A. Yamamoto, M. Matsuo, M. Nunoshita, H. Tamura, Y. Ishikawa, and S. Shiosaka, "On-chip biofluorescence imaging inside a brain tissue phantom using a (CMOS) image sensor for in vivo brain imaging verification," *Sensors and Actuators B (Chemical)*, vol. 119, no. 1, 2006.

[64] D. C. Ng, T. Tokuda, A. Yamamoto, M. Matsuo, M. Nunoshita, H. Tamura, Y. Ishikawa, S. Shiosaka, and J. Ohta, "A complementary metal-oxide-semiconductor image sensor for on-chip in vitro and in vivo imaging of the mouse hippocampus," *Japanese Journal of Applied Physics, and Part 1*, vol. 45, no. 4, 2006.

[65] T. Tokuda, D. C. Ng, A. Yamamoto, K. Kagawa, M. Nunoshita, and J. Ohta, "An optical and potential dual-image CMOS sensor for on-chip neural and DNA imaging applications," *Proceedings of IEEE ISCAS*, 2006.

[66] D. C. Ng, T. Tokuda, T. Nakagawa, H. Tamura, M. Nunoshita, Y. Ishikawa, S. Shiosaka, and J. Ohta, "A new neural imaging approach using a CMOS imaging device," *Proceedings of IEEE EMBS*, 2006.

[67] M. Eggers, M. Hogan, R. Reich, J. Lamture, D. Enrlich, M. Hollis, B. Kosicki, T. Powdrill, K. Beattie, S. Smith, R. Varma, R. Gangadharan, A. Mallik, B. Burke, and D. Wallace, "A microchip for quantitative detection of molecules utilizing luminescent and radioisotope reporter groups," *Biotechniques*, vol. 17, no. 3, 1994.

[68] M. Adams, G. DeRose, S. R. Quake, and A. Scherer, "Fundamental approach for optoelectronic and microfluidic integration for miniaturizing spectroscopic devices," *Proceedings of SPIE*, vol. 4647, 2002.

[69] M. Adams, S. R. Quake, and A. Scherer, "On-chip absorption and fluorescence spectroscopy with polydimethylsiloxane (PDMS) microfluidic flow channels," *Proceedings of IEEE-EMBS Conf. on Microtechnologies in Medicine and Biology*, 2002.

[70] M. L. Adams, M. Enzelberger, S. Quake, and A. Scherer, "Microfluidic integration on detector arrays for absorption and fluorescence micro-spectrometers," *Sensors and Actuators A*, vol. A104, no. 1, 2003.

[71] G. Medoro, N. Manaresi, A. Leonardi, L. Altomare, Tartagni, and R. Guerrieri, "A lab-on-a-chip for cell detection and manipulation," *IEEE Sensors Journal*, vol. 3, no. 3, 2003.

[72] K. Salama, H. Eltoukhy, A. Hassibi, and A. E. Gamal, "Modeling and simulation of integrated luminescence detection platforms," *Proceedings of SPIE*, vol. 4966, 2003.

[73] H. Eltoukhy, K. Salama, A. E. Gamal, M. Ronaghi, and R. Davis, "A 0.18μm CMOS 10^{-6}lux bioluminescence detection system-on-chip," *Proceedings of IEEE ISSCC*, vol. 1, 2004.

[74] K. Salama, H. Eltoukhy, A. Hassibi, and A. E. Gamal, "Modeling and simulation of luminescence detection platform," *Biosensors and Bioelectronics*, vol. 19, no. 11, 2004.

[75] J. L. Gonzalez, D. Sadowski, K. V. I. S. Kaler, M. P. Mintchev, and O. Yadid-Pecht, "A CMOS imager for light blobs detection and processing," *Proc. of ISCAS*, 2005.

[76] T. Chen, P. Catrysse, A. E. Gamal, and B. Wandell, "How small should pixel size be?" *Proceedings of the SPIE*, vol. 3965, 2000.

[77] M. Born and E. Wolf, "Principles of optics (7th edition)," *Cambridge University Press*, 1999.

[78] S.-C. Liu, J. Kramer, G. Indiveri, T. Delbruck, and R. Douglas, "Orientation-selective avlsi spiking neurons," *Advances in Neural Information Processing Systems*, vol. 2, no. ISSU 14, 2002.

[79] C. M. Higgins and C. Koch, "A modular multi-chip neuromorphic architecture for real-time visual motion processing," *Analog Integrated Circuits and Signal Processing*, vol. 24, pp. 195–211, 2000.

[80] T. Choi, B. Shi, and K. Boahen, "A multi-chip implementation of cortical orientation hypercolumns," *Circuits and Systems, 2004. ISCAS '04. Proceedings of the 2004 International Symposium on*, vol. 3, may 2004.

[81] T. Choi, P. Merolla, J. Arthur, K. Boahen, and B. Shi, "Neuromorphic implementation of orientation hypercolumns," *Circuits and Systems I: Regular Papers, IEEE Transactions on*, vol. 52, no. 6, june 2005.

[82] E. Chicca, P. Lichtsteiner, T. Delbruck, G. Indiveri, and R. Douglas, "Modeling orientation selectivity using a neuromorphic multi-chip system," 2006.

[83] R. Vogelstein, U. Mallik, J. Vogelstein, and G. Cauwenberghs, "Dynamically reconfigurable silicon array of spiking neurons with conductance-based synapses," *Neural Networks, IEEE Transactions on*, vol. 18, no. 1, jan 2007.

[84] M. A. Mahowald, "VLSI analogs of neuronal visual processing: A synthesis of form and function," *Ph.D. Dissertation, and California Inst. Technol., and Pasadena*, 1992.

[85] K. Boahen, "A burst-mode word serial address-event link –i: Transmitter design," *IEEE Trans. Circuits Syst. I*, vol. 51, July 2004.

[86] ——, "A burst-mode word serial address-event link –ii: Receiver design," *IEEE Trans. Circuits Syst. I*, vol. 51, July 2004.

[87] ——, "A burst-mode word serial address-event link –iii: Analysis and test results," *IEEE Trans. Circuits Syst. I*, vol. 51, July 2004.

[88] Z. Kalayjin and A. Andreou, "Asynchronous communication of 2d motion information using winner-take-all arbitration," *J. Analog Integrated Circuits Signal Processing*, vol. 13, Mar. 1997.

[89] E. Culurciello and A. G. Andreou, "A comparative study of access topologies for chip-level address-event communication channels," *IEEE Transactions on Neural Networks*, vol. 14, no. 5, Sept. 2003.

[90] ——, "Aloha CMOS imager," *IEEE International Symposium on Circuits and Systems*, May 2004.

[91] ——, "CMOS image sensors for sensor networks," *Analog Integrated Circuits and Signal Processing, and Springer Netherlands*, vol. 49, no. 1, Oct. 2006.

[92] E. Culurciello, R. Etienne-Cummings, and K. Boahen, "High dynamic range, and arbitrated address event representation digital imager," *IEEE International Symposium on Circuits and Systems*, vol. 2, 2001.

[93] V. Brajovic, "Lossless non-arbitrated address-event coding," *Intl. Symposium on Circuits and Systems, ISCAS*, 25-28 May 2003.

[94] G. Xiaochuan, Q. Xin, and J. Harris, "A time-to-first-spike cmos image sensor," *Sensors Journal, IEEE*, vol. 7, no. 8, pp. 1165 –1175, aug. 2007.

[95] R. Probst, Z. Cummins, A. Nacev, and B. Shapiro, "Electrokinetic tweezers: living cells manipulation by vision sensing and electrokinetic feedback control," *Nature Protocol*, vol. to appear, 2011.

[96] Y. Nemirovsky, I. Brouk, and C. Jakobson, "1/f noise in CMOS transistors for analog applications," *IEEE Trans on Electron Devices*, vol. 48, no. 5, May 2001.

[97] B. A. Fowler, A. E. Gamal, D. Yang, and H. Tian, "Method for estimating quantum efficiency for CMOS image sensors," *Proc. SPIE*, vol. 3301, 1998.

[98] A. Moini, "Vision chips." *Norwell, and MA, and USA: Kluwer Academic Publishers*, 1999.

[99] B. Fowler, A. El Gamal, D. Yang, and H. Tian, "Method for estimating quantum efficiency for CMOS image sensors," *Proceedings SPIE*, vol. 3301, 1998.

[100] N. Nelson, S. Prakash, D. Sander, M. Dandin, A. Sarje, H. Ji, and P. Abshire, "A handheld fluorometer for UV excitable fluorescence assays," *IEEE Biomedical Circuits and Systems Conference*, 2007.

[101] A. Rabner and Y. Shacham, "A concept for a sensitive micro total analysis system for high throughput fluorescence imaging," *Sensors*, vol. 6, 2006.

[102] A. E. Bruno, S. Barnard, M. Rouilly, A. Waldner, J. Berger, and M. Ehrat, "A solid state miniaturized fluorescence sensor array for the determination of critical gases and electrolytes in blood," *Anal. Chem.*, vol. 69, 1997.

[103] D. A. Chang-Yen and B. K. Gale, "An integrated optical biochemical sensor fabricated using rapid-prototyping techniques," *Lab. Chip.*, vol. 3, 2003.

[104] E. Thrush, O. Levi, W. Ha, K. Wang, S. J. Smith, and J. S. Harris, "Integrated bio-fluorescence sensor," *J. Chromatography A.*, vol. 1013, 2003.

[105] S. Bellis, J. C. Jackson, and A. Mathewson, "Towards a disposable in vivo miniature implantable fluorescence detector," *SPIE Optical Fibers and Sensor for Medical Diagnositics and Treatment Applications VI*, vol. 6083, 2006.

[106] O. Hofmann, X. H. Wang, J. C. deMello, D. D. C. Bradley, and A. J. deMello, "Towards microalbuminuria determination on a disposable diagnostic microchip with integrated fluorescence detection based on thinfilm organic light emitting diodes," *Lab. On a Chip.*, vol. 5, 2005.

[107] D. Starikov, F. Benkabou, N. Medelci, and A. Bensaoula, "Integrated multi-wavelength fluorescence sensors," *ISA/IEEE Sens. for Industry Conf.*, 2002.

[108] M. L. Chabinyc, D. T. Chiu, J. C. McDonald, A. D. Stroock, J. F. Christian, A. M. Karger, and G. M. Whitesides, "An integrated fluorescence detection system in poly(dimethylsiloxane) for microfluidic applications," *Anal.Chem.*, vol. 73, 2001.

[109] J. A. Chediak, Z. S. Luo, J. G. Seo, N. Cheung, L. P. Lee, and T. D. Sands, "Heterogeneous integration of cds filters with gan leds for fluorescence detection microsystems," *Sens. Actuators A.*, vol. 111, 2004.

[110] V. P. Iordanov, J. Bastemeijer, R. Ishihara, P. M. Sarro, A. Bossche, and M. J. Vellekoop, "Filter-protected photodiodes for high-throughput enzymatic analysis," *IEEE. Sens. J.*, vol. 4, 2004.

[111] O. J. A. Schueller, D. C. Duffy, J. A. Rogers, S. T. Brittain, and G. M. Whitesides, "Reconfigurable diffraction gratings based on elastomeric microfluidic devices," *Sens. Actuators A.*, vol. 78, 1999.

[112] C. C. Chen, D. Hirdes, and A. Folch, "Gray-scale photolithography using microfluidic photomasks," *Proc. Natl. Acad. Sci. U. S. A.*, vol. 100, 2003.

[113] M. Dandin, P. Abshire, and E. Smela, "Optical filtering technologies for integrated fluorescence sensors," *Lab. On a chip.*, vol. 7, 2007.

[114] O. Hofmann, X. Wang, A. Cornwell, S. Beecher, A. Raja, D. D. C. Bradley, A. J. deMello, and J. C. de Mello, "Monolithically integrated dye-doped pdms long-pass filters for disposable on-chip fluorescence detection," *Lab.on aChip.*, vol. 6, 2006.

[115] G. Patounakis, K. Shepard, and R. Levicky, "Active (CMOS) array sensor for time resolved fluorescence detection," *IEEE Journal of Solid-State Circuits*, vol. 41, no. 11, 2006.

[116] "USB4000-FL fluorescence spectrometer data sheet," *Ocean Optics, and Dunedin, and FL USA*.

[117] "Pico*fluor* fluorometer data sheet," *Turner BioSystems, Sunnyvale, CA USA*, Sept. 2002.

[118] "Fluorpen - handheld chlorophyll fluorometer data sheet," *Qubit Systems, Kingston, ON Canada*, 2008.

[119] K. M. Kitchens, R. B. Kolhatkar, P. W. Swaan, N. D. Eddington, and H. Ghandehari, "Transport of poly(amidoamine) dendrimers across caco-2 cell monolayers: Influence of size, and charge and fluorescent labeling," *Pharmaceutical Research*, vol. 23, no. 12, Dec. 2006.

[120] R. Jevprasesphant, J. Penny, R. Jalal, D. Attwood, N. B. McKeown, and A. D'Emanuele, "The influence of surface modificaton on the cytotoxicity of PAMAM dendrimers," *International J. Pharmaceutics*, vol. 252, 2003.

[121] D. W. Zabriskie and A. E. Humphrey, "Estimation of fermentation biomass concentration by measuring culture fluorescence," *Applied and Environmental Microbiology*, vol. 35, no. 2, 1978.

[122] C. Ratledge, "Yeast physiology - a micro-synopsis," *Applied and Environmental Microbiology*, vol. 6, 1991.

[123] M. Armani, S. Chaudhary, R. Probst, and B. Shapiro, "Using feedback control and micro-fluidics to steer individual particles," *18th IEEE International Conference on Micro Electro Mechanical Systems*, 2005.

[124] ——, "Using feedback control of micro-flows to independently steer multiple particles," *Journal of Microelectromechanical Systems*, vol. 15, no. 4, Aug. 2006.

[125] L. Kremser, D. Blaas, and E. Kenndler, "Capillary electrophoresis of biological particles: Viruses, and bacteria, and eukaryotic cells," *Electrophoresis*, vol. 25, 2004.

[126] W. Korohoda and A. Wilk, "Cell electrophoresis: a method for cell separation and research into cell surface properties," *Cellular and Molecular Biology Letters*, vol. 25, no. 13, 2008.

[127] M. Urdaneta and E. Smela, "Multiple frequency dielectrophoresis," *Electrophoresis*, vol. 28, no. 19, 2007.

[128] "Kodak kac-00401 image sensor," *http://www.kodak.com/global/plugins/acrobat/en/business/ISS/productsummary/CMOS/KAC-00401ProductSummary.pdf*, 2010.

[129] R. Brolly, D. Carpenter, T. Guy, and G. Putnam, "New 640 x 480 image sensor achieves 120 full-resolution images-per-second," *http://www.kodak.com/global/plugins/acrobat/en/business/ISS/supportdocs/New640x480SensorAchieves120Full-ResolutionImagesperSecond.pdf*, 2010.

[130] "VTB process photodiode," *http://www.perkinelmer.com/CMSResources/Images/44-3639DTS_vtb1012b13b.pdf*, 2010.

[131] "Channel photomultipliers overview and specifications," *www.perkinelmer.com*, 2001.

[132] "H7826 series photosensor module," *http://sales.hamamatsu.com/assets/pdf/parts_H/m-h7826e.pdf*, 2010.

[133] A. Gulinatti, P. Maccagnani, I. Rech, M. Ghioni, and S. Cova, "35 ps time resolution at room temperature with large area single photon avalanche diodes," *Electronics Letters*, vol. 4, no. 5, 3 March 2005.

[134] R. Daniel, R. Almog, A. Ron, S. Belkin, and Y. S. Diamand, "Modeling and measurement of a whole-cell bioluminescent biosensor based on a single photon avalanche diode," *Biosensors and Bioelectronics*, vol. 24, no. 4, 1 December 2008.

[135] "MPPC (multi-pixel photon counter)," *http://jp.hamamatsu.com/resources/products/ssd/pdf/s10362-11_series_kapd1022e05.pdf*, 2010.

[136] K. Murari, R. Etienne-Cummings, N. Thakor, and G. Cauwenberghs, "Which photodiode to use: A comparison of cmos-compatible structures," *Sensors Journal, IEEE*, vol. 9, no. 7, july 2009.

[137] I. Shcherback and O. Yadid-Pecht, "Photoresponse analysis and pixel shape optimization for cmos active pixel sensors," *Electron Devices, IEEE Transactions on*, vol. 50, no. 1, pp. 12 – 18, jan 2003.

[138] R. Vijayaraghavan, S. Islam, M. Zhang, S. Ripp, S. Caylor, D. Bull, S. Moser, S. Terry, B. Blalock, and G. Sayler, "A bioreporter bioluminescent integrated circuit for very low-level chemical sensing in both gas and liquid environments," *Sensors and Actuators B: Chemical*, vol. 123, no. 2, 21 May 2007.

[139] P. Hasler, B. Minch, and C. Diorio, "An autozeroing floating-gate amplifier," *IEEE TCAS II*, vol. 48, no. 1, January 2001.

[140] T. Datta and P. Abshire, "Mismatch compensation of CMOS current mirrors using floating-gate transistors," *Circuits and Systems, and 2009. ISCAS 2009. IEEE International Symposium on*, 24-27 May 2009.

[141] V. Srinivasan, D. Graham, and P. Hasler, "Floating-gates transistors for precision analog circuit design: an overview," *Circuits and Systems, and 2005. 48th Midwest Symposium on*, vol. 1, 7-10 Aug. 2005.

[142] Y. Wong and P. Abshire, "A 144 × 144 current-mode image sensor with self-adapting mismatch reduction," *IEEE Transactions on Circuits and Systems I: Fundamental Theory and Applications*, vol. 54, no. 8, 2007.

[143] T. Constandinou, J. Georgiou, and C. Toumazou, "An auto-input-offset removing floating gate pseudo-differential transconductor," *Circuits and Systems, Proceedings of the 2003 International Symposium on*, vol. 1, 25-28 May 2003.

[144] V. Babu, A. Sekhar, R. S. Devi, and M. Baiju, "Floating gate mosfet based operational transconductance amplifier and study of mismatch," *Industrial Electronics and Applications, and 2009. ICIEA 2009. 4th IEEE Conference on*, 25-27 May 2009.

[145] M. Zhang, F. Devos, and J. Pone, "Trimming smart imagers for an image converter with a non-volatile analog memory," *Sensors and Actuators A: Physical*, vol. 47, 1995.

[146] A. Aslam-Siddiqi, W. Brockherde, M. Schanz, and B. Hosticka, "A 128-pixel cmos image sensor with integrated analog nonvolatile memory," *Solid-State Circuits, IEEE Journal of*, vol. 33, no. 10, pp. 1497–1501, oct 1998.

[147] M. Cohen and G. Cauwenberghs, "Floating-gate adaptation for focal-plane online nonuniformity correction," *IEEE Transactions on Circuits and Systems II: Analog and Digital Signal Processing*, vol. 48, no. 1, Jan. 2001.

[148] A. Pesavento, T. Horiuchi, C. Diorio, and C. Koch, "Adaptation of current signals with floating-gate circuits," *Analog Integrated Circuits and Signal Processing*, vol. 30, pp. 137–147, 2002.

[149] G. Fikos, L. Nalpantidis, and S. Siskos, "A compact aps with fpn reduction and focusing criterion using fgmos photocell," *Sensors and Actuators A: Physical*, vol. 147, no. 2, 2008.

[150] Y. L. Wong, M. H. Cohen, and P. A. Abshire, "A floating gate comparator with automatic offset adaptation for 10-bit data conversion," *Circuits and Systems I: Regular Papers, IEEE Transactions on*, vol. 52, no. 7, 2005.

[151] S. Prakash and P. Abshire, "A fully differential rail-to-rail CMOS capacitance sensor with floating-gate trimming for mismatch compensation," *Trans. Cir. Sys. Part I*, vol. 56, no. 5, May. 2009.

[152] C. H. Aw and B. A. Wooley, "A 128×128-pixel standard-CMOS image sensor with electronic shutter," *IEEE J. Solid-st. Circ.*, vol. 31, no. 12, 1996.

[153] M. Kyomasu, "A new mos imager using photodiode as current source," *IEEE J. Solid-st. Circ.*, vol. 26, no. 8, 1991.

[154] M. K. et al., "Advances in digital radiography: Physical principles and system overview," *Radiographics*, vol. 27, 2007.

[155] M. Spahn, "Flat detectors and their clinical applications," *European Radiology*, vol. 15, no. 9, Sept. 2005.

[156] L. Zhang, W. Rogers, and N. Clinthorne, "Potential of a compton camera for high performance scintilation mammography," *Phys. Med. Biol.*, vol. 49, 2004.

[157] K. Wong, P. Cheng, S. Adler, P. Abshire, V. Saveliev, S. Mun, and I. Weinberg, "Pet glove: A new technology for portable molecular imaging," *Medical Imaging: Visualization and Image-Guided Procedures, Proceedings of the SPIE*, vol. 6509, Mar 2007.

[158] C. Arvanitis, S. Bohndiek, G. Segneri, C. Segneri, C. Venanzi, G. Royle, A. Clark, J. Crooks, R. Halsall, M. Key-Charriere, S. Martin, M. Pryderch, R. Turchetta, and R. Speller, "A novel active pixel sensor with on-pixel analog-to-digital converter for mammography," *Nuclear Science Symposium Conference*, vol. 6, Oct-Nov 2006.

[159] C. E. Shannon, "A mathematical theory of communication," *J. Bell Syst. Tech.*, vol. 27, July 1948.

[160] P. M. Furth and A. G. Andreou, "A design framework for low power analog filter banks," *IEEE Trans. Cir. and Sys. I*, vol. 42, no. 11.

[161] H. Ji and P. Abshire, "Fundamentals of silicon based phototransduction," *Imagers From Phototransduction to Image Processing, and O. Yadid-Pecht and R. Etienne-Cummings Eds, and Springer*, 2004.